



UNIVERSIDAD DE CHILE
FACULTAD DE CIENCIAS FÍSICAS Y MATEMÁTICAS
DEPARTAMENTO DE INGENIERÍA MECÁNICA

MODELAMIENTO HIDRODINÁMICO DEL TRANSPORTE DE PORTADORES DE
CARGA FUERA DE EQUILIBRIO TÉRMICO EN UNA CELDA SOLAR COMPUESTA
POR UNA JUNTA PN

TESIS PARA OPTAR AL GRADO DE
MAGÍSTER EN CIENCIAS DE LA INGENIERIA, MENCIÓN MECÁNICA

MEMORIA PARA OPTAR AL TÍTULO DE
INGENIERO CIVIL MECÁNICO

CRISTIAN ANDRÉS JARA BRAVO

PROFESOR GUÍA:
WILLIAMS CALDERÓN MUÑOZ

MIEMBROS DE LA COMISIÓN:
AXEL OSSES ALVARADO
PATRICIO MENA MENA

Este trabajo ha sido parcialmente financiado por CONICYT

SANTIAGO DE CHILE
2020

RESUMEN DE: Tesis para optar al grado de Magíster en Ciencias de la Ingeniería, Mención Mecánica y Memoria para optar al título de Ingeniero Civil Mecánico.

POR: Cristian Andrés Jara Bravo.

FECHA: 14 de agosto de 2019

PROF. GUÍA: Williams Calderón Muñoz.

MODELAMIENTO HIDRODINÁMICO DEL TRANSPORTE DE PORTADORES DE CARGA FUERA DE EQUILIBRIO TÉRMICO EN UNA CELDA SOLAR COMPUESTA POR UNA JUNTA PN

Se espera que la tercera generación de celdas solares mantenga los bajos costos de producción alcanzados actualmente, al mismo tiempo de mejorar considerablemente los niveles de eficiencia. A medida que se desarrollan nuevos materiales y configuraciones, mejoras en el manejo térmico son requeridas, tanto para el diseño como para operación. El presente trabajo estudia el efecto de portadores de carga altamente energéticos, y fuera de equilibrio térmico, en una celda solar de GaAs compuesta por una junta PN.

En primer lugar, se aplica una aproximación asintótica al modelo hidrodinámico obteniendo simplificaciones válidas para la implementación numérica. Se obtiene la solución unidimensional en estado estacionario mediante la resolución iterativa del método de diferencias finitas. Utilizando dicho modelo, el efecto de las condiciones de borde térmicas en el rendimiento de la celda es estudiado. Mayores valores de potencia son alcanzados para bajas temperaturas de lattice y altas para los portadores de carga. Se obtiene una dependencia térmica lineal entre el voltaje de circuito abierto y la temperatura de electrones en los bordes de $dV_{oc}/dT_n = 3,2 \text{ mV/K}$. Lo anterior es una consecuencia directa de la extracción de *hot-carriers*, dado que el exceso de energía no es transformado en calor hacia la lattice.

Para mejorar la consistencia del modelo para trabajos futuros, los supuestos térmicos para los hoyos son analizados mediante la comparación de la condición de equilibrio térmico con los electrones y con la lattice. Se observa que, a menos que el balance térmico sea resuelto para los hoyos, lo más razonable es considerarlos en equilibrio térmico con la lattice dado que, en caso contrario, la mayor temperatura alcanzada por los electrones, junto con la mayor masa efectiva de los hoyos, genera una distorsión en el campo eléctrico al mismo tiempo que una alta recombinación en las cercanías de la junta, lo que no es esperado en estos dispositivos.

Finalmente, diferentes modelos de saturación de velocidad fueron comparados para obtener la mejor representación del comportamiento de las bandas individuales. Se propone el uso del modelo de Baccarani y Wordeman junto con un balance poblacional entre bandas de conducción para la densidad de electrones, para ser utilizado junto con el modelo hidrodinámico. Los resultados de tiempos de relajación para momentum y energía, masa efectiva y velocidad de drift son comparados con resultados de un estudio mediante el método de Monte Carlo. Se obtiene un buen nivel de ajuste para la velocidad de drift, mientras que el resto de los parámetros de transporte presenta mayores divergencias, especialmente en el rango medio de campo eléctrico, donde la transferencia de electrones comienza. La modificación de la función de distribución de población entre las bandas central y satélite podría llevar a resultados más precisos y una mejor representación de los fenómenos térmicos al interior de la celda.

ABSTRACT FOR: Thesis for the degree of Master of Science in Engineering, Mechanical Mention & Memory for the degree of Mechanical Engineer.

AUTHOR: Cristian Andrés Jara Bravo.

DATE: August 14, 2019

GUIDE PROF.: Williams Calderón Muñoz.

HYDRODYNAMIC MODELING OF CHARGE CARRIERS TRANSPORT OUT OF THERMAL EQUILIBRIUM ON A PN JUNCTION SOLAR CELL

Third generation solar cells are expected to maintain currently achieved low production costs while greatly improving efficiency values. As new materials and configurations are developed, a better thermal management of the devices is needed, both in design and operation. In the present work, a study is performed on the effect of highly energetic, out of thermal equilibrium charge carriers on a PN junction GaAs solar cell.

On the first place, an asymptotic approximation is performed on the full hydrodynamic model, allowing to recognize valid simplifications for the numerical implementation. The steady state, one-dimensional solution of a GaAs single junction solar cell is obtained iteratively through a finite difference scheme. Using this model, the effect of thermal boundary conditions on the performance of the cell is studied. Higher values of power output are obtained with low lattice temperature and high temperature for carriers. A positive value of $dV_{oc}/dT_n = 3.2 \text{ mV/K}$ was obtained for the open circuit linear thermal dependence factor for electron temperature at the boundaries. This is a direct consequence of hot carrier extraction, given that the excess of energy is not transformed into lattice heating.

In order to improve the consistency of the model for future works, the thermal assumption for holes is analyzed comparing the condition of thermal equilibrium with electrons and lattice. It is found that, unless energy balance is solved separately for holes, the most reasonable assumption is to consider thermal equilibrium with the lattice, given that the higher temperatures reached by electrons, along with higher effective masses for holes, generate a distortion in the electric field leading also to high recombination rates near the junction, which are not expected for these devices.

Finally, different velocity saturation models were compared in order to obtain the best representation for the behavior of individual bands. With this, the use of the Baccarani and Wordeman model for velocity saturation, combined with a population balance between energy bands for electron density is proposed for its use with the hydrodynamic model. The results for momentum and energy relaxation times, effective mass and drift velocity are compared with results from a Monte Carlo study. A good fit is obtained for drift velocity, while transport parameters show more divergence, especially in the mid-field range, where electron transfer begins. The use of a different population distribution function between central and satellite bands could lead to more accurate results and a better representation of the thermal phenomena within solar cells.

Agradecimientos

Este trabajo fue parcialmente financiado por la beca de Magíster Nacional Complementaria del PFCHA de CONICYT folio 221320780, junto con la Facultad de Ciencias Físicas y Matemáticas de la Universidad de Chile.

Después de un proceso tan largo e interrumpido como lo fue este trabajo, han sido tantas las personas con las que me he cruzado y relacionado que sería difícil agradecer a cada uno haciéndoles justicia, y sin olvidar a una parte importante. Mi única opción sería escribir algunos lugares comunes como que de cada una de estas personas he recibido más apoyo y comprensión del que merezco, al mismo tiempo que me han enseñado valiosas lecciones en todo ámbito desde lo humano a lo mundano, llegando incluso a lo laboral; muy lugares comunes serán pero es la verdad. Espero poder expresar mi gratitud mediante acciones y gestos, más que unas pocas palabras escritas.

Una historia aparte es con mis papás, quienes merecen bastante más que unas escuetas palabras. Ojalá algún día pueda devolver a alguien el apoyo y cariño que me han dado, especialmente en esta etapa. Los quiero.

Contents

1	Introduction	1
2	Literature review	7
2.1	Semiconductor Material Basics	7
2.1.1	Structure	8
2.1.2	Band Structure in Semiconductors	10
2.1.3	Effective Masses	16
2.1.4	Statistics at Equilibrium	19
2.2	Carrier Transport Models	24
2.2.1	Poisson's Equation for Electrostatics	25
2.2.2	Boltzmann's Transport Equation	25
2.2.3	Hydrodynamic Transport Model	28
2.2.4	Scattering Approximations	30
2.2.5	Heat Flow Approximation	33
2.2.6	Lattice Energy Balance	34
2.2.7	Drift-Diffusion Transport Model	35
2.3	Mobility and Relaxation Times	36
2.3.1	Lattice Mobility	37
2.3.2	Mobility Degradation by Impurities	38
2.3.3	High Energy Mobilities	41
2.4	Interband Scattering Processes	47
2.4.1	Generation	47
2.4.2	Recombination	51
2.5	Analytical solution for a PN junction	56
2.5.1	Depletion Region Approximation	56
2.5.2	Solution for $J(V)$	58
3	Methodology	63
3.1	Problem Description	63
3.2	The Hydrodynamic Model	64
3.3	Boundary Conditions	66
3.3.1	Voltage	66
3.3.2	Majority Carrier Densities	66
3.3.3	Minority Carrier Densities	67
3.3.4	Temperatures	68
3.4	Nondimensionalization	69
3.5	Asymptotic Approximation	72
3.6	Numerical Method	73

3.6.1	Newton's Method	73
3.6.2	Discretization	74
3.6.3	Boundary Conditions for Newton's Method	76
3.6.4	Numerical Procedure	76
4	Results	79
4.1	Numerical Verification	79
4.2	HD modeling of a single junction solar cell	88
4.3	Hot Carriers at the contacts of a solar cell	92
4.3.1	GaAs Solar Cell Characteristics and Comparison to Experimental Data	96
4.3.2	Suggested Improvements in Design of Concentrator Solar Cell	97
4.3.3	Considerations Regarding the Assumptions for Case 2	99
4.4	Hole Temperature Assumption Verification	99
4.5	High Field Mobility Effects	104
4.5.1	Velocity Saturation Models	105
4.5.2	Baccarani & Wordeman Transferred Electron Model	108
	Conclusions	117
	Bibliography	122
A	HD model derivation	130
A.1	Zeroth moment	130
A.2	First moment	130
A.3	Second moment	132
B	Components of the Jacobian Matrix	134

List of Tables

2.1	Parameters for modeling bandgap energies [26].	15
2.2	Parameters for modeling effective masses [27, 28].	18
2.3	Parameters for modeling temperature dependence of effective masses [27, 28].	18
2.4	Parameters for modeling temperature dependence of carrier mobility	38
2.5	GaAs parameters for low field mobility calculation [40].	39
2.6	Si parameters for low field mobility calculation.	40
2.7	Parameters for the calculation of saturation velocity [43].	41
2.8	Parameters for the calculation of energy relaxation times as a function of temperature.	43
2.9	Parameters for the calculation of E_T as a function of doping density [51]. . .	45
2.10	Impact ionization modeling constants for III-V materials.	51
2.11	Recombination parameters for GaAs [26, 29].	56
4.1	Parameters used to solve case 1.	80
4.2	Transport properties for the device in case 1.	80
4.3	Material properties for the device in case 1.	80
4.4	Non-dimensional groups values for case 1.	81
4.5	Non-dimensional location of the L^∞ norm.	85
4.6	Relevant parameters and properties for Case 2.	93
4.7	Relevant parameters and properties for Case 3.	100

List of Figures

1.1	Power generation capacity additions in GW. <i>Source:</i> Bloomberg New Energy Finance.	2
1.2	Relationship between power conversion efficiency, module areal costs and cost per peak Watt (in \$/Wp). [6].	4
2.1	2D Representation of lattice and basis concepts.	8
2.2	Basic Bravais lattices.	9
2.3	Conventional unit cube for GaAs [21].	10
2.4	Periodic potential with the same periodicity as $ \psi ^2$ [22].	13
2.5	Formation of energy bands for electrons in a silicon crystal with a diamond-type lattice structure.	13
2.6	Brillouin zones for fcc diamond and zincblende lattices [23].	14
2.7	Calculated band structure of GaAs (left) and Silicon (right) [21].	15
2.8	Schematic representation of electrons and holes.	16
2.9	Value of Fermi function versus energy for different temperatures.	20
2.10	Schematic representation of doping process in Si.	21
2.11	Drift velocity of carriers in high purity Si and GaAs as a function of the applied electric field at $T = 300[K]$ [30].	37
2.12	Electron mobility in GaAs for various temperatures using the empirical relation (2.95).	40
2.13	Electron velocity in n -doped GaAs with $N_D = 10^{16} \text{ cm}^{-3}$, as a function of electric field using the transferred electron model and Monte Carlo results.	45
2.14	Solar spectrum in photon flux density for AM0 and AM1.5 [23].	48
2.15	Optical absorption coefficient for different semiconductor materials [59].	49
2.16	Schematic representation of different recombination mechanisms.	51
2.17	Schematic representation of different zones in a PN junction.	57
2.18	Current-voltage characteristic curves for solar cells using the depletion region approximation and different values of m	61
3.1	Scheme of a PN junction solar cell.	64
3.2	Numerical procedure diagram.	78
4.1	Different convergence steps towards of Newton's method for the solution of the HD model in case 1, using $N_u = 2000$	82
4.2	Solution of the HD model in case 1 for different mesh grid numbers, $N_u = 100, 500$ and 10000	83
4.3	Convergence of each variable using the norm L^∞	84
4.4	Convergence of each variable using the norm L^1	84
4.5	Value of the total current J_T for different mesh grid numbers.	86

4.6	Effect of using a high relaxation parameter θ	86
4.7	Minority boundary condition for hole density after several iteration steps, using two values of θ	87
4.8a	Solution plots of the hydrodynamic model for case 1. Results of electric potential and field.	88
4.8b	Solution plots of the hydrodynamic model for case 1. Results of carrier densities for electrons (left) and holes (right).	89
4.8c	Solution plots of the hydrodynamic model for case 1. Results of carrier velocities for electrons (left) and holes (right).	90
4.8d	Solution plots of the hydrodynamic model for case 1. Results of electron temperature increase (left) and lattice temperature increase (right).	91
4.9a	Steady-state solution for voltage across a PN junction at different forward bias under 1 Sun of illumination and AM 1.5 spectrum.	94
4.9b	Steady-state solution for electric field across a PN junction at different forward bias under 1 Sun of illumination and AM 1.5 spectrum.	94
4.9c	Steady-state solution for electron density across a PN junction at different forward bias under 1 Sun of illumination and AM 1.5 spectrum.	94
4.9d	Steady-state solution for hole density across a PN junction at different forward bias under 1 Sun of illumination and AM 1.5 spectrum.	95
4.9e	Steady-state solution for electron velocity across a PN junction at different forward bias under 1 Sun of illumination and AM 1.5 spectrum.	95
4.9f	Steady-state solution for hole velocity across a PN junction at different forward bias under 1 Sun of illumination and AM 1.5 spectrum.	95
4.9g	Steady-state solution for lattice temperature across a PN junction at different forward bias under 1 Sun of illumination and AM 1.5 spectrum.	96
4.9h	Steady-state solution for carrier temperature across a PN junction at different forward bias under 1 Sun of illumination and AM 1.5 spectrum.	96
4.10a	Total current density vs. voltage characteristics for a GaAs PN junction solar cell under 1 Sun with AM 1.5 spectrum, at different lattice temperature boundary conditions, T_L , and different charge carrier temperatures, T_c	98
4.10b	Power output density vs. voltage characteristics for a GaAs PN junction solar cell under 1 Sun with AM 1.5 spectrum, at different lattice temperature boundary conditions, T_L , and different charge carrier temperatures, T_c	98
4.11a	Total current density vs. voltage characteristics for a GaAs PN junction solar cell under 1 Sun with AM 1.5 spectrum, $T_L = 300[K]$ (lattice temperature boundary conditions) at different charge carrier temperatures, T_c	98
4.11b	Power output density vs. voltage characteristics for a GaAs PN junction solar cell under 1 Sun with AM 1.5 spectrum, $T_L = 300[K]$ (lattice temperature boundary conditions) at different charge carrier temperatures, T_c	99
4.12	Electric potential and field under the assumptions of $T_p = T_L$ and $T_p = T_n$	101
4.13	Carrier densities and velocities under the assumptions of $T_p = T_L$ and $T_p = T_n$. The red and blue lines correspond to electrons and holes respectively.	101
4.14	Electron and lattice temperature increase under the assumptions of $T_p = T_L$ and $T_p = T_n$	102
4.15	Recombination rate under the assumptions of $T_p = T_L$ and $T_p = T_n$	103
4.16	Mobility in GaAs as a function of electric field, according to Baccarani & Wordeman and Hänsch models.	106

4.17	Drift velocity in GaAs as a function of electric field, according to Baccarani & Wordeman and Hänsch models.	106
4.18	Drift velocity in GaAs as a function of electric field according to Hänsch model, considering different values for energy relaxation time.	107
4.19	Electron temperature in GaAs as a function of electric field, according to Baccarani & Wordeman and Hänsch model, using different values for energy relaxation time.	107
4.20	Mobility in GaAs as a function of carrier temperature (high field), according to Baccarani & Wordeman and Hänsch models, for two doping levels.	108
4.21	Average electron drift velocity for individual valleys using the BW model, along with the field dependent transferred electron model.	110
4.22	Total average electron drift velocity using the BW model for each band, along with the transferred electron model. Two different weighing functions for the total energy relaxation time are used.	111
4.23	Total energy relaxation time $\tau_{e,n}$ as a function of electron temperature, using the two different weighing functions f_1 and f_2	112
4.24	Total average electron drift velocity using the BW model for each band, along with the transferred electron model. Three different values of $\mu_{n,0}^L$ are used, for a saturation velocity of $v_{n,\text{sat}}^\Gamma = 4 \cdot 10^7$	112
4.25	High-field electron drift velocity using the field dependent and Baccarani & Wordeman based transferred electron models, along with Monte Carlo results from Tait [52].	113
4.26	High-field behavior of momentum relaxation time for electrons using the Baccarani & Wordeman based transferred electron model, along with Monte Carlo results from Tait [52].	114
4.27	High-field behavior of electron effective mass using the Baccarani & Wordeman based transferred electron model, along with Monte Carlo results from Tait [52].	115
4.28	High-field behavior of electron temperature using the Baccarani & Wordeman transferred electron model, along with Monte Carlo results from Tait [52].	115
4.29	High-field behavior of energy relaxation time for electrons using the Baccarani & Wordeman transferred electron model, along with Monte Carlo results from Tait [52].	116

Chapter 1

Introduction

In recent years, solar photovoltaic (SPV) energy has become one of the major contributors to the energy generation world wide, showing an increase in added capacity which not only is expected to be sustained but even to accelerate in subsequent years. Figure 1.1, obtained from a study by Bloomberg New Energy Finance [1], shows the new power generation capacity additions worldwide divided by energy source and classified by renewable or fossil sources. This chart shows how 2013 was a turning point where more renewable energies were used for new power generation instead of fossil fuels. The trend of an increase in the addition of low carbon emission energy sources along with a decrease in the use of fossil fuels is projected to become even more significant.

Given the recent technological advances, in the year 2015 more than 50 GW were added of SPV, surpassing 1% of the world's electricity capacity. SPV is expected to become the largest source of new electricity even under conservative considerations, assuming lower growth rate than what it is currently experiencing. Higher participation of solar energy is something that has been expected since the introduction of modern solar cells, given that it is considered to be the only energy source that is available in large enough quantity to sustainably supply the increasing energy demand in long term; but its penetration has occurred much more rapidly than what was predicted. As can be seen in Fig.1.1, wind power is also currently experiencing a similar expansion but it is expected to slow down because of its lower relative abundance. Therefore, it is crucial to investigate in modern solar technologies. In this context, the present thesis work aims to clarify some important concepts regarding solar cells. In particular we focus on studying how hot-carriers affect solar cells. Understanding the physics of these high-energy charge carriers could lead to the development of new technologies, as well as to improve the management of current technologies under operating conditions.

According to the Global Status Report on renewable energies of 2016 by the Renewable Energy Policy Network for the 21st Century, REN21 [2], this market expansion in most of the world is due largely to the increasing competitiveness of solar PV, as well as to new government programmes, rising demand for electricity and improving awareness of the potential of SPV as countries seek to lessen pollution and CO₂ emissions. Until recently, solar energy demand was concentrated in wealthy countries, but the decreasing cost to efficiency ratio has made possible that emerging countries in the developing world contribute significantly to the global growth of SPV. This is the case of Chile, which ranked among the top 15 countries in SPV capacity addition in 2015.

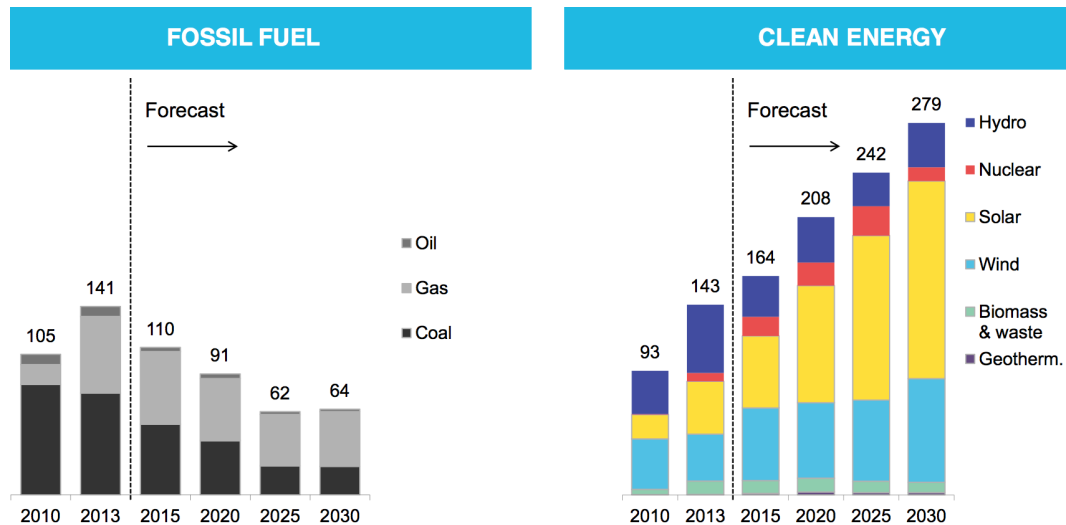


Figure 1.1: Power generation capacity additions in GW. *Source:* Bloomberg New Energy Finance.

Chilean energy matrix is composed by many independent systems, being the most important the *Sistema Interconectado del Norte Grande* (SING) and *Sistema Interconectado Central* (SIC), which comprise 21.98% and 77.24% of the total installed capacity, respectively. The installed capacity of electric power generation in both systems reaches 22.1 GW of which 15.4% corresponds to non-conventional renewable energies (NCRE) and 11.8% only to solar and wind power¹. In the year 2015, Chile installed over 0.4 GW of SPV energy, mostly in very large-scale projects, with a year-end total exceeding 0.8 GW. This trend will persist in the following years, given that during the last public tender for power generation, which had a record average price of 47.6 USD/MWh, 60% of the awarded projects corresponded to renewable energies.

An overall problem in countries with rapidly growing renewable energy supply has been the grid saturation because of insufficient transmission capacity. This has been an issue the previous years in Chile, where some renewable energy centrals have had to throw away up to 40% of their energy production. Nonetheless, a recent study led by the Ministry of Energy [3] has shown that NCRE could comprise more than 40% of the grid capacity in an efficient way, considering the fact that the SIC and SING systems will soon be interconnected. Concerning SPV and WP, the study indicates that at least 20% can be incorporated annually without making any adjustments to the current status of the system. Making some improvements 30% could be reached while maintaining the economical optimum of the system. This agrees with the report by REN21 which states that electricity market design is increasingly important, and there is a need for new business models. The study itself claims to be conservative, which means that there is still plenty of space for NCRE, and specifically SPV, to be integrated into the grid.

While some countries have already occupied much of their available installation space, Chile could benefit from the next generation technologies as they develop. Most of the SPV technologies in use nowadays are considered to be first generation. The leading technology among

¹Data from the National Commission of Energy (CNE) corresponding to the month of August 2016.

them until now has been by far single-junction Silicon solar cells. These have the advantage of being made from an abundant raw material which, however, needs to be processed into its pure crystalline form, increasing the costs. Nevertheless, the price of developing this technology has decreased steadily in recent years given the progress in the know-how, advances in technology and larger volumes of production, caused mainly by an increase in the demand of clean energies. Although the efficiency of these cells has increased substantially, they have a well known theoretical ceiling, which is known as the Shockley–Queisser limit. In 1961 Shockley and Queisser calculated a theoretical limit of 33.7% for a single junction solar cell, using the detailed balance method[4]. The most important assumptions of this method were that electrons and holes suffered no collisions. Therefore, any generated carrier would be collected instantly, and that there is complete absorption for photons with energies above the bandgap energy (E_g). Within these assumptions, an optimal bandgap separation can be found which maximizes the theoretical efficiency. This optimum arises from a trade-off between more photons being captured and the decrease of open circuit voltage (V_{oc}) along with E_g . The record efficiency for a mono-crystalline Silicon solar cell under non-concentrated light at 2016 is of 25%.

The second generation of photovoltaics arise from the premise that any mature solar cell technology seems likely to evolve to the stage where costs are dominated by those of the constituent materials [5]. In this sense, second generation PV consists mainly in thin-film solar cells, which benefit from light trapping techniques, but have the same limitations as the first generation in terms of maximum achievable efficiency. Among these technologies are Copper Indium Gallium Selenide (CIGS) and Cadmium Telluride (CdTe) solar cells, with record efficiencies of 22.3% and 22.1% respectively.

Third generation photovoltaic technologies aim to reduce one of the most important inefficiencies in photovoltaic conversion which is the loss of energy due to an excess (or lack) of energy from the photons with respect to E_g , while maintaining a low price per module. Although the goal is the same, there are different approaches for its achievement. Figure 1.2 graphically presents the relationship between power conversion efficiency, module areal costs and cost per peak Watt of energy production for different technologies, showing how next generation technologies aim to surpass the SQ limit at lower costs.

The first and most renowned of these technologies are multi-junction or tandem solar cells, which consist of using different bandgap materials, allowing for a larger portion of solar light to be absorbed more efficiently. This is equivalent to stacking solar cells of different bandgaps on top of each other, therefore a larger number of junctions means more efficient light conversion. However, many difficulties arise at the bonding of materials, which need to be lattice matched, increasing the costs of production. Current efficiency record for a tandem solar cell is 46%, achieved at 2015 by a four junction cell under light concentration; the limit according to a detailed balance for an infinite layer cell is of 86%[7]. Although this type of cells are more expensive than single junctions, they have been expected to be competitive with other technologies through the use of optics and light concentration.

A more recent concept are intermediate-band solar cells (IBSC), which use only one junction, but with multiple narrow density of states within the bandgap forming an intermediate band. Fermi level must be located within the IB in order for this concept to be effective. This

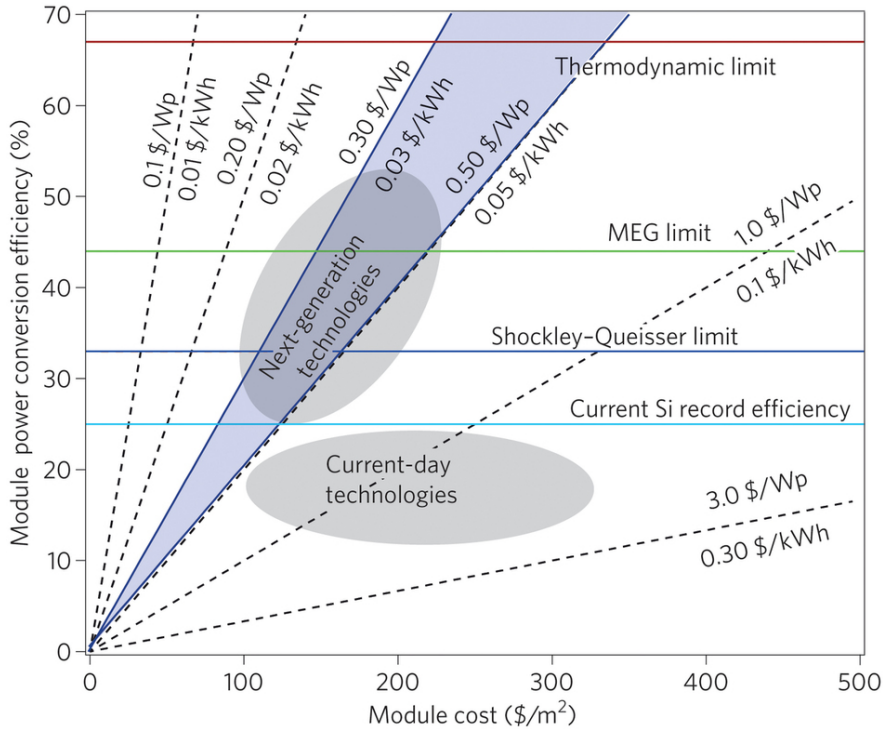


Figure 1.2: Relationship between power conversion efficiency, module areal costs and cost per peak Watt (in $\$/\text{Wp}$). [6].

additional states allow for sub-band absorption without the decrease in V_{oc} associated to a lower E_g . The latest approach in this context is the use of quantum dots (QD) for the formation of these intermediate bands, which are placed between the P and N sides of the junction. Quantum dot solar cells (QDSC) that show sub-bandgap absorption have been successfully fabricated but present lower V_{oc} . This decrease is attributed to non-radiative recombination caused by imperfections originated from the growth techniques. An efficiency of 11.3% has been achieved for this type of cells at this date.

Hot carrier solar cells (HCSC) are also a very recent concept that, in turn, pretend to transform the energy of carriers generated from photons with energies above E_g (hot-carriers) directly into electricity, before they are thermalized as heat to the lattice through phonons. This process is normally very fast, in the order of less than a picosecond, hence the difficulty of extracting these carriers. The excess of energy transported by hot-carriers can be exploited in two forms: by being collected in energy selective contacts, or by generating new carriers through impact ionization, also called multiple exciton generation (MEG). A detailed balance limit of 86% has been calculated for this type of solar cells[8]. To this date, no successful HCSC has been produced, and much research is being done for an appropriate energy selective contact. Nevertheless, evidence of a hot-carrier photocurrent from an InGaAs single quantum well solar cell has already been achieved [9].

Many efforts are also being made towards obtaining cells with very low costs of production. Until recently, organic solar cells were the main research focus in this aspect, but the newly developed perovskite solar cells have had many advances, being the fastest advancing solar technology to date. Current record efficiency for organic solar cells is 11.8%, and 22.1% for

perovskite cells.

Another option is to convert the solar spectrum into a narrower distribution of photons suited to the bandgap of the solar cell. In this way, several sub-bandgap photons can be absorbed in order to extract a photon with an energy above the bandgap in a process called up-conversion (UC) or above-bandgap photons can be reduced to multiple lower energy photons in a process called down-conversion (DC). This method has shown few advances, but has the advantage of being able to be used with any photovoltaic technology.

Whatever method is used for optimizing the transformation of solar light into electricity, it is evident that high energy phenomena such as hot-carriers need to be studied in further detail in order to improve the design of these technologies.

Macroscopic transport models have been widely used in semiconductor-device simulation in general and in solar cells in particular. However, most of the modeling has been achieved through drift-diffusion models or more simplified approaches as the depletion region approximation (DRA)[10]. In order to successfully represent higher energy phenomena, models with higher orders of accuracy are needed. Among these, the most used are Energy Transfer (ET) and Hydrodynamic (HD) models. These have been used since many years to simulate high-energy phenomena such as velocity overshoot [11], electron shock waves [12], impact ionization in PN junctions [13], electron vortices [14] or modeling heat generation in semiconductor devices [15, 16, 17].

Nevertheless, not much research has been done using these models in order to understand the effects of high energy phenomena in the ambit of solar cells, which would help improve the design of these new technologies. This could also lead to a better comprehension of the relationship between carrier transport and heat generation, improving the thermal control of solar cells under operating conditions or preventing damaging effects such as hot spots.

In this line of research, this thesis continues the work by Calderón and Osses [18] which studied electron and hole transport in a solar cell based on a Gallium Arsenide (GaAs) PN junction and its dependency with electron and lattice temperatures. A lattice temperature distribution throughout the device was obtained considering the change of kinetic energy of electrons due to interactions with the lattice and heat absorbed from sunlight. It was obtained that in terms of performance, higher values of power output are obtained with low lattice temperature and hot energy carriers. This analysis was performed using a one-dimensional hydrodynamic model considering charge carriers and lattice out of thermal equilibrium, which was solved through the perturbation method in asymptotic expansions. However, electrons and holes were considered to have an equal constant temperature through the device, therefore, an energy balance equation was solved for lattice temperature only.

In this research, a one-dimensional two-temperature hydrodynamic model is used to simulate the steady-state operating conditions of a GaAs single PN junction solar cell used under illumination. The dependency of charge carrier and lattice temperature boundary conditions with power output is discussed. The main objectives of the present work are described ahead.

Objectives

General Objective

- To study the relation between performance and thermal behavior on a GaAs solar cell, under the consideration of charge carriers out of thermal equilibrium with lattice.

Specific Objectives

- Apply valid simplifications on the hydrodynamic model in order to reduce non-linearities for a simpler numerical implementation.
- Obtain a solution of the model through the finite difference method, for a single junction GaAs solar cell.
- Analyze the performance effect of charge carrier temperature at the boundaries.
- Analyze the model assumptions, and propose possible improvements for future implementations.

Chapter 2

Literature Review

Just as solar cells themselves, the work done on this thesis involves concepts regarding both electrical and mechanical engineering that need to be addressed before depicting and discussing the results. As a broad definition, a solar cell is any device which converts the energy from a source of light into electrical current in a direct way. The most basic requirements in order to do this are a density of states (DOS) bottleneck in the material and selective contacts. Since this research is focused on PN junction solar cells, the DOS bottleneck is achieved using a semiconductor material and the selective the contacts through the formation of the PN junction. These conditions determine the effectiveness of the solar cell for generating charge carriers from incoming photons, and carrying them through the device into the contacts.

Besides the kind of material, many external factors affect the behavior of solid state devices in general and solar cells in particular. Therefore, the most important concepts will also be explained ahead like the interactions between incoming light and the material, and the effect of different thermal scenarios affecting the device. The latter is of special interest in this thesis work, since thermal behavior of the lattice and charge carriers are studied using a two temperature model.

The following literature review briefly describes these basic concepts needed for a complete understanding of the research and its results.

2.1 Semiconductor Material Basics

Semiconductors used in solid state devices are crystalline materials composed by elements in group IV of the periodic table; a combination of groups III and V; or groups II and VI. Most commonly used materials are Silicon (Si) or Germanium (Ge) from group IV, Gallium Arsenide (GaAs) or Indium Arsenide (InAs) from groups III+V and Cadmium Telluride from groups II+VI among many others. The fact that many combinations of elements can be used, allows to achieve a great variety of properties like different electrical conductivities, light absorption or generation, and even mechanical properties. Moreover, all these properties also depend on the direction that the crystalline cell is oriented; defects existence, like doping or free bonds on the surface (both explained ahead); lattice mismatch between different

materials and any other crystalline property. The following subsections describe important concepts for the understanding of the role of semiconductor materials in electronic devices, focusing mainly in GaAs which is the material used through this study.

2.1.1 Structure

The fact that semiconductor materials have a crystalline structure provides important benefits in terms of electromagnetic properties. However, imperfections in the consolidation of the material have repercussions with positive or negative effect depending on the context of the device, so they need to be taken in careful consideration. In this aspect, typical material defects usually studied from the mechanical point of view such as impurities, dislocations or lattice mismatch have consequences in the electrical behaviour of the device. The amount of unlinked bonds changes the way light is absorbed and charge carriers are generated; selecting the type and quantity of a certain impurity allows the tuning of the amount of charge carriers in the device, and lattice mismatches limit the compatibility between materials, among many other important issues regarding the crystalline structure, making semiconductors very dynamic materials. This is why nowadays the theoretical basis of many novel devices are designed but their construction is limited by challenges regarding the material.

Crystalline materials are periodic structures made up of identical building blocks. In order to define these structures two concepts are used: lattice and basis. The concept of lattice refers to a mathematical abstraction representing a set of spatial points forming a periodic structure, meaning the location of these basic building blocks, whereas the basis refers to an atom or group of atoms defining the periodically repeated structure [19]. A full representation of the material is then achieved by placing the basis to each position of the lattice, this is schematically represented in Fig. 2.1. Nevertheless, the concept of lattice is used in this thesis to express the temperature of the material as a solid (T_L).

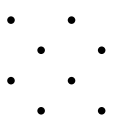

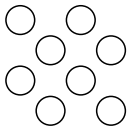
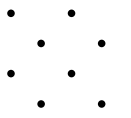

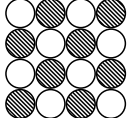
Lattice	Basis	Crystal
		
		

Figure 2.1: 2D Representation of lattice and basis concepts.

Being a periodic three-dimensional structure, any lattice point \mathbf{R}' can be obtained from other point \mathbf{R} using three vectors defined as \mathbf{a}_1 , \mathbf{a}_2 and \mathbf{a}_3 by the translation

$$\mathbf{R}' = \mathbf{R} + m_1\mathbf{a}_1 + m_2\mathbf{a}_2 + m_3\mathbf{a}_3, \quad (2.1)$$

where m_1 , m_2 and m_3 are integers; this called a Bravais lattice. There are 14 basic lattices

that are able to represent every crystalline material, these are defined by the primitive vectors shown in Eq.(2.1) and the angles α_{ii} between them. All these 3D lattice structures are shown in Fig.2.2, however all semiconductor materials have only cubic and hexagonal structures [20].

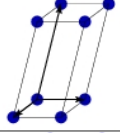
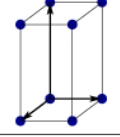
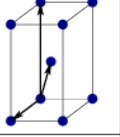
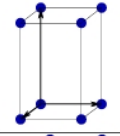
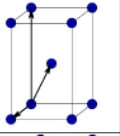
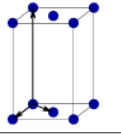
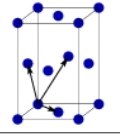
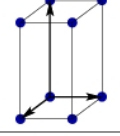
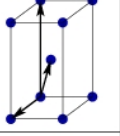
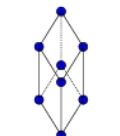
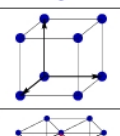
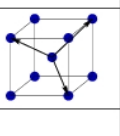
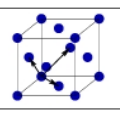
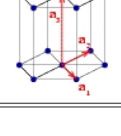
Bravais lattice	Parameters	Simple (P)	Volume centered (I)	Base centered (C)	Face centered (F)
Triclinic	$a_1 \neq a_2 \neq a_3$ $\alpha_{12} \neq \alpha_{23} \neq \alpha_{31}$				
Monoclinic	$a_1 \neq a_2 \neq a_3$ $\alpha_{23} = \alpha_{31} = 90^\circ$ $\alpha_{12} \neq 90^\circ$				
Orthorhombic	$a_1 \neq a_2 \neq a_3$ $\alpha_{12} = \alpha_{23} = \alpha_{31} = 90^\circ$				
Tetragonal	$a_1 = a_2 \neq a_3$ $\alpha_{12} = \alpha_{23} = \alpha_{31} = 90^\circ$				
Trigonal	$a_1 = a_2 = a_3$ $\alpha_{12} = \alpha_{23} = \alpha_{31} < 120^\circ$				
Cubic	$a_1 = a_2 = a_3$ $\alpha_{12} = \alpha_{23} = \alpha_{31} = 90^\circ$				
Hexagonal	$a_1 = a_2 \neq a_3$ $\alpha_{12} = 120^\circ$ $\alpha_{23} = \alpha_{31} = 90^\circ$				

Figure 2.2: Basic Bravais lattices.

For the specific case of electronics and optoelectronics most semiconductors have a face centered cubic (fcc) lattice with two atoms per basis in the positions $(0, 0, 0)$ and $(\frac{a}{4}, \frac{a}{4}, \frac{a}{4})$. When both atoms are identical it is called a diamond structure. Semiconductors such as Si, Ge or C have this crystal structure and are often referred to as elemental semiconductors. If the two atoms are of a different kind it is called a Zinc Blende structure, which is the one present in GaAs, AlAs and CdS among others; they are often called compound semiconductors. Figure 2.3 shows the crystal structure of GaAs. The rest of semiconductors with two-atom basis form the hexagonal closed pack (hcp) structure which is characteristic of BN, AlN, GaN and SiC, among others.

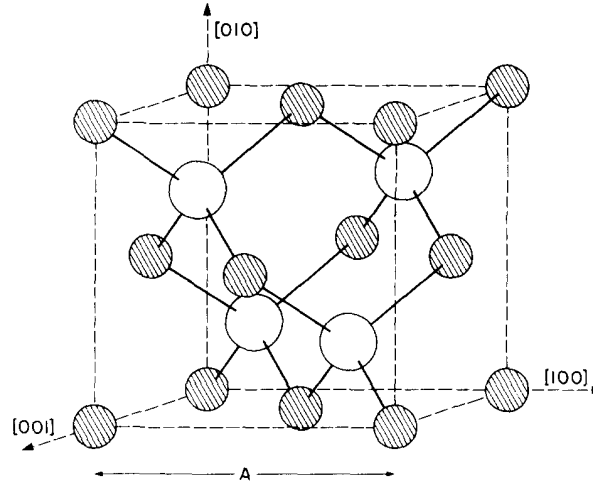


Figure 2.3: Conventional unit cube for GaAs [21].

2.1.2 Band Structure in Semiconductors

Crystalline structure gives semiconductor materials particular electrical properties. In order to understand them, it is necessary to analyze the behavior of electrons within the material. Given that a simple representation of the problem is a vast collection of particles travelling through a continuum media, it seems logical to describe it through classical physics (Newton's second law in particular), using a relation between particle's momentum, velocity and external perturbations. However, this approach fails given that at the scale of electronic interactions, quantum mechanics is needed for an accurate description. This is because in semiconductor devices electrons manifest their wave nature, which is actually the main reason for which these specific kinds of materials are useful for solar cells. The understanding of the relation between electronic energy levels of the material and incoming light energies is basic for design improvements and developing new technologies.

As in any physics problem, the level of simplification allowed depends on the particular context. For semiconductor physics there are many approaches that use quantum mechanics to describe electronic behaviour in a very detailed manner, sometimes even solving equations for every particle. However, for the scope of this research, effective descriptions can be made using macroscopic models and classical physics.

The Hydrogen Atom Problem

In order to take into account the duality of particles, Schrödinger derived an equation (1925) which describes the temporal evolution of a particle, in an analogue way to what Newton's second law would be for classical particles. For electrons, Schrödinger's equation can be written as

$$\left[-\frac{\hbar^2}{2m_0} \nabla^2 + V(r, t) \right] \Psi(r, t) = E \Psi(r, t), \quad (2.2)$$

where m_0 is the mass of the electron, \hbar is the reduced Planck's constant, E the energy value, $V(r, t)$ is the potential energy and $\Psi(r, t)$ the wave functions which are solutions to the equation. A posterior interpretation of the solution of this differential equation would interpret $\Psi(r, t)^* \Psi(r, t)$ as a probability density function for the particle. Another important result is that only certain energy states are allowed for a particle, while others are forbidden. Understanding where these energy levels are located is key for every semiconductor application.

Under specific conditions, an analytical solution for Eq.(2.2) can be obtained. This is the case of the very well studied hydrogen atom problem which consists of an electron and a proton under Coulombic interaction. Through separation of variables the wavefunction is described as a function of three quantum numbers n, l, m (not accounting for spin). The solution implies that the principal quantum number n defines the energy of the electronic levels, whose eigenvalues are

$$E_n = -\frac{\mu e^4}{2(4\pi\epsilon_0)^2 \hbar^2 n^2}, \quad (2.3)$$

where μ is the reduced mass, in this case approximated by the electron mass m_0 due to the much larger mass of the nucleus compared to the electron, e is the elementary charge and ϵ_0 is the vacuum permittivity. The principal quantum number n must not be mistaken with electron density expressed with the same letter through this document. This result shows that bounded electrons in an atom can take only discrete energy levels.

Density of States

As stated previously, an analysis of electron behavior within the material through a quantum mechanical description, allows to obtain an effective description through the use of classical mechanics. One step forward in this direction is to assume electrons as free particles moving in space, but having *effective properties*. Assuming the background potential for the solid as V_0 , then the time independent Schrödinger equation is

$$-\frac{\hbar^2}{2m} \left(\frac{\partial^2}{\partial x^2} + \frac{\partial^2}{\partial y^2} + \frac{\partial^2}{\partial z^2} \right) \psi(r) = (E - V_0) \psi(r). \quad (2.4)$$

A solution to this equation is

$$\psi(\mathbf{r}) = \frac{1}{\sqrt{V}} e^{\pm i\mathbf{k}\cdot\mathbf{r}}. \quad (2.5)$$

The particle's position is represented through the spatial vector \mathbf{r} , while \mathbf{k} is the wave-vector for the particle representing the state's periodicity. For a free particle, the relation between the momentum and the wave vector is given by

$$\mathbf{p} = \hbar\mathbf{k}, \quad (2.6)$$

which will help to build an effective description of the particle within the crystal. The corresponding energy when Eq.(2.5) is a solution for Eq.(2.4) is

$$E = \frac{\hbar^2 k^2}{2m} + V_0. \quad (2.7)$$

Note that $\frac{1}{\sqrt{V}}$ in Eq.(2.5) is a normalization factor that allows to define as a unity the probability of finding the particle in a volume V , in other words

$$\int_V d^3r |\psi(r)|^2 = 1. \quad (2.8)$$

However, the really interesting result is the macroscopic properties independent of the chosen volume V . For this purpose, two boundary conditions are assumed for the wave function over a volume that is considered as a cube of side L . First, it is assumed that the wave function goes to zero at the boundaries of the volume and second, periodicity is assumed as if the shape of the wave repeated identically across L sided cubes that make up the material. This allows to obtain the permitted values of k through the volume. It is rather simple then to use a control volume technique to calculate the number of electronic states available in the k -space region between k and $k + dk$, given the relation in Eq.(2.7). Finally, the possibility that the electrons have spin, multiplies by 2 the quantity of allowed states. This calculations result in the number of available electronic states per unit volume per unit energy for a given energy E . This is what is called the density of states (DOS) of the system which for free electrons in a 3D space, considering effective properties, is equal to

$$g(E) = \frac{\sqrt{2}m^{*3/2}(E - V_0)^{1/2}}{\pi^2\hbar^3}. \quad (2.9)$$

Analogue calculations can be made for 2 and 1 dimensional systems, which are of great importance in the study of quantum wells, wires or dots.

Particles in a Periodic Potential

A similar analysis to what is done for electrons in free space delivers the most important concept for semiconductor theory, the band structure. Given the periodic characteristic of crystals described in section 2.1.1 the material is represented as a periodic potential, hence, Schrödinger's equation becomes

$$\left[-\frac{\hbar^2}{2m_0} \nabla^2 + U(\mathbf{r}) \right] \psi(\mathbf{r}) = E\psi(\mathbf{r}) \quad (2.10)$$

where $U(\mathbf{r})$ is the background potential acting over the electrons. It is then considered that the potential has the same periodicity as the crystal and the wave function is spread through the material with an equal probability $\psi^*\psi$ in every cell of the crystal, considering that each cell is identical. In this case, Bloch's theorem states that the eigenfunctions of Schrödinger equation for a periodic potential are the product of a plane wave $e^{i\mathbf{k}\cdot\mathbf{r}}$ and a function $u_{\mathbf{k}(\mathbf{r})}$, which has the same periodicity as the periodic potential [22]. Therefore the solution for

Eq.(2.10) takes the form

$$\psi_{\mathbf{k}}(\mathbf{r}) = e^{i\mathbf{k}\cdot\mathbf{r}} u_{\mathbf{k}}(\mathbf{r}), \quad (2.11)$$

with $u_{\mathbf{k}}(\mathbf{r})$ having the same periodicity as the crystal. This is represented in Fig.2.4.

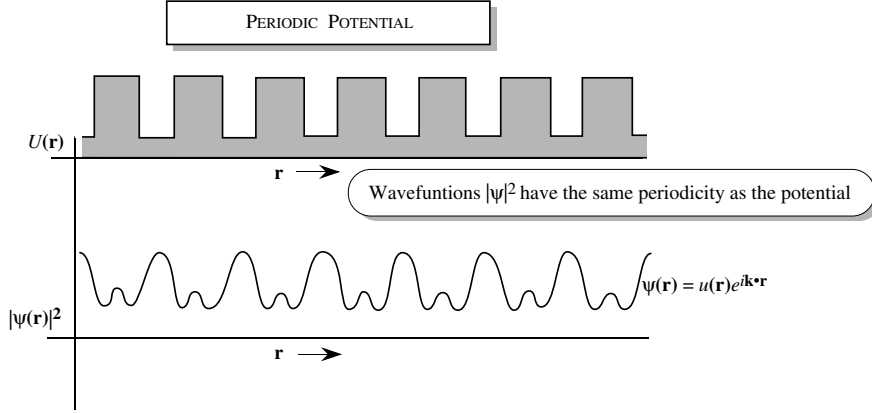


Figure 2.4: Periodic potential with the same periodicity as $|\psi|^2$ [22].

The fact of considering a periodic potential implies a difference in the allowed energies for electrons. By considering the potential for a single particle as a potential well given by Eq.(2.3), there are only discrete states allowed. If the same analysis is made for two potential wells the solution is two possible energies for the same quantum number. When the distance between them is made very large the solution is the same energy for both (degeneracy). This is the principle for understanding the formation of energy bands.

Using Bloch's theorem for a large number of particles affecting each other gives a continuum number of states (bands) separated by a gap which depends on the inter-atomic distance between particles. Figure 2.5 shows the variation of allowed energy levels considering a Silicon (diamond) crystalline structure. It can be observed that allowed energy states become discrete when the distance is large, and separated bands form for lower inter-atomic distances. The actual energy gap for Silicon at 200 K, meaning a lattice constant of 2.35 Å, is shown.

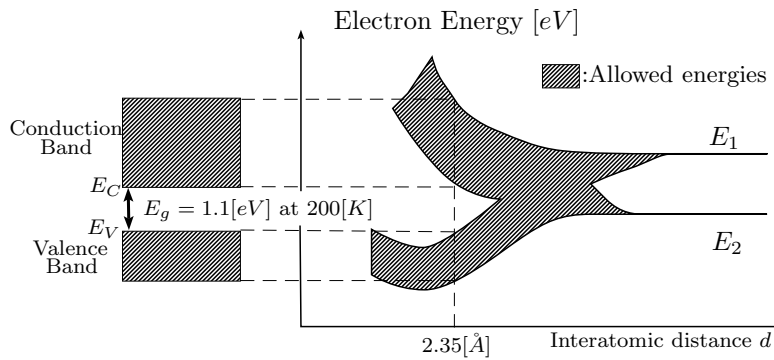


Figure 2.5: Formation of energy bands for electrons in a silicon crystal with a diamond-type lattice structure.

Energy Band Diagrams

A *reciprocal lattice* is an abstract construction made by vectors normal to a set of planes in the crystalline lattice. For any crystalline structure these vectors define primitive cells whose volume is inversely proportional to the one of the lattice. Using this inverse relation, they allow to visualize energy in k -space (given that $k = 2\pi/\lambda$). These primitive cells are called the Wigner-Seitz cells and are of great importance given that the wave's behaviour can be completely characterized within a single Wigner-Seitz cell, namely the first Brillouin zone. Any state for a given k of the particle will be a repetition of a point defined within this reciprocal space. The first Brillouin zone for fcc, diamond and zinc-blende structures is shown in Fig.2.6. The characteristics for this k -space lattice are defined by Γ for the origin and a capital letter for symmetry points depending on the crystal lattice; in the case of zinc-blende X, K, W, L . The vectors for reaching these points are defined by Λ, Δ and Σ .

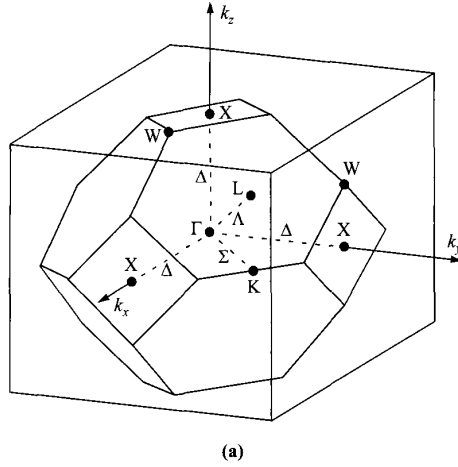


Figure 2.6: Brillouin zones for fcc diamond and zincblende lattices [23].

Considering the lattice structure as a series of periodic potentials, Bloch's theorem, Eq.(2.11) is used to find solutions for the energy levels, this is Kronig-Penney's model. Numerical methods are used to obtain the solutions of this model and the results are the allowed energy levels as a function of the k -vector. This means the energy states are allowed only above and below this forbidden region defined as the energy gap (E_g). Bands above the E_g are called conduction bands and the ones below valence bands. The bottom of the conduction band is designated as E_C while the top of the valence band E_V , hence

$$E_g = E_C - E_V. \quad (2.12)$$

The band structures of GaAs and Si are shown in Fig.2.7 as calculated by Chelikowsky and Cohen[24]. As it was previously stated, the product of reduced Planck's constant \hbar and the k -vector is the effective momentum of the particle. When the top of the valence band and the lowest point of the conduction band are located at the same value of \mathbf{k} , we refer to it as a direct gap semiconductor, an example of this is GaAs (left on Fig.2.7). Otherwise, an

indirect gap semiconductor has its maximum value of E_V and its minimum value of E_C at different values of \mathbf{k} , for instance Silicon (right on Fig.2.7).

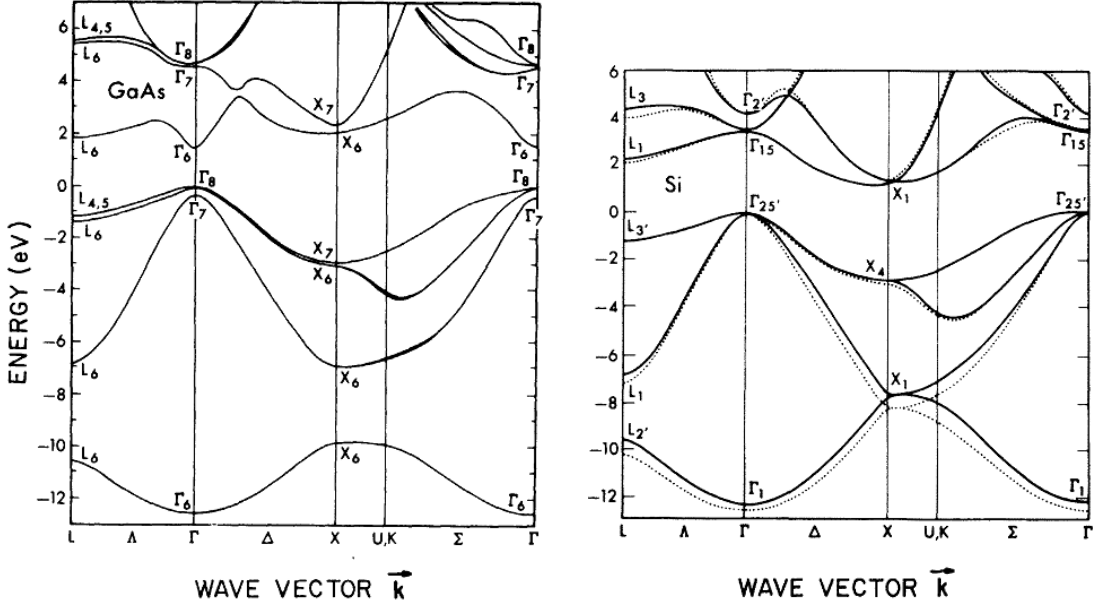


Figure 2.7: Calculated band structure of GaAs (left) and Silicon (right) [21].

The energy levels depend strongly on the distance between particles, which is in turn affected by the random motion of these, *i.e.* the temperature of the lattice. Several models describe the dependency of the bandgap energy in elemental or compound semiconductors and even for alloy materials. The most common model was established by Varshni [25], and is given by

$$E_g(T_L) = E_{g,0} - \frac{\alpha T_L^2}{\beta + T_L}, \quad (2.13)$$

where $E_{g,0}$ is the material bandgap at 0 K, α and β are coefficients dependent of the material and T_L is the lattice temperature. This model is considered to be valid for any peak-valley difference in semiconductors. In particular for GaAs it is important to know the level of the L -valley relative to that of the Γ -valley, given that electrons may be transferred from one valley to the other. These parameters are shown in Table 2.1 for GaAs and Si along with the value of the energy gap at room temperature $E_{g,300}$.

Table 2.1: Parameters for modeling bandgap energies [26].

Material	Valley	$E_{g,0}$ [eV]	α [eV/K]	β [K]	$E_{g,300}$ [eV]
Si	Γ	1.1695	$4.73 \cdot 10^{-4}$	636	1.124
GaAs	Γ	1.521	$5.58 \cdot 10^{-4}$	220	1.424
GaAs	L	1.815	$6.05 \cdot 10^{-4}$	204	1.699

Electrons and Holes in the Semiconductor

The concepts of conduction and valence bands arise from the difference between having an electron located at the energy levels above or below the energy gap. In the hypothetical case of a semiconductor at 0 K, the valence band is full and the conduction band is empty. This is because considering the crystal as a perfect structure, every electron forms a bond with its surrounding valence electrons and they cannot travel through the material, therefore there is no electrical conductivity. When the temperature increases there is sufficient energy for the bonds to be split and some electrons are free to carry charge, existing now in the conduction band. The fact that an electron is missing in the bond means there are unoccupied states in the valence band. If an electric field is applied to the material, electrons in the valence band will tend to move in the opposite direction to it and the only way they can achieve this is by forming and breaking bonds. This is equivalent to a positively charged pseudo-particle moving in the opposite direction and is defined as a hole. It is then considered that holes inhabit the valence band. Figure 2.8 shows the concept and displacement principle of holes. Both holes and electrons contribute to the conductivity in a separate way. This means they have to be treated as separated particles of opposite charge and if an effective description is made, it is also different for both.

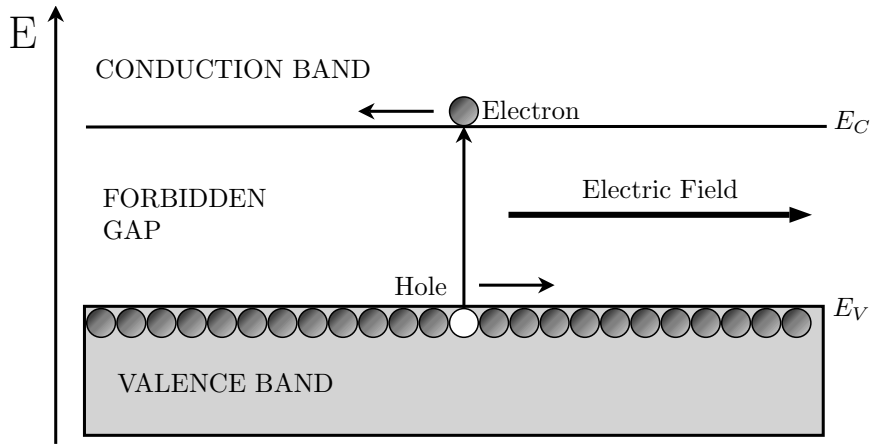


Figure 2.8: Schematic representation of electrons and holes.

Any energetic excitation that surpasses E_g will therefore liberate an electron into the conduction band leaving a hole in the valence band, this is why it is referred to as an *electron-hole pair* creation. The term charge carrier is used for electrons or holes indistinctly.

2.1.3 Effective Masses

In order to evaluate how charge carriers move, and considering the particle's duality, it is assumed they travel as a wave packet with a group velocity given by

$$\mathbf{v}_g = \frac{d\omega}{d\mathbf{k}}, \quad (2.14)$$

where ω is the angular frequency of the wavefunction of electrons which is related to their energy according to quantum mechanic's relation

$$E = h\nu = \hbar\omega, \quad (2.15)$$

where ν is the frequency of the wavefunction. The group velocity can be expressed in terms of energy by

$$\mathbf{v}_g = \frac{1}{\hbar} \nabla_{\mathbf{k}} E(\mathbf{k}). \quad (2.16)$$

This means that the equation of motion assuming the carrier as a free particle can be written as

$$\hbar \frac{d\mathbf{k}}{dt} = \mathbf{F},$$

where \mathbf{F} represents external forces acting over the particle. The value $\hbar\mathbf{k}$ represents the momentum of the particle, which is called the crystal momentum. Since crystal momentum accounts for internal potential effects within the material, it is used as an effective momentum and Newton's equation of motion may be used. Using the classical definition of momentum, we obtain the expression for a particle's effective mass,

$$m^* = \left[\frac{d^2 E}{dp^2} \right]^{-1} = \left[\frac{1}{\hbar^2} \frac{d^2 E}{dk^2} \right]^{-1}. \quad (2.17)$$

From Fig.2.7 it can be observed that the value for effective mass changes considerably as \mathbf{k} varies and can also have multiple values. Given the curvature of the valence band, Eq.(2.17) results in a negative value for holes. However, since their electrical charge is opposite to that of electrons, they can also be assumed to have positive effective mass. Near the Brillouin zone's symmetry points, electronic bands generally have a parabolic shape, this can also be appreciated in Fig.2.7. According to Eq.(2.17) this means the effective mass will have different but constant values for a neighbourhood around each symmetry point (m_{Γ} , m_L , m_X , etc.), given by

$$E(\mathbf{k}) = \frac{\mathbf{p}^2}{2m^*} = \frac{\hbar^2 |k|^2}{2m^*}. \quad (2.18)$$

This implies that one needs to use a combination of different masses depending on what it is used for. For the calculation of the DOS in the valence band the effective mass is characterized by three masses at the center of the Brillouin zone: light holes m_{pl} , heavy holes m_{ph} and the split-off sub band which is generally neglected. Anisotropy is another important effect to take into account. For the effective mass value for electrons there is contribution of transverse electron mass, m_{nt} , and longitude electron mass, m_{nl} .

These masses are generally expressed as a value scaled by the free electron mass m_0 . The value used in semiconductor simulations is generally the same as for the DOS calculations, which is obtained through a combination of the masses described above, depending whether it is a direct or indirect semiconductor. The expressions for the DOS effective mass of electrons

are [23]

$$m_{0,n} = \begin{cases} m_{\Gamma} & \text{for GaAs, InAs and InP.} \\ m_X = (m_{nt}^2 m_{nl})^{1/3} & \text{for Si, AlAs and GaP.} \\ m_L = (m_{nt}^2 m_{nl})^{1/3} & \text{for Ge, GaAs.} \end{cases} \quad (2.19)$$

where the sub-indexes in $m_{0,n}$ imply that temperature dependency is not being considered. On the other hand, the effective mass for holes is calculated for all materials using

$$m_{0,p} = \left(m_{pl}^{3/2} + m_{ph}^{3/2} \right)^{2/3}. \quad (2.20)$$

The parameters used for the calculation of the effective masses of Si and GaAs are shown in table 2.2 together with the calculated $m_{0,n}$ and $m_{0,p}$. Every given value is a scale factor of m_0 .

Table 2.2: Parameters for modeling effective masses [27, 28].

Material	m_{nt}	m_{nl}	m_{ph}	m_{pl}	$m_{0,n}$	$m_{0,p}$
Si	0.19	0.98	0.49	0.16	0.328	0.55
GaAs	0.229	1.987	0.49	0.08	0.067	0.49

Just as the energy gap and any variable depending on the energy bands, effective masses depend on temperature. The most common approach is to use a linear temperature dependency for all materials [29], the only exception is Silicon, in which the temperature dependence is better studied [27] and a parabolic approach is introduced for relative hole masses. The resulting effective mass m^* will be written as m_n and m_p for electrons and holes respectively (superscript * is omitted). The relations for obtaining the relative effective masses are

$$m_n = m_{0,n} + m_{1,n} \left(\frac{T_L}{300} \right), \quad (2.21)$$

$$m_p = m_{0,p} + m_{1,p} \left(\frac{T_L}{300} \right) + m_{2,p} \left(\frac{T_L}{300} \right)^2, \quad (2.22)$$

where T_L is expressed in $[K]$. Parameters $m_{0,n}$, $m_{1,n}$, $m_{0,p}$, $m_{1,p}$ and $m_{2,p}$ are detailed in Table 2.3 for Si and GaAs.

Table 2.3: Parameters for modeling temperature dependence of effective masses [27, 28].

Material	$m_{0,n}$	$m_{1,n}$	$m_{0,p}$	$m_{1,p}$	$m_{2,p}$
Si	0.321	0.009	0.55	0.6	-0.1
GaAs	0.067	-0.0036	0.49	0	0

2.1.4 Statistics at Equilibrium

According to the definitions for charge carriers previously described, they need to be treated as independent particles contributing separately to current conduction. We described how electrons occupy the conduction band and holes the valence band, however statistical properties for each carrier are required to define conduction properties, in order to perform semiconductor modeling. One of the most important results in device simulations is the population of each carrier whether it is under steady or unsteady conditions. In order to achieve this, the properties under equilibrium are established first. Using the effective masses, it is possible to obtain a statistical description of the occupation of the bands, as presented in this section.

Electron and Hole Density of States

In a similar way to what was done in section 2.1.2, Schrödinger's equation (SE) is used to obtain expressions for the density of states for each carrier. As was previously mentioned, an effective carrier mass is used for a given semiconductor, this greatly simplifies the analysis and permits to obtain a general expression using directly m_n and m_p . In this context, SE, Eq.(2.2) is solved for a pseudo-potential well where electrons can roam freely, generally described as a three dimensional box. As usual, the solutions to SE depend on vectors in the \mathbf{k} -space, which means there is a discrete number of solutions in proportion to \mathbf{k} . The most usual procedure to obtain the DOS is to represent every solution in the \mathbf{k} -space, where only one octant would gather every linearly independent solution. Since the number of possible solutions is large, a good approximation of the number of states can be achieved through integration of the volume in \mathbf{k} -space. For the density of number of states the relation between wave vector and energy is used and the number of states between E and $E + dE$ can be obtained. Taking in consideration the spin of the particle, the number of states are doubled. This procedure is very well described in [30]. The resulting expressions are very similar to Eq.(2.9),

$$g_C(E) = \frac{\sqrt{2}m_n^{*3/2} (E - E_C)^{1/2}}{\pi^2\hbar^3}, \quad (2.23)$$

$$g_V(E) = \frac{\sqrt{2}m_p^{*3/2} (E_V - E)^{1/2}}{\pi^2\hbar^3}, \quad (2.24)$$

where g_C and g_V are the density of states for electrons in the conduction band and holes in the valence band respectively.

Fermi Distribution

Knowing the density of states alone is not enough to determine the population of each carrier, since this only provides the amount of available states, not considering if they are occupied or not. To calculate the actual populations we need to know the ratio of filled to total allowed states for each given energy E . When thermal equilibrium is considered this ratio is expressed by the Fermi-Dirac distribution function $f(E)$ (often simply referred to as Fermi function),

given by

$$f(E) = \frac{1}{1 + e^{(E-E_F)/k_B T_L}}, \quad (2.25)$$

where k_B is Boltzmann's constant and E_F is the Fermi energy level. Figure 2.9 shows the Fermi distribution for different temperature values. The Fermi level E_F , or electrochemical potential, can be thought of a hypothetical energy level such that at thermodynamic equilibrium E_F would have 1/2 probability of being occupied. This is true for the Fermi distribution regardless the temperature of evaluation, as can be seen in Fig.2.9. For semiconductors, E_F will usually be located within the energy gap, and very near the middle for intrinsic semiconductors.

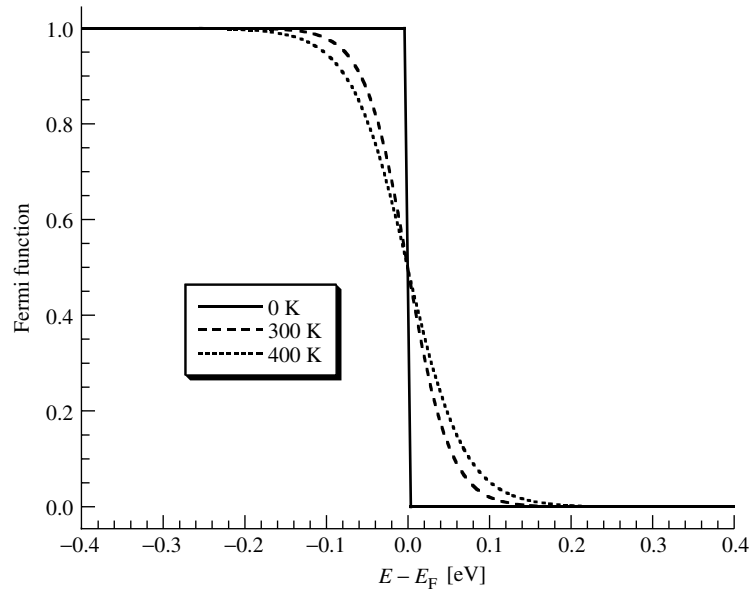


Figure 2.9: Value of Fermi function versus energy for different temperatures.

From Fig.2.9 it can be noticed that for 0 K the function is approximately a step function, which agrees with the idea that at absolute zero there are no electrons at the conduction band, nor holes in the valence band. Fermi distribution arises in a statistical manner from arranging a fixed number of particles into a system with constant energy where Pauli's exclusion principle is considered. This is why, relative to where E_F is located with respect to E_C and E_V , the distribution function will provide non zero values even if the E value is located within the energy gap (hence, there are no states available).

Doping

When a semiconductor material contains a negligible amount of impurity atoms it is said to be an intrinsic semiconductor. In an intrinsic material the population of electrons in the conduction band is equal to that of holes in the valence band. A very successful technique for manipulating electronic properties of semiconductors is by *doping* the material. This consists

in adding a controlled amount of specific impurities distributed in the sample which changes the total amount of electrons and/or holes population.

In the case of an intrinsic crystal of Silicon, electron and hole populations depend exclusively on temperature, since this is the only excitation mechanism provoking a rupture of the bonds. If an atom with an extra valence electron is added within the crystal, *e.g.* Antimony (Sb), all surrounding Si atoms will bond to it leaving an un-bonded electron that aids in conduction. Antimony is then said to be a *donor* atom. An analogue situation occurs when an atom with one valence electron less than those of the crystal, *e.g.* B from group III, is added. One bond will then be left un-linked and an extra hole is formed in the crystal. This impurity is then said to be an *acceptor*. Both processes are shown schematically in Fig.2.10.

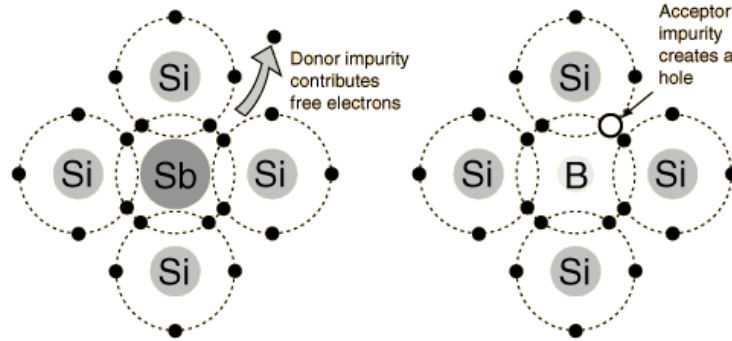


Figure 2.10: Schematic representation of doping process in Si.

When donors are added to a semiconductor it becomes an *n*-type semiconductor and the total density of impurities is denoted by N_D . If on the other hand acceptors are added in the material, a *p*-type semiconductor is formed and the total density of acceptors is N_A . If both kinds of impurities are added the type of the material will depend on which one of them is in major quantity. Even though the amount of electrons or holes is increased, charge neutrality is still maintained through the ionization (or charging) of the fixed donors or acceptors. Regardless the conservation of charge neutrality, the band structure of the material will shift because of the extra carriers in the corresponding bands, though E_g is maintained. Fermi level of intrinsic semiconductors is often referred to as E_i and used as a reference in doped materials where E_F moves. In *n*-type materials E_F will move closer to the conduction band, while in *p*-type materials E_F gets closer to the valence band edge. Relations for the energy displacements due to doping are specified in the following subsections.

Carrier Concentration at Equilibrium

Having Fermi's distribution function, it is evident that the calculation of each carrier's concentration at equilibrium can be achieved by means of the integration through the conduction and valence bands for electrons and holes respectively,

$$n_0 = \int_{E_C}^{\infty} g_C(E) f(E) dE = \frac{2N_C}{\sqrt{\pi}} F_{1/2}((E_F - E_C)/k_B T_L), \quad (2.26a)$$

$$p_0 = \int_{-\infty}^{E_V} g_V(E) [1 - f(E)] dE = \frac{2N_V}{\sqrt{\pi}} F_{1/2}((E_V - E_F)/k_B T_L), \quad (2.26b)$$

where Eqs.(2.23) and (2.24), and the Fermi function in Eq.(2.25) were replaced obtaining the effective density of states for each band given by

$$N_C = 2 \left(\frac{2\pi m_n^* k_B T_L}{h^2} \right)^{3/2}, \quad (2.27a)$$

$$N_V = 2 \left(\frac{2\pi m_p^* k_B T_L}{h^2} \right)^{3/2}. \quad (2.27b)$$

The factor $F_{1/2}(\eta)$ is the Fermi-Dirac integral of order 1/2 defined by

$$F_{1/2}(\eta) = \int_0^\infty \frac{\xi^{1/2} d\xi}{1 + e^{\xi - \eta}}. \quad (2.28)$$

An important approximation is made by using the fact that

$$\frac{2}{\sqrt{\pi}} F_{1/2}(\eta) \approx e^\eta \quad \text{for } \eta \leq -3, \quad (2.29)$$

which yields to replacing Fermi-Dirac's distribution by the simpler Maxwell-Boltzmann's distribution. With this a simple expression for equilibrium carrier concentration is achieved when the Fermi energy E_F is far from the band edges, more precisely at a distance $> 3k_B T_L$ within the gap. When this is the case, the semiconductor is said to be *non-degenerate*. If, on the other hand, E_F lies within $3k_B T_L$ from any band edge the semiconductor is referred to as *degenerate*. From Eq.(2.26), for electrons and holes respectively we get expressions for non-degenerate semiconductors

$$n_0 = N_C e^{(E_F - E_C)/k_B T_L}, \quad (2.30a)$$

$$p_0 = N_V e^{(E_V - E_F)/k_B T_L}. \quad (2.30b)$$

Intrinsic Carrier Concentration

Relations presented in the previous section are valid for every nondegenerate semiconductor and specifically for an intrinsic one, where the population of electrons n is equal to that of holes p . This means $n = p = n_i$, which is defined as the intrinsic carrier concentration, and the level of Fermi energy satisfies $E_F = E_i$. Regardless the level of the Fermi energy, for a nondegenerate semiconductor in equilibrium the product of its electron and hole populations will be a constant. Using Eq.(2.30) for an intrinsic semiconductor, relations for n_i are obtained; replacing them back, carrier densities at equilibrium can be defined in terms of n_i and E_F as

$$n_0 = n_i e^{(E_F - E_i)/k_B T_L}, \quad (2.31a)$$

$$p_0 = n_i e^{(E_i - E_F)/k_B T_L}. \quad (2.31b)$$

Given that the product of both expressions must be constant since we are considering equilibrium,

$$np = n_i^2. \quad (2.32)$$

Finally, using Eq.(2.30) an expression for n_i is obtained

$$n_i = \sqrt{N_C N_V} e^{-E_g/2k_B T_L}. \quad (2.33)$$

This expression allows to obtain the value of n_i as a function of material properties at a given temperature. Solving Eqs.(2.30) for an intrinsic semiconductor, where $n = p$, it is also very straight forward to obtain the intrinsic Fermi level

$$E_i = \frac{E_C + E_V}{2} + \frac{k_B T_L}{2} \ln \left(\frac{N_V}{N_C} \right), \quad (2.34)$$

which is usually very near to the middle of the bandgap. This can also be written in terms of carrier effective masses using Eqs.(2.27),

$$E_i = \frac{E_C + E_V}{2} + \frac{3}{4} k_B T_L \ln \left(\frac{m_p}{m_n} \right). \quad (2.35)$$

Doped Semiconductors at Equilibrium

In a doped semiconductor under equilibrium conditions, charge neutrality must still be maintained when no electric field is affecting the sample, thus

$$p - n + N_D^+ - N_A^- = 0,$$

where N_D^+ and N_A^- the concentration of ionized donors and acceptors respectively. The number of ionized impurities can be found using a Fermi distribution considering degeneracy factors, but for general purposes it can be considered that the vast majority of impurities are ionized and

$$p - n + N_D - N_A = 0. \quad (2.36)$$

This is often referred to as the charge neutrality relationship. When the semiconductor is non-degenerate Eq.(2.32) can be combined with with Eq.(2.36) to obtain each carrier density at equilibrium, for electrons

$$n_i^2/n - n + N_D - N_A = 0, \quad (2.37)$$

which is a quadratic equation that yields

$$n = \frac{N_D - N_A}{2} + \left[\left(\frac{N_D - N_A}{2} \right)^2 + n_i^2 \right]^{1/2}. \quad (2.38)$$

From a similar analysis, the density of holes p can be obtained

$$p = \frac{n_i^2}{n} = \frac{N_A - N_D}{2} + \left[\left(\frac{N_A - N_D}{2} \right)^2 + n_i^2 \right]^{1/2}. \quad (2.39)$$

In the extrinsic temperature region, which is range at which the carrier concentration is considered constant regarding temperature changes, all of the dopant carriers have been energized into the conduction band and there is very little thermal generation of additional carriers. For a highly doped semiconductor this means that $N_D \gg n_i$ for an n -type semiconductor and $N_A \gg n_i$ for a p -type semiconductor. Therefore, Eqs.(2.38) and (2.39) for an n -type semiconductor become

$$n \simeq N_D, \quad (2.40a)$$

$$p \simeq n_i^2/N_D, \quad (2.40b)$$

while for a p -type semiconductor they are approximated by

$$p \simeq N_A, \quad (2.41a)$$

$$n \simeq n_i^2/N_A. \quad (2.41b)$$

These approximations allow to obtain the Fermi energy level for doped semiconductors, which is given by

$$E_F - E_i = k_B T_L \ln(N_D/n_i) \quad \text{for an } n\text{-type}, \quad (2.42a)$$

$$E_i - E_F = k_B T_L \ln(N_A/n_i) \quad \text{for a } p\text{-type}. \quad (2.42b)$$

2.2 Carrier Transport Models

As discussed in Section 2.1, the use of an effective mass of charge carriers travelling within the semiconductor allows for a semi-classical description of their motion. Due to the large amount of mobile carriers within the materials, statistical approaches are often good enough to represent their behaviour. In this respect, Boltzmann's transport equation yields macroscopic models that vary in complexity depending on the approximations made regarding the specific problem. These models can be written in terms of several physical quantities, such as velocity, temperature or energy.

One of the most important aspects of modeling semiconductors is taking into account the scattering processes within the device. Unlike, for instance, a simple fluid problem, particles (charge carriers) can be destroyed and/or created while interacting with light, making collision processes dominant, specially for solar cells. This implies that different problems need different levels of accuracy and will need different mathematical models. The usual approach is to consider thermal equilibrium between lattice and charge carriers ($T_L = T_n = T_p$). This yields the well known drift-diffusion (DD) model, widely presented in literature

[22, 23, 30, 31].

Every macroscopic model relates carrier population to their movement and/or energy. Since electric potential is generally responsible (or a consequence) of this charge current, an additional expression is needed in order to relate its changes within the device and also to have a well posed mathematical model. For this purpose Poisson's equation is used, which is an electrostatic relation between the electric field and charge carrier densities.

All these relations are described briefly in this section. First, Poisson's equation for semiconductors is presented, followed by a description of Boltzmann's transport equation. The general version of the Hydrodynamic model is then derived, along with the corresponding approximations for scattering terms and energy flow, discussing the validity of each assumption. The energy balance used for the lattice temperature description is also presented. Finally, the Drift-Diffusion model is derived as a simplification of the Hydrodynamic model. A detailed and mathematically thorough description of several transport equations used in semiconductor device modeling is made by Jünger [32].

2.2.1 Poisson's Equation for Electrostatics

Poisson's equation relates charge distribution with the electrical potential through the device. It is one of the essential equations in electrostatics, derived from Gauss's law and given by

$$\nabla^2 V = -\nabla \cdot \mathbf{E} = -\frac{e}{\epsilon_s} (p - n + C), \quad (2.43)$$

where \mathbf{E} is the electric field, V the electric potential, ϵ_s the electric permittivity of the material and $C = C(\mathbf{r})$ denotes the doping profile which is space dependent and can have positive or negative values depending whether it is a p or n -type semiconductor.

2.2.2 Boltzmann's Transport Equation

In Section 2.1, expressions were derived for charge carrier concentrations at thermal equilibrium and no current flow. In a similar manner, a statistical approach is used in this section in order to obtain descriptions out of equilibrium.

A distribution function $f(\mathbf{r}, \mathbf{k}, t)$ is defined as the ratio of the number of occupied quantum states for an infinitesimal volume (in both real and k -space) to the total number of states. Since it can be considered as an occupation probability, $0 \leq f(\mathbf{r}, \mathbf{k}, t) \leq 1$ for any point $(\mathbf{r}, \mathbf{k}, t)$. As discussed previously, holes are considered to be particles moving independently to electrons, so any statistical estimate of their evolution will be analogue, only taking into account the differences in their effective properties. Hence, for simplicity, only the transport of electrons is considered below.

In a similar way as in subsection 2.1.4 for electrons in equilibrium, the total number of electrons in a certain volume $\text{vol}(\Omega)$ in the conduction band can be obtained through the

integration of infinitesimal momentum volumes $d\mathbf{k}$ in the Brillouin zone. Therefore, electron density n is obtained as units per volume as

$$n(\mathbf{r}, t) = \frac{1}{4\pi^3} \int_B f(\mathbf{r}, \mathbf{k}, t) d\mathbf{k}. \quad (2.44)$$

Electron density is then a macroscopic quantity obtained by means of the averaging of the distribution function through k -space. In the following, any averaged magnitude w , will be expressed using the notation

$$\langle w \rangle = \frac{1}{4\pi^3} \int_B w(\mathbf{k}) d\mathbf{k}, \quad (2.45)$$

and the electron concentration can be expressed as

$$n = \langle f \rangle. \quad (2.46)$$

In a similar way, we could express the mean velocity as

$$\mathbf{u} = \frac{1}{n} \langle \mathbf{v}_g f \rangle, \quad (2.47)$$

where $\mathbf{v}_g(\mathbf{k})$ is the group velocity defined in Eq.(2.16). This comes from the fact that particles have a random motion, defined in terms of a thermal velocity v_{th} , which contributes to the total kinetic energy, but not to the average displacement of the particle, therefore

$$\mathbf{v}_{th} = \mathbf{v}_g - \mathbf{u}, \quad (2.48)$$

which is in accordance with Eq.(2.47) because

$$\langle \mathbf{v}_{th} f \rangle = 0. \quad (2.49)$$

The average energy density is similarly defined as

$$\xi = \langle E f \rangle, \quad (2.50)$$

where E is given by the parabolic band approximation in Eq.(2.18). Since the group velocity is expressed as

$$\mathbf{v}_g(\mathbf{k}) = \hbar \mathbf{k} / m^*, \quad (2.51)$$

the mean velocity and energy, respectively become

$$n\mathbf{u} = \frac{1}{m^*} \langle \mathbf{p} f \rangle, \quad (2.52)$$

$$\xi = \frac{1}{m^*} \left\langle \frac{1}{2} |p|^2 f \right\rangle. \quad (2.53)$$

These expressions define the moments associated to f , being $\langle f \rangle$ the zeroth moment, $\langle \mathbf{p} f \rangle$

the first moment and $\langle |p|^2 f/2 \rangle$ the second moment. The quantities 1, \mathbf{p} and $|p|^2/2$ are called weight functions. These functions are used in the moments method when deriving balances for each macroscopic quantity.

Since $f(\mathbf{r}, \mathbf{k}, t)$ is considered to be out of equilibrium (opposite to the Fermi approximation), an equation that describes its evolution is needed. For this purpose, it is assumed that f is temporarily constant through a trajectory $(\mathbf{r}(t), \mathbf{k}(t))$, which means that if we follow a carrier as it moves in phase space, the probability of occupation does not change [33], then by the chain rule

$$\frac{Df}{Dt} = \partial_t f + \partial_t \mathbf{r} \cdot \nabla f + \partial_t \mathbf{k} \cdot \nabla_{\mathbf{k}} f. \quad (2.54)$$

Considering that the rate of change for f balances with the rate of change due to collisions, the collision operator is introduced

$$\frac{Df}{Dt} = (\partial_t f)_c, \quad (2.55)$$

which quantifies all the irreversible processes not included in the right hand-side part of Eq.(2.54). Under the semi-classical approach, the variation in the location of the particle, $\partial_t \mathbf{r}$, is equivalent to the particle's velocity, \mathbf{v} , which directly depends on momentum. In the same manner, the rate of change in momentum $\partial_t \mathbf{k}$, is caused mainly by electromagnetic forces. In this particular case the magnetic component is neglected. Therefore, Eq.(2.55) can be written as

$$\partial_t f + \mathbf{v}(\mathbf{k}) \cdot \nabla f + \frac{q}{\hbar} \nabla V(\mathbf{r}) \cdot \nabla_{\mathbf{k}} f = (\partial_t f)_c, \quad (2.56)$$

which is Boltzmann's transport equation (BTE) for semiconductors. When thermal equilibrium is considered, f is equal to the Fermi-Dirac distribution, and is a solution for Eq.(2.56). Moreover, when the semiconductor is non-degenerate and the Fermi energy is constant, the Maxwell-Boltzmann distribution can be used. However, under out-of-equilibrium conditions, a solution to BTE must be found. This is done in purely statistical methods, such as Monte-Carlo, where a considerable amount of computational resources are needed. Macroscopic models, in turn, allow for the use of averaged quantities as variables in a system of differential equations.

The most common approach to derive a macroscopic model starting from BTE is the method of moments. This method consists of multiplying BTE by weight functions and then integrating them over k -space, obtaining equations for macroscopic variables. The moment can be considered as the expected value of each random variable, so different weight functions deliver different expressions for each variable. Using Eqs.(2.52) and (2.53), the zeroth, first and second moments are expressed in terms of the wave vector k as

$$m_0 = \langle \kappa_0 f \rangle = \langle f \rangle, \quad (2.57a)$$

$$m_1 = \langle \kappa_1 f \rangle = \left\langle \frac{\hbar \mathbf{k}}{m^*} f \right\rangle, \quad (2.57b)$$

$$m_2 = \langle \kappa_2 f \rangle = \left\langle \frac{\hbar^2 |k|^2}{2m^*} f \right\rangle, \quad (2.57c)$$

where κ_0 , κ_1 and κ_2 are the corresponding weight functions. The physical meaning of each moment would be the particle, momentum and energy densities respectively. Both drift-diffusion and hydrodynamic models can be obtained from BTE through the method of moments. These models are presented below, indicating the assumptions made for their derivation.

2.2.3 Hydrodynamic Transport Model

Hydrodynamic models arise from the need of less restrictive models than the usual DD model. One of the first versions of these transport equations was presented by Kjell Blotjekjaer in 1970 [34]. Under the statistical approach of using effective descriptions for charge carriers, it is possible to attain models of higher accuracy. The derivation of HD model through BTE using the method of moments requires some assumptions. These are

- Energy bands are approximated by a parabolic shape.
- Collision operators conserve mass, momentum and energy.
- Quantum effects are neglected (intracollisional field effect, collision broadening).

A thorough review of the suitability of these models was performed by Grasser *et al.* [35]. In the rest of this subsection, momentum and energy balances are presented as obtained from the method of moments, along with the consequent velocity and temperature differential equations derived from it.

Zeroth Moment - Continuity Equation

Multiplying BTE by the first weight function and integrating in \mathbf{k} -space, delivers a mass balance for electrons and holes given respectively by

$$\partial_t n + \nabla \cdot (n \mathbf{u}_n) = (\partial_t n)_c, \quad (2.58a)$$

$$\partial_t p + \nabla \cdot (p \mathbf{u}_p) = (\partial_t p)_c, \quad (2.58b)$$

which are called the charge continuity equations. The terms on the right-hand side of each equation are the collision terms, in the case of carriers they correspond to generation and recombination rates, discussed in Section 2.4. Since carriers are considered as moving particles, current flow density equals the particle density times the charge they transport times their velocity, and as discussed previously both electrons and holes contribute in a separate way to the total current, thus

$$\mathbf{J}_n = -en\mathbf{u}_n, \quad (2.59a)$$

$$\mathbf{J}_p = +ep\mathbf{u}_p. \quad (2.59b)$$

Considering the electron and hole currents, continuity equations, Eqs.(2.58), can be written as

$$\partial_t n - \frac{1}{e} \nabla \cdot (\mathbf{J}_n) = (\partial_t n)_c, \quad (2.60a)$$

$$\partial_t p + \frac{1}{e} \nabla \cdot (\mathbf{J}_p) = (\partial_t p)_c. \quad (2.60b)$$

The expressions for continuity, Eqs. (2.60), are part of any macroscopic model, whether it is DD, HD, energy transport, etc. Continuity equation for each carrier, Eqs.(2.60), are a simple mass conservation balance and can therefore be derived by using an infinitesimal control volume.

First Moment - Momentum Balance

Boltzmann's transport equation is multiplied by the first weight function $\kappa_1 = \hbar \mathbf{k}/m^*$ from Eq.(2.57b). Considering the expressions for linear momentum of each carrier \mathbf{p}_n and \mathbf{p}_p ,

$$\mathbf{p}_n = m_n n \mathbf{u}_n, \quad (2.61a)$$

$$\mathbf{p}_p = m_p p \mathbf{u}_p, \quad (2.61b)$$

for electrons and holes respectively, the average momentum density balance equations are obtained,

$$\partial_t (\mathbf{p}_n) + \nabla \cdot (\mathbf{p}_n \otimes \mathbf{u}_n) = en \nabla V - \nabla (nk_B T_n) + (\partial_t \mathbf{p}_n)_c, \quad (2.62a)$$

$$\partial_t (\mathbf{p}_p) + \nabla \cdot (\mathbf{p}_p \otimes \mathbf{u}_p) = -ep \nabla V - \nabla (pk_B T_p) + (\partial_t \mathbf{p}_p)_c. \quad (2.62b)$$

The left-hand side terms of these equations are the rate of change plus the outflow of momentum density. The right-hand side shows the effect of the force done by the electric field (drift) and by the electron or hole pressure, which corresponds to the diffusion term in Eq.(2.85). The last term on the right-hand side represents the rate of change in momentum due to collisions. The specific description of the collision terms is discussed in subsection 2.2.4.

Due to the assumption of a parabolic band structure, Eqs.(2.61) can be used and electron and hole momentum balance in terms of velocity (see appendix A) can be expressed as

$$\partial_t \mathbf{u}_n + \mathbf{u}_n \nabla \cdot \mathbf{u}_n = \frac{e}{m_n} \nabla V - \frac{k_B}{m_n n} \nabla (n T_n) + (\partial_t \mathbf{u}_n)_c, \quad (2.63a)$$

$$\partial_t \mathbf{u}_p + \mathbf{u}_p \nabla \cdot \mathbf{u}_p = -\frac{e}{m_p} \nabla V - \frac{k_B}{m_p p} \nabla (p T_p) + (\partial_t \mathbf{u}_p)_c. \quad (2.63b)$$

Second Moment - Energy Balance

In a similar way, multiplying BTE by the second weight function given by Eq.(2.57c), the second moment delivers a balance for energy density ξ . For electrons, we define

$$\xi_n = \frac{3}{2}nk_B T_n + \frac{m_n}{2}nu_n^2, \quad (2.64)$$

where $u_n^2 = \mathbf{u}_n \cdot \mathbf{u}_n$ and an analogue expression is defined for holes. BTE then yields

$$\partial_t \xi_n + \nabla \cdot (\xi_n \mathbf{u}_n) = en\mathbf{u}_n \cdot \nabla V - \nabla \cdot (nk_B T_n \mathbf{u}_n) - \nabla \cdot (n\mathbf{Q}_n) + (\partial_t \xi_n)_c, \quad (2.65a)$$

$$\partial_t \xi_p + \nabla \cdot (\xi_p \mathbf{u}_p) = -ep\mathbf{u}_p \cdot \nabla V - \nabla \cdot (pk_B T_p \mathbf{u}_p) - \nabla \cdot (n\mathbf{Q}_p) + (\partial_t \xi_p)_c. \quad (2.65b)$$

The left-hand side of Eq.(2.65) represents the rate of change of energy $\partial_t \xi_{n(p)}$, plus the outflow of kinetic energy density $\nabla \cdot (\xi_{n(p)} \mathbf{u}_{n(p)})$. On the right-hand side, the term $en(p)\mathbf{u}_{n(p)} \cdot \nabla V$ is the energy delivered by the electric field, $\nabla \cdot (n(p)k_B T_{n(p)} \mathbf{u}_{n(p)})$ is the work performed by electron or hole pressure, $(\partial_t \xi_{n(p)})_c$ is the change in kinetic energy attributed to collisions and $\nabla \cdot (n\mathbf{Q}_{n(p)})$ is the heat flow density. The choice of $\mathbf{Q}_{n(p)}$ has been widely discussed and is reviewed in subsection 2.2.5.

Using the definition of energy density in Eq.(2.64), energy balances from Eqs.(2.65) can be rewritten in terms of only carrier density, velocity and temperature (see appendix A) as

$$\partial_t T_n + \mathbf{u}_n \cdot \nabla T_n + \frac{2}{3}T_n \nabla \cdot \mathbf{u}_n + \frac{2}{3k_B n} \nabla \cdot (n\mathbf{Q}_n) = (\partial_t T_n)_c, \quad (2.66a)$$

$$\partial_t T_p + \mathbf{u}_p \cdot \nabla T_p + \frac{2}{3}T_p \nabla \cdot \mathbf{u}_p + \frac{2}{3k_B p} \nabla \cdot (p\mathbf{Q}_p) = (\partial_t T_p)_c, \quad (2.66b)$$

where energy flux nor collision terms are specified.

2.2.4 Scattering Approximations

The equations presented for the HD model have generic collision or scattering terms which are different for the specific problem context and are generally simplified. The complete expressions along with the expressions used for this work are presented below. For Eqs.(2.63) and (2.66) it is simpler and safer to derive the collision terms as a function of momentum (\mathbf{p}) and kinetic energy (ξ) rather than velocity (\mathbf{u}) and temperature (T), respectively [34]. Therefore, the collision terms for electrons are expressed as:

$$(\partial_t \mathbf{u}_n)_c = \frac{1}{m_n n} (\partial_t \mathbf{p}_n)_c - \frac{\mathbf{u}_n}{n} (\partial_t n)_c, \quad (2.67)$$

$$(\partial_t T_n)_c = \frac{2}{3nk_B} (\partial_t \xi_n)_c - \frac{2\mathbf{u}_n}{3nk_B} \cdot (\partial_t \mathbf{p}_n)_c + \left(\frac{m_n u_n^2}{3nk_B} - \frac{T_n}{n} \right) (\partial_t n)_c. \quad (2.68)$$

Analogue relations are obtained for holes. Then, the collision terms need to be derived for density, momentum and energy, and will be obtained consequently for velocity and temperature.

Carrier Density Collision Terms

For electrons and holes, time variation of the carriers is expressed as source and sink terms, meaning carriers moving between the valence and conduction bands. This is represented as generation and recombination terms $G_{n(p)}(x)$, $R_{n(p)}(x)$, presented in detail in Section 2.4,

$$(\partial_t n)_c = G_n - R_n, \quad (2.69a)$$

$$(\partial_t p)_c = G_p - R_p. \quad (2.69b)$$

Momentum and Velocity Collision Terms

The change of momentum accounts for both inter and intra-band phenomena. Interband momentum changes are due to generation and recombination, while the rest of the scattering processes, namely carrier-lattice, electron-hole or carrier-carrier collisions are expressed using the relaxation time approximation. With this, we can express momentum changes for electrons and holes respectively as

$$(\partial_t \mathbf{p}_n)_c = \frac{\Delta \mathbf{p}_{ne-l}}{\tau_{m,n}} + \frac{\Delta \mathbf{p}_{ne-h}}{\tau_{eh}} + \frac{\Delta \mathbf{p}_{ne-e}}{\tau_{ee}} + \frac{\mathbf{p}_n}{n} (\partial_t n)_c, \quad (2.70a)$$

$$(\partial_t \mathbf{p}_p)_c = \frac{\Delta \mathbf{p}_{ph-l}}{\tau_{m,p}} + \frac{\Delta \mathbf{p}_{pe-h}}{\tau_{eh}} + \frac{\Delta \mathbf{p}_{ph-h}}{\tau_{hh}} + \frac{\mathbf{p}_p}{p} (\partial_t p)_c, \quad (2.70b)$$

where $\tau_{m,n}$, $\tau_{m,p}$, τ_{eh} , τ_{ee} and τ_{hh} are the relaxation times for electron-lattice, hole-lattice, electron-hole, electron-electron and hole-hole collisions respectively. Each relaxation time defines a momentum interchange rate between the carriers and a corresponding final state. For changes of momentum due to carrier-lattice collisions, it is considered that all the momentum is given to the lattice, hence the final momentum is zero. On the other hand, in electron-hole collisions the linear momentum ($m^* \mathbf{u}$) changes at a rate τ_{eh} towards the linear momentum of the other particle, similarly for carrier-carrier interactions.

Electron-hole scattering is usually neglected because high concentrations of different carriers are seldom present at the same time, given that electronic devices frequently use doped semiconductors. Collisions between carriers of the same type can occur at a higher rate, but are neglected since they do not change the total amount of momentum under macroscopic considerations. Nevertheless, they do randomize the momentum, affecting other scattering mechanisms. This effect is normally handled as a modification to the expected phonon and ionized impurity scattering [30].

With these assumptions, considering constant effective mass and hence expressing momentum as a function of carrier velocity, momentum changes due to scattering effects are approximated

by

$$(\partial_t \mathbf{p}_n)_c = -\frac{m_n n \mathbf{u}_n}{\tau_{m,n}} + \frac{\mathbf{p}_n}{n} (\partial_t n)_c, \quad (2.71a)$$

$$(\partial_t \mathbf{p}_p)_c = -\frac{m_p p \mathbf{u}_p}{\tau_{m,p}} + \frac{\mathbf{p}_p}{p} (\partial_t p)_c. \quad (2.71b)$$

The momentum relaxation time τ_m is a difficult parameter to measure experimentally, but it is closely related to the carrier mobility, as can be seen from Eq.(2.81). This is why empirical relations are usually obtained for mobility in terms of other variables, linked to the scattering mechanisms in consideration. The models used for this work are presented in Section 2.3. Given that HD models normally use τ_m instead of μ , it is important to detach the effects of each scattering process and identify whether the changes are occurring due to the effective mass or the average time between collisions. Finally, using the expression from Eq.(2.67), collision terms are expressed as a function of carrier velocities as

$$(\partial_t \mathbf{u}_n)_c = -\frac{\mathbf{u}_n}{\tau_{m,n}}, \quad (2.72a)$$

$$(\partial_t \mathbf{u}_p)_c = -\frac{\mathbf{u}_p}{\tau_{m,p}}. \quad (2.72b)$$

Carrier Energy and Temperature Collision Terms

The energy of carriers is transferred to an equilibrium system with a reference temperature T_0 , which in this case is assumed as the lattice temperature T_L . Considering energy variation due to interband processes and using the relaxation time approximation yields

$$(\partial_t \xi_n)_c = \frac{\Delta \xi_{el}}{\tau_{\epsilon,n}} + \frac{\xi_n}{n} (\partial_t n)_c = -\frac{\left(\xi_n - \frac{3}{2} k_B n T_L\right)}{\tau_{\epsilon,n}} + \frac{\xi_n}{n} (\partial_t n)_c, \quad (2.73)$$

where $\tau_{\epsilon,n}$ is the energy relaxation time for electrons. There is an analogue expression for holes. Then, using Eq.(2.64) for the electron energy density (and the corresponding one for holes), energy collision terms are

$$(\partial_t \xi_n)_c = -\frac{n}{\tau_{\epsilon,n}} \left(\frac{3}{2} k_B (T_n - T_L) + \frac{1}{2} m_n u_n^2 \right) + \frac{\xi_n}{n} (\partial_t n)_c, \quad (2.74a)$$

$$(\partial_t \xi_p)_c = -\frac{p}{\tau_{\epsilon,p}} \left(\frac{3}{2} k_B (T_p - T_L) + \frac{1}{2} m_p u_p^2 \right) + \frac{\xi_p}{p} (\partial_t p)_c. \quad (2.74b)$$

The energy relaxation time is usually a function of both carrier and lattice temperature, as demonstrated in Section 2.3. Equations (2.74), (2.71), (2.69) and (2.68) are combined to obtain the complete thermal collision terms, giving

$$(\partial_t T_n)_c = -\frac{(T_n - T_L)}{\tau_{\epsilon,n}} + \frac{2m_n u_n^2}{3k_B \tau_{m,n}} \left(1 - \frac{\tau_{m,n}}{2\tau_{\epsilon,n}} \right), \quad (2.75a)$$

$$(\partial_t T_p)_c = -\frac{(T_p - T_L)}{\tau_{\epsilon,p}} + \frac{2m_p u_p^2}{3k_B \tau_{m,p}} \left(1 - \frac{\tau_{m,p}}{2\tau_{\epsilon,p}}\right), \quad (2.75b)$$

for electrons and holes respectively.

2.2.5 Heat Flow Approximation

When using the method of moments, every equation obtained for a moment through its corresponding weight function will have a higher hierarchy term that will need to be obtained through the next moment, or through approximation. This is a closure problem that needs to be solved considering the level of detail required for the specific simulation. In this way, Drift-diffusion model arises from the first two moments and considering thermal equilibrium for the higher order terms. On the other hand, hydrodynamic models need considerations regarding the average energy flow for electrons, $n\mathbf{S}_n$, given by

$$n\mathbf{S}_n = \langle \mathbf{v}_g E f \rangle. \quad (2.76)$$

Using the definition of the particle's group velocity \mathbf{v}_g , the average energy flow can be expressed as

$$n\mathbf{S}_n = n\mathbf{Q}_n + (\xi_n + nk_B T_n) \mathbf{u}_n + \frac{u_n^2}{2} \langle m_n \mathbf{v}_{th} f \rangle. \quad (2.77)$$

where heat flux density $n\mathbf{Q}_n$ is used, which is given by definition as

$$n\mathbf{Q}_n = \left\langle \frac{1}{2} m_n v_{th}^2 \mathbf{v}_{th} f \right\rangle. \quad (2.78)$$

The last term in Eq.(2.77) is usually neglected even for non parabolic bands approximations [36]. Average energy flow is then made up by a convective energy flux density ($(\xi_n + nk_B T_n) \mathbf{u}_n$) and heat flux density ($n\mathbf{Q}_n$) terms. Therefore, in order to obtain a solution of the model, heat flux needs to be approximated in terms of the rest of the variables that comprise the system of equations. The most common approximation is through the use of a thermal conductivity according to Fourier's law, as

$$n\mathbf{Q}_n = -\kappa_n \nabla T_n, \quad (2.79)$$

with an analogous relation for holes. This choice has been criticized given that $\kappa \nabla T$ only approximates the diffusive component of heat flux [32], though many times even the total energy flux is represented using Fourier's law. Some authors, such as Anile and Romano [37], present more complex expressions but also justify the use of Fourier's law under certain circumstances.

Carrier thermal conductivities κ_n and κ_p are sometimes considered to be constant. However, a better approximation arises from assuming they obey a generalized Wiedemann-Franz law

[11],

$$\kappa_n = \left(\frac{5}{2} + r\right) \left(\frac{k_B}{e}\right)^2 \sigma_n T_n, \quad (2.80a)$$

$$\kappa_p = \left(\frac{5}{2} + r\right) \left(\frac{k_B}{e}\right)^2 \sigma_p T_p, \quad (2.80b)$$

where σ_n and σ_p are the electrical conductivities of electrons and holes respectively. The factor r relates carrier temperature (or energy) changes with changes in energy relaxation time. A usual estimate is $r = -1$. As discussed in Section 2.3, electrical conductivity depends mainly on carrier mobilities, μ_n and μ_p , which describe electronic displacement due to an electric field,

$$\mu_n = \frac{e\tau_{m,n}}{m_n}, \quad (2.81a)$$

$$\mu_p = \frac{e\tau_{m,p}}{m_p}. \quad (2.81b)$$

Given the relation between mobility, electric field and current, the conductivity of the material is often presented, analogously to ohm's law, as

$$\sigma = \sigma_n + \sigma_p = en\mu_n + ep\mu_p. \quad (2.82)$$

With this, thermal conductivities are expressed as

$$\kappa_n = \frac{3}{2} \frac{k_B^2}{e} T_n \mu_n n, \quad (2.83a)$$

$$\kappa_p = \frac{3}{2} \frac{k_B^2}{e} T_p \mu_p p. \quad (2.83b)$$

These expressions are normally used when studying velocity overshoot or hot carriers in semiconductors.

2.2.6 Lattice Energy Balance

Many times when solving hydrodynamic models the lattice temperature is considered to be constant through the device. This is justified by the assumption that the lattice acts as a heat sink for charge carriers, and the energy they deliver to the lattice does not generate large temperature differences, even though electrons and holes could easily reach temperatures an order of magnitude higher than that of the lattice.

The energy balance equation for lattice temperature comprises the heat equation for acoustic phonons, meaning that heat transfer to the lattice occurs directly through this method and optical phonon emission is only considered indirectly. Therefore, lattice is heated through car-

rier thermalization and Joule heating, both estimated by relaxation-time approximation,

$$C_L \partial_t T_L = \nabla \cdot (\kappa_L \nabla T_L) + \frac{3k_B n}{2} \left(\frac{T_n - T_L}{\tau_{E,n}} \right) + \frac{3k_B p}{2} \left(\frac{T_p - T_L}{\tau_{E,p}} \right) + \frac{nm_n u_n^2}{2\tau_{E,n}} + \frac{pm_p u_p^2}{2\tau_{E,p}}. \quad (2.84)$$

2.2.7 Drift-Diffusion Transport Model

Drift-diffusion equations are the most used equations in semiconductor modeling. They were first derived by Van Roosbroeck [38] in 1950. The main assumptions for the derivation of this model are the following:

- Energy bands are described by a parabolic approximation.
- The semiconductor is non-degenerate. This means linear collision operators are used.
- The mean free path is very small compared to the device diameter.
- Thermal equilibrium between carriers and lattice ($T_n = T_p = T_L$).

Considering these assumptions, the first moment of BTE delivers a momentum conservation equation given by

$$k_B T_L \nabla n - en \nabla V = (\partial_t \mathbf{P}_n)_c. \quad (2.85)$$

From the second assumption, the collision operator for momentum is estimated using a relaxation time approximation as

$$(\partial_t \mathbf{P}_n)_c = -\frac{\mathbf{P}_n}{\tau_{m,n}}, \quad (2.86)$$

where $\tau_{m,n}$ is the relaxation time for electrons. Using the first assumption, *i.e.* parabolic bands, the average momentum of electrons can be expressed according to Eq.(2.61) and an expression for electron average velocity can be obtained

$$\mathbf{u}_n = \frac{e\tau_{m,n}}{m_n} \nabla V - \frac{k_B T_L \tau_{m,n}}{m_n} \frac{\nabla n}{n}. \quad (2.87)$$

The term next to the gradient of density is denoted as the diffusion constant, given by

$$D_n = \frac{k_B T_L \tau_{m,n}}{m_n}, \quad (2.88)$$

which is more often expressed in terms of mobility as

$$D_n = \frac{k_B T_L}{e} \mu_n, \quad (2.89a)$$

$$D_p = \frac{k_B T_L}{e} \mu_p, \quad (2.89b)$$

namely Einstein's relation. These equations are analogue for holes, with the exception of having opposite charge ($+e$). Therefore, using Eqs.(2.87) and (2.59), expressions for current density of electrons and holes are obtained,

$$\mathbf{J}_n = e(D_n \nabla n - \mu_n n \nabla V), \quad (2.90a)$$

$$\mathbf{J}_p = -e(D_p \nabla p + \mu_p p \nabla V), \quad (2.90b)$$

which are the drift-diffusion current equations. These expressions combined with Eq.(2.60) and Eq.(2.43) complete the Drift-Diffusion model. Note that the expressions for current, Eqs.(2.90), are used directly in Eqs.(2.60) and the system has one variable less. The usual derivation of DD equations is conceptually more graphic and develops separately the contribution of the electric field (*drift*) and concentration gradient (*diffusion*). It can be found in detail in any basic semiconductor physics books [22, 23, 30].

2.3 Mobility and Relaxation Times

Carrier mobility characterizes the motion of a charge carrier particle, with respect to the magnitude of the electric field. Because of this, mobility is usually studied under conditions where only an electric field generates an electrical current, which can therefore be written as

$$\mathbf{J}_n \approx \mathbf{J}_{n,\text{drift}} = qn\mathbf{u}_{n,\text{drift}}, \quad (2.91)$$

for electrons, where $\mathbf{u}_{n,\text{drift}}$ is the electron drift velocity caused by the effect of the electric field, given by

$$\mathbf{u}_{n,\text{drift}} = \mu_n \mathbf{E}. \quad (2.92)$$

At low fields, mobility is considered to be constant, having a linear relation between velocity and electric field. This can be observed in Fig.2.11, where electron and hole drift velocities are depicted for GaAs and Si as a function of electric field, considering a constant temperature of $T_L = 300$ K and thermal equilibrium.

Many analytical and experimental studies have been made, obtaining empirical relations for the dependence of low-field mobility with material doping and temperature. The results of some of these studies are presented in this section.

According with expressions in Eqs.(2.81), mobility is also a relation between the average time between scattering events (or momentum relaxation time) τ_m , effective mass m^* and electrical charge of the particle e . Consequently, if mobility is constant, τ_m is also considered constant, given that for a specific temperature the effective mass has a constant value given by Eq.(2.21), and the electrical charge is always constant.

As the electric field increases, the relation with drift velocity ceases to be linear, and $\mathbf{u}_{n,\text{drift}}$ generally reaches asymptotically a constant value, as can be seen in the behaviour of Silicon

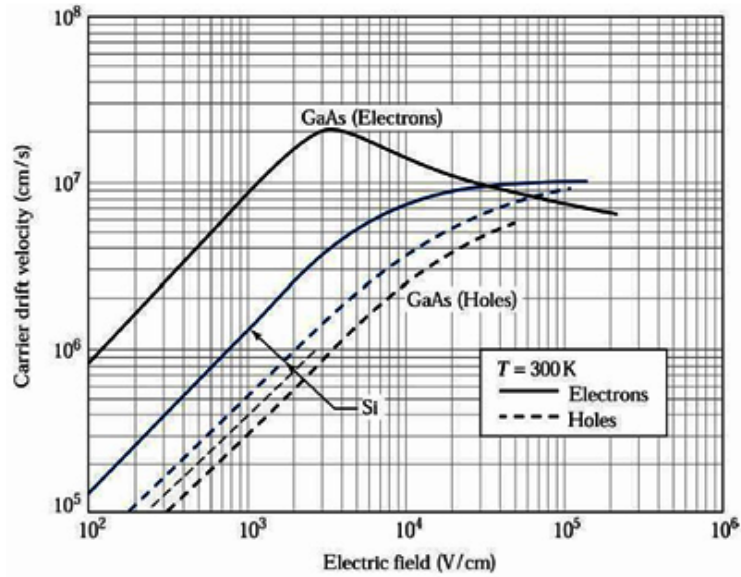


Figure 2.11: Drift velocity of carriers in high purity Si and GaAs as a function of the applied electric field at $T = 300[K]$ [30].

in Fig.2.11. This effect is caused by a decrease in τ_m generated by an increase on the average number of collisions, and a more efficient energy transfer generated by optical phonon emission. The decrease in $\mathbf{u}_{n,\text{drift}}$ is even greater for some semiconductors like GaAs, where carriers even slow down as the field is increased, meaning there is a negative differential mobility. This behaviour is due to a phenomenon called *transferred electron effect*. As explained in the present section, this effect causes mobility to change because of changes in τ_m , but also in the effective mass m^* . Therefore, special attention needs to be paid when using HD models, where τ_m and m^* describe the motion of carriers, rather than μ .

Relations that describe these variations of mobility as a function to carrier temperatures have been presented, in order to take into account these high field (or more generally, high energy) effects. Since the focus of this work is upon hot-carrier behaviour, these carrier temperature dependent models will be compared in order to find out which is the most appropriate for the modeling of hot-carriers.

2.3.1 Lattice Mobility

One of the main sources of carrier scattering is due to collisions with the crystal lattice. Considering an undoped material at low fields, as temperature increases atoms vibrate more with respect to their equilibrium positions. This effect increases the probability of collisions with moving charge carriers. This is referred to as phonon scattering and its effect is normally fitted by an exponential expression with respect to a reference state, given by

$$\mu^L = \mu_{300}^L \left(\frac{T_L}{300} \right)^{\gamma_0}, \quad (2.93)$$

where μ_{300}^L is the carrier mobility at $T_L = 300$ K and γ_0 is the fitting factor with a negative value given the inverse relation between mobility and carrier temperature. This relation is valid for both electrons and holes. Parameters for this relation are listed in Table 2.4 for GaAs and Si.

Table 2.4: Parameters for modeling temperature dependence of carrier mobility

Material	Carrier	$\mu_{300}^L [cm^2/Vs]$	γ_0	Ref
Si	n	1448	-2.33	[39]
	p	472.8	-2.23	
GaAs	n	9400	-2.1	[40]
	p	491.5	-2.2	

2.3.2 Mobility Degradation by Impurities

Regardless that the expression in Eq.(2.93) is valid only for intrinsic materials, it is often coupled to other empirical relations to account for impurity scattering. Doped materials contain a large number of distributed charges within them, making the carrier concentrations increase greatly compared to that of intrinsic materials, and also making the number of collisions of these carriers increase, degrading their mobility.

As well as degradation due to phonon scattering, impurity scattering in semiconductors is temperature dependent. Near thermal equilibrium, an increase in temperature is directly related to an increase in carrier thermal velocity which means it is less likely that carriers spend time near an impurity and consequently mobility increases. This effect is opposite when the impurity concentration increases, hence, any empirical relation starts from the basis that mobility degradation due to impurities increases with impurity concentration and decreases with temperature. This opposite behaviour makes highly doped materials far less sensitive to temperature changes.

If only one effect is considered at the time, mobilities sum up according to Matthiessen's rule, meaning that if μ^L is the carrier mobility due to lattice scattering and μ^I is the mobility only accounting for impurities, then

$$\mu^{LI} = \left(\frac{1}{\mu^L} + \frac{1}{\mu^I} \right)^{-1}, \quad (2.94)$$

is the total mobility accounting for both effects. Matthiessen's rule is used because mobility can be thought of as a measure of the resistance to the movement of the particle, thus each contribution sums up as parallel resistances in an electric circuit. For instance, a very frequent approximation for impurity scattering in Silicon is given by Masetti *et al.* [41] which considers the effect of different doping impurities, improving earlier models. Even though this is valid only for a temperature of 300 K it is often used as default model in device simulators such as Sentaurus by SYNOPSIS®.

Although this is useful when considering different sources of scattering independently, other empirical fits usually consider both effects at once. Already in 1967 Caughey and Thomas [42] developed an empirical model to account for impurity effects in Silicon, this model has been widely used and adjusted for other materials. This relation states that electron or hole mobility is given by

$$\mu^{LI} = \mu^{\min} + \frac{\mu^L - \mu^{\min}}{1 + \left(\frac{C}{N^{\text{ref}}}\right)^{\alpha^I}}, \quad (2.95)$$

where μ^L is the phonon dependent mobility as given by Eq.(2.93), C is the doping concentration, μ^{\min} a minimum value for mobility at high doping values, N^{ref} a reference doping concentration and α^I an adjustable parameter for the doping dependence. Since Caughey and Thomas presented this expression not accounting for temperature changes, a common approach is to adjust μ^{\min} , N^{ref} and α^I in a similar way as μ^L having each a different exponent, thus can be written as

$$\mu^{\min} = \mu_{300}^{\min} \left(\frac{T_L}{300}\right)^{\gamma_1}, \quad (2.96a)$$

$$N^{\text{ref}} = N_{300}^{\text{ref}} \left(\frac{T_L}{300}\right)^{\gamma_2}, \quad (2.96b)$$

$$\alpha^I = \alpha_{300}^I \left(\frac{T_L}{300}\right)^{\gamma_3}. \quad (2.96c)$$

This procedure is followed for instance by Sotoodeh [40] for several III-V binary and ternary compounds, obtaining relations for low-mobility in GaAs, which are used as a reference in this work. In this case $\gamma_1 = \gamma_3 = 0$ so μ^{\min} nor α^I are temperature dependent, the rest of the parameters are presented in Table 2.5.

Table 2.5: GaAs parameters for low field mobility calculation [40].

Carrier	$\mu_{300}^{\min} [cm^2/Vs]$	$N_{300}^{\text{ref}} [cm^{-3}]$	α_{300}^I	γ_2
n	500	$6 \cdot 10^{16}$	0.394	3
p	20	$1.48 \cdot 10^{17}$	0.38	3

Figure 2.12 shows the variation of electron mobility as a function of doping concentration for GaAs according to Eq.(2.95), using the parameters given in [40]. It can be clearly noted how higher doping concentrations make the mobility value less sensitive to temperature.

A very similar approach is used by Arora *et al.* [39] for the calculation of carrier mobility in Silicon as a function of doping and temperature, the slight difference with Eq.(2.95) is the use of a temperature dependent mobility μ_0 instead of $(\mu^L - \mu^{\min})$. The factor γ_0 will be used as the exponent for this temperature dependence following the same shape as in Eq.(2.96). This relation is given by

$$\mu^{LI} = \mu^{\min} + \frac{\mu_0}{1 + \left(\frac{C}{N^{\text{ref}}}\right)^{\alpha^I}}, \quad (2.97)$$

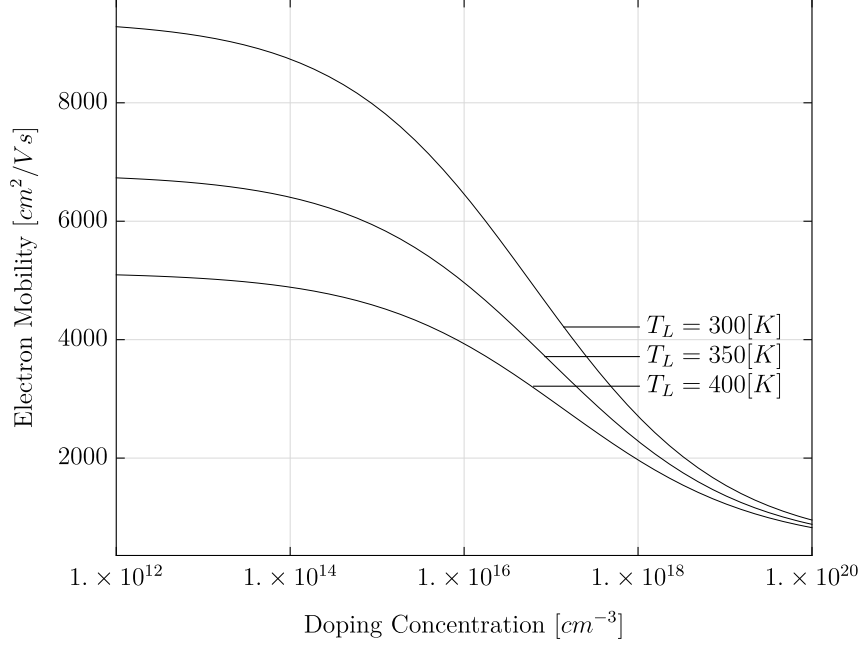


Figure 2.12: Electron mobility in GaAs for various temperatures using the empirical relation (2.95).

and its parameters are presented in Table 2.6.

Table 2.6: Si parameters for low field mobility calculation.

Carrier	$\mu_{0,300} [cm^2/Vs]$	$\mu_{300}^{\min} [cm^2/Vs]$	$N_{300}^{\text{ref}} [cm^{-3}]$	α_{300}^I	γ_0	γ_1	γ_2	γ_3
n	1268	92	$1.3 \cdot 10^{17}$	0.91	-2.33	-0.57	2.4	-0.146
p	406.9	54.3	$2.35 \cdot 10^{17}$	0.88	-2.23	-0.57	2.4	-0.146

Given that empirical models are fitted from experimental data it is usual to find considerable variation between parameters following different references.

If low-field mobility is considered, then τ_m can be easily calculated using Eq.(2.81). There are several works which develop empirical relations that take into account minority or majority carrier mobility as well as compensation due to having two types of dopant. However, since all the modeling in this work is done in highly doped non-compensated materials, only the minority mobility expressions are considered.

In many cases there are additional factors that further reduce the mobility under low field conditions. Regardless if any other factors are considered, low field mobility will be expressed as μ^{LF} .

2.3.3 High Energy Mobilities

Velocity Saturation

At low energies, non-polar semiconductors interact with the *acoustic* and *optical deformation potential* (ADP and OPD respectively), which cause the temperature dependent lattice scattering, and the doping dependent impurity scattering mechanisms. On the other hand, under low energy conditions, polar semiconductors such as GaAs, interact with polar acoustic phonons (piezoelectric scattering) and absorb polar optical phonons (POP). With an increase in the parallel component of the applied field, carriers can gain energies above the optical phonon energy threshold, which for a phonon frequency of ω_{OP} corresponds to $\hbar\omega_{OP}$, and are able to transfer the energy gained from the field to the lattice by optical phonon emission. This effect leads to a saturation of the carriers velocity, and a consequent reduction in mobility. The effect is similar to a body moving in a viscous fluid and reaching a limit velocity. In the case of charge carriers in semiconductors it is called the *saturation velocity*, v_{sat} .

The value of v_{sat} is often obtained from empirical relations. The relation used in this work was developed by Quay *et al.* [43], and depends exclusively on lattice temperature. The effect of doping density is rarely included for v_{sat} and has a minor effect in the final value. Temperature dependence of v_{sat} is given by

$$v_{\text{sat}} = \frac{v_{300}^{\text{sat}}}{1 - A + A \left(\frac{T_L}{300} \right)}, \quad (2.98)$$

where A is a factor that depends on the material and type of carrier. The parameters for the calculation of v_{sat} are presented in Table 2.7.

Table 2.7: Parameters for the calculation of saturation velocity [43].

Material	Carrier	v_{300}^{sat} [m/s]	A
Silicon	n	$1 \cdot 10^5$	0.26
	p	$0.704 \cdot 10^5$	0.63
GaAs	n	$0.72 \cdot 10^5$	0.56
	p	$0.63 \cdot 10^5$	0.41

Considering Eq.(2.92), as the electric field is increased, mobility reduces asymptotically to zero. Electric fields high enough for this effect to be important can be readily attained in small devices with high doping concentrations. This degradation of mobility at high energies should be taken into account for the modeling under high-fields and hot-carrier effects. In this sense, the most common approach is to consider mobility dependence of electric field. Besides obtaining an empirical fit for doping dependence, Caughey & Thomas [42] developed expressions for electric field dependence for carrier mobilities on Silicon. This commonly used

expression is given by

$$\mu^{HF} = \frac{\mu^{LF}}{\left(1 + (\mu^{LF} E / v_{\text{sat}})^{\beta_C}\right)^{1/\beta_C}}. \quad (2.99)$$

For simplicity, the values for the coefficient β_C were taken as integrals in the mentioned work. Canali *et al.* [44] later obtained more precise parameters and expressions for field and temperature dependence of the drift velocity, which is why this is often referred to as the Canali model. Even though these phenomenological descriptions have a very good fit with experimental data, the energy of carriers does not depend exclusively on the electric field when modeling a device using a hydrodynamic model. Because of this, different models are needed, which describe the variation of transport parameters, specifically momentum and energy relaxation times τ_m and τ_ϵ , with carrier temperature. The first to deliver such a model were Baccarani & Wordeman [11] in order to study velocity overshoot in Silicon. In their work, they used a basic model for effective momentum relaxation time dependent on carrier temperature, defined here as T_c , according to

$$\tau_m^{HF} = \tau_m^{LF} \left(\frac{T_c}{T_L}\right)^{\gamma_F}. \quad (2.100)$$

In most cases $\gamma_F = -1$ and the low field momentum relaxation time τ_m^{LF} is obtained from the low-field mobility

$$\tau_m^{LF} = \frac{m^* \mu^{LF}}{e}. \quad (2.101)$$

Consequently, according to this model Eq.(2.100), high field mobility is obtained as

$$\mu^{HF} = \mu^{LF} \left(\frac{T_c}{T_L}\right)^{\gamma_F}. \quad (2.102)$$

It must be noted that this model considers effective mass to be constant for high energy particles (depends only on lattice temperature). As it is discussed below, this is not always accurate. Considering electrons in a semiconductor under an applied electric field, where no spatial nor temporal gradients are present, the energy balance consisting of equations (2.65) and (2.74) leads to

$$\frac{e n u_n^2}{\mu_n} = \frac{(\xi_n - \xi_0)}{\tau_\epsilon}, \quad (2.103)$$

where Eq. (2.92) was used for drift velocity, given that no carrier density gradients are considered. This expression shows that not only changes in mobility due to increasing collisions make velocity saturate, but also changes in the energy transfer rate into the lattice (thermalization). This relation between carrier energy, velocity and the applied electric field, along with the expression given by Caughey & Thomas, Eq. (2.99) using $\beta_C = 2$, allows to obtain a simple expression for energy relaxation time, given by

$$\tau_\epsilon^{\text{bw}} = \frac{\tau_m^{HF}}{2} + \frac{3k_B \mu^{LF}}{2e v_{\text{sat}}^2} \frac{T_L T_c}{T_L + T_c}, \quad (2.104)$$

where the superscript ‘bw’ is used to highlight the fact that this is obtained through the model of Baccarani & Wordeman, and τ_m^{HF} is given by Eq.(2.100). This expression is valid for both electrons and holes. This approach is used for instance by Jüngel[45], where a Si diode is simulated and high energy effects such as velocity overshoot can be observed.

Another often used high field mobility model that depends on carrier temperature, is the one developed by Hänsch *et al.* [46]. This model also depicts the behavior of semiconductors that reach asymptotically a maximum velocity v_{sat} . As observed in Fig. 2.11, electrons and holes for Si, and holes for GaAs show this behavior. The main assumptions of this model are a linear expression for the distribution function and constant energy relaxation time, which deliver a self-consistent expression for mobility. The dependence with carrier temperature according to the cited study is given by

$$\mu^{HF} = \frac{\mu^{LF}}{1 + \alpha^F (T_c - T_L)}, \quad (2.105)$$

with the factor α^F being

$$\alpha^F = \frac{3k_B\mu^{LF}}{2e\tau_\epsilon v_{\text{sat}}^2}. \quad (2.106)$$

Since the energy relaxation time defines the rate at which energy is transferred from and to the lattice from the charge carriers, it is reasonable to expect that this parameter should depend on the mean energy of both the lattice and carriers. However, for this model it is assumed to be constant. Additionally, it is very complicated to obtain this parameter experimentally. To overcome this problem, Gonzalez *et al.* [47] presented a Monte Carlo solution based method for several materials under different conditions and developed an empirical expression depending on lattice and carrier temperatures. This fitting is given by

$$\tau_{\epsilon,n}^{\text{mc}} = \tau_{\epsilon,0} + \tau_{\epsilon,1} \exp \left(C_1 \left(\frac{T_n}{300} + C_0 \right)^2 + C_2 \left(\frac{T_n}{300} + C_0 \right) + C_3 \left(\frac{T_L}{300} \right) \right), \quad (2.107)$$

for electrons, where the superscript ‘mc’ is used to emphasize the use of the Monte Carlo method. A constant value is used for holes. Parameters used for this expression are presented in Table 2.8 for Si and GaAs. Nevertheless, the use of this fitting along with the Hänsch mobility model is inconsistent due to the basic assumptions of the latter, mentioned above.

Table 2.8: Parameters for the calculation of energy relaxation times as a function of temperature.

Material	$\tau_{\epsilon,0}$ [ps]	$\tau_{\epsilon,1}$ [ps]	C_0	C_1	C_2	C_3	$\tau_{\epsilon,p}$ [ps]
Silicon	1.0	-0.538	0	0.0015	-0.09	0.17	0.4
GaAs	0.48	0.025	0	-0.053	0.853	0.5	1.0

As can be deduced from the Eqs.(2.102) and (2.105), both the basic and Hänsch models deliver the degrading behavior of mobility as energy is increased. The main difference between both of them is the assumption regarding energy relaxation time. This implies there will be a

difference in the transport parameters with respect to temperature. Therefore, even though both models should deliver similar results in a situation like the one described to obtain Eq. (2.103), greater difference could arise in the simulation of a more complex device. A brief comparison between the two models is presented in the results section.

Transferred Electron Effect

Once more referring to Fig.2.11 it can be noted that electrons in GaAs show a decrease in drift velocity as the electric field increases, this means a negative differential mobility, which arises from a phenomenon called *transferred electron effect* (TEE). While the decrease in mobility described above can be related to lower momentum relaxation times due to optical phonon emission, the further reduction in mobility in GaAs and some other compound semiconductors occurs due to a change in the effective mass of electrons overcoming a specific energy level. As can be seen in the band diagram of GaAs in Fig.2.7, the valley at the L point is energetically located near to that of Γ , this means that when electrons have high energies they can easily be transferred from one band to another, and since L -band will have many available states, the total change of average effective mass is not negligible. In fact, the effective mass at the L -band is much higher than that at Γ , thus the average effective mass is increased and consequently the mobility is reduced. This effect occurs in some III-V materials with satellite bands near enough to the central band.

The most commonly used relation in order to represent this behavior is an empirical expression for drift velocity versus electric field, known as the transferred electron model [48]. This is given by

$$u_{n,\text{drift}}(E) = \frac{\mu_n^{LF} E + v_{\text{sat}} (E/E_T)^{\beta_T}}{1 + (E/E_T)^{\beta_T}}, \quad (2.108)$$

which is fitted to experimental or Monte-Carlo data through the parameters E_T and β_T . Commonly used values for these parameters in GaAs are [49, 50]

$$E_T = 4 \text{ kV/cm}, \quad (2.109)$$

$$\beta_T = 4. \quad (2.110)$$

Expressions for doping dependence for the reference field E_T have also been developed using the Monte Carlo method [51], given by

$$E_T(N) = F_0 + F_1 \left(\frac{N}{N_F} \right)^{\beta_F}, \quad (2.111)$$

with the fitting parameters for GaAs listed in Table 2.9.

An important study using the Monte Carlo approach was also performed by Tait & Krowne [52], where they presented the equivalent transport properties calculated by this method including total effective mass, along with momentum and energy relaxation times. They also presented the resulting properties such as electron velocity and temperature, for the case of a

Table 2.9: Parameters for the calculation of E_T as a function of doping density [51].

Parameter	Value
F_0 [kV/cm]	2.735
F_1 [kV/cm]	0.752
N_F [cm ⁻³]	$2.14 \cdot 10^{16}$
β_F	0.203

spatially homogeneous electric field on an n -doped GaAs sample. Figure 2.13, presents the results for electron drift velocity using the transferred electron model with the parameters from both of the aforementioned references, along with the Monte Carlo results of Tait & Krowne.

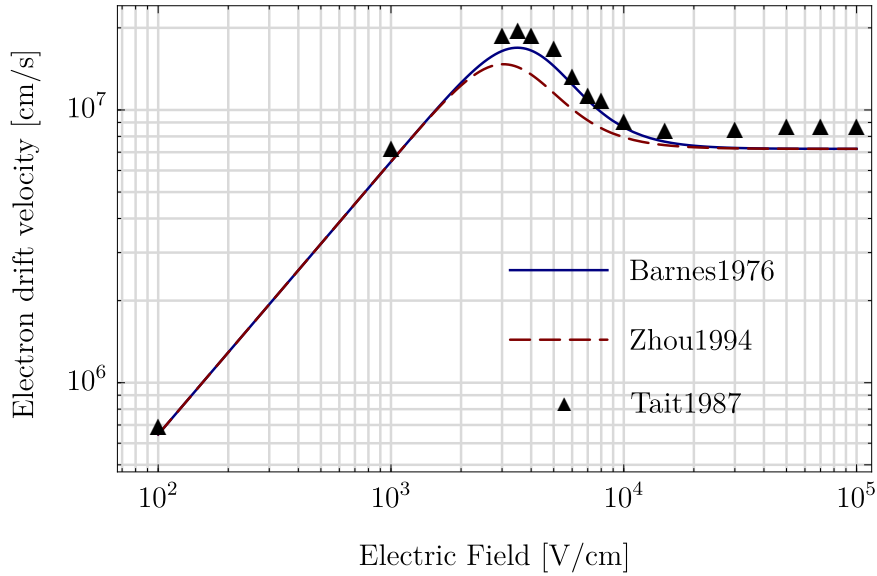


Figure 2.13: Electron velocity in n -doped GaAs with $N_D = 10^{16}$ cm⁻³, as a function of electric field using the transferred electron model and Monte Carlo results.

A temperature dependent multi-valley mobility model can also be used in order to quantify this effect. In order to do this, the population ratio P_L is defined as [23],

$$P_L = \frac{n_L}{n_\Gamma} = 4 \left(\frac{m_L}{m_\Gamma} \right)^{3/2} \exp \left(-\frac{E_{C,L} - E_{C,\Gamma}}{k_B T_n} \right), \quad (2.112)$$

where n_L and n_Γ are the electron populations in the L and Γ valleys respectively, hence

$$n = n_L + n_\Gamma. \quad (2.113)$$

The pre-factor 4 arises from the fact that there are four times more equivalent upper valleys

in the L -direction than lower valleys in the Γ -direction. The use of Boltzmann distribution in order to obtain the population ratio has been criticized because the electrons are not in thermal equilibrium, neither internally nor with the phonons [34]. However, since the present work focuses on the modeling of solar cells, the carrier population will be much higher than most of other devices, therefore internal equilibrium is easier to achieve.

The energy gap at each point is lattice temperature dependent and calculated empirically from Eq.(2.13), considering that

$$E_{g,L} - E_{g,\Gamma} = E_{C,L} - E_{C,\Gamma}. \quad (2.114)$$

If the change in current density due to transferred electron effect is isolated from other phenomena (for instance, diffusion current), the total value of the current is equivalent to the sum of L and Γ valley electrons contribution, each with a low field mobility given by μ_L^{LF} and μ_Γ^{LF} respectively. The latter is expressed as

$$\mathbf{J}_n = en\mu^{HF} \mathbf{E} = e \left(n_L \mu_L^{LF} + n_\Gamma \mu_\Gamma^{LF} \right) \mathbf{E}, \quad (2.115)$$

and the high field mobility is obtained as an energy dependent shift from μ_Γ^{LF} to μ_L^{LF} . Combining Eqs.(2.113), (2.115) and (2.112), we get

$$\mu^{HF} = \frac{\mu_\Gamma^{LF} + P_L \mu_L^{LF}}{1 + P_L}, \quad (2.116)$$

where the energy dependency is established as a function of electron temperature in the expression for P_L , given in Eq.(2.112). As a consequence of electrons moving from one band to another, the total average effective mass also changes from that at the Γ -valley to the one at the L -valley according to

$$m_n^{HF} = \frac{m_\Gamma + P_L m_L}{1 + P_L}. \quad (2.117)$$

It is noted that the mass of each specific electron is strictly m_Γ or m_L , and m_n^{HF} is the total average value. From Eq.(2.19) it can be deduced that $m_L(300 \text{ K}) = 0.47m_0$, which compared to $m_\Gamma(300 \text{ K}) = 0.067m_0$ is an order of magnitude higher, meaning the change is significant. The temperature dependency is given by Eq.(2.21). Using the above expressions the change of average momentum relaxation time can also be obtained from Eq.(2.81). In order to select the model that better describes the behavior of transport parameters under high energy conditions, an analysis of different assumptions is made in Chapter 4.

2.4 Interband Scattering Processes

2.4.1 Generation

Photogeneration

Even before the discovery of the photoelectric effect in 1839, a relation between light's frequency and its contained energy was accepted, although light was thought of only as a wave.

Max Planck quantified this relation in 1900 [53], proposing the existence of *quanta* of energy composing light. Einstein later related these packets with what would later be called photons, proposing the dual nature of light. This originated the Planck-Einstein relation, Eq.(2.15), which for light can be written as

$$E_{ph}(\lambda) = \frac{hc}{\lambda}. \quad (2.118)$$

This means high-energy light will have a high frequency and therefore a short wavelength, while on the contrary lower-energy light will have larger wavelength. On the visible range of light, blue lights are more energetic while red lights have lower energies. A very appropriate and commonly used unit for the order of magnitude of light's energy and semiconductor bandgaps is the electron-volt, eV, which delivers the simplified relation

$$E_{ph}(eV) = \frac{1.24}{\lambda(\mu m)}. \quad (2.119)$$

This relation is essential for the study of solar light conversion given that it allows to accurately approximate the number of electron-hole pairs being created through the solar cell as light penetrates. The major input for the operation of solar cells is the incident light intensity for a given wavelength. With this, the Planck-Einstein relation can be used to know the photon flux per wavelength using

$$H(\lambda) = \Phi(\lambda) E_{ph}(\lambda) = \Phi(\lambda) \frac{hc}{\lambda}, \quad (2.120)$$

where $H(\lambda)$ is the light intensity per unit of area for a given wavelength (for instance in W/m^2). In this context, information of incoming solar light per wavelength is needed. At the average distance from the sun, the total radiation received by the Earth outside the atmosphere is $1353 W/m^2$. This is the sum of the intensity for each wavelength, while the distribution of the spectral irradiance is given roughly by Planck's radiation law for a black body at approximately 5800 K, shown by the dashed line in Fig.2.14. This is a rather good approximation in space, but at the earth's surface the incoming light is attenuated by the atmosphere. The amount of dissipation depends on how much air light has to go through. This means that the angle at which light is reaching the surface strongly affects $H(\lambda)$, this effect is quantified by the concept of *air mass*.

The air mass (AM) is defined as the secant of the sun's angle and the zenith, usually defined as

θ . Therefore, it is a measure of the sun's path relative to the shortest path that it can undergo to reach the surface (sun at the zenith). In this manner, AM0 is the irradiance spectre outside the earth atmosphere; AM1 is the spectrum with the sun at its zenith ($\theta = 0^\circ$), equivalent to 925 W/m^2 of power; AM2 is the spectrum for $\theta = 60^\circ$ with an incident power of 691 W/m^2 and so on. The international standard used as a reference for evaluating spectrally selective PV applications is the AM1.5 spectre, this is defined for $\theta = 48.19^\circ$ under specific atmospheric conditions defined at [54]. This spectrum is shown in Fig.2.14 along with AM0.

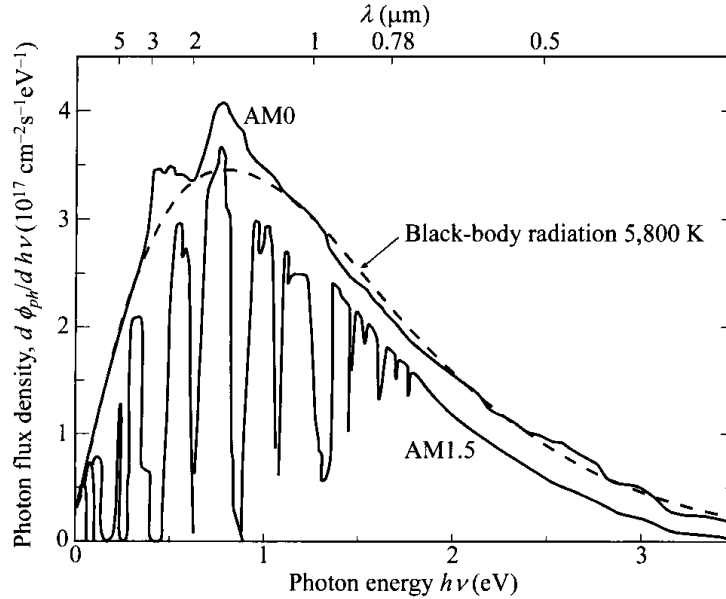


Figure 2.14: Solar spectrum in photon flux density for AM0 and AM1.5 [23].

The fact that each semiconductor material has a very specific energy gap is very relevant for photonic devices because it implies that there is a wavelength associated to that energy. Specifically for solar cells, the choice of the best material is closely related to this property.

Photons with an energy equal or above E_g will be able to move an electron from the valence to the conduction band and therefore generate an electron-hole pair, while if $E_{ph} < E_g$ the energy of the photons will only contribute to heat the lattice. Moreover, when $E_{ph} > E_g$ *hot carriers* are generated which later relax to the bottom of the conduction band (or top of valence band), giving away their energy as heat. This phenomenon is known as *thermalisation*. Whichever the case, any photon with an energy that does not match exactly that of the semiconductor gap, will mean a waste of energy and the generation will only be one electron-hole pair per photon with an energy above E_g , for regular solar cells. There are three means of avoiding this inefficiencies that are currently being studied, upconversion (two or more low energy photons generating one electron-hole pair), downconversion (one high energy photon generating more than one electron-hole pair) or hot carrier extraction. The later is studied in this work.

Since light of different energies has different wavelengths, it will interact differently with the semiconductor lattice. In general terms, higher-energy photons will be absorbed easier than the ones with lower energies. This is represented through the absorption coefficient denoted

here by α_c , which determines how far into a material light of a particular wavelength can penetrate before it is absorbed. It is usually measured in cm^{-1} . Figure 2.15 shows this coefficient for several semiconductor materials; this data was tabulated by the Department of Electrical & Computer Engineering of the Brigham Young University and can be found in [55], which is the reference used in this work. More specific research on optical absorption on GaAs has been performed for energies between 0.6 and 2.75 eV by Sturge [56], for different doping concentrations by Casey *et al.* [57] and for infrared spectrum by Spitzer and Whelan [58].

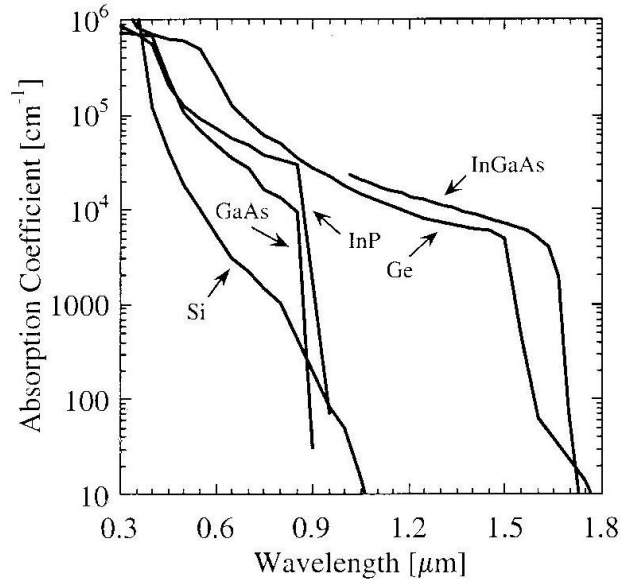


Figure 2.15: Optical absorption coefficient for different semiconductor materials [59].

Optical properties of semiconductors make it important to take special care of material thickness when designing a solar cell. On one hand, a minimum thickness is needed in order to capture a considerable part of the incoming light which will be different for each material and also depending on the wavelength of the incoming light. This would imply the thicker the absorber layer the better, but in reality carriers traveling through the material recombine when an electron meets a hole (process explained in section 2.4.2), so thinner layers are needed to minimize the amount of carriers being recombined. This means there is a trade-off between more light being captured and carriers being recombined, giving rise to an optimal solar cell thickness. A very useful technique for reducing the losses by recombination is to use light trapping techniques allowing for thinner solar cells. For more information regarding light managing, one can refer to chapter 9 in [31]. Therefore it is important to consider spatially variable generation when analyzing a solar cell.

Finally, part of the light reaching the surface of the solar cell is reflected at the surface by a factor denoted here as $R_c(\lambda)$, which is also wavelength dependent. This means $1 - R_c(\lambda)$ of the light penetrates into the lattice at each frequency. Concluding, in the case of one electron-hole pair being generated per photon, the generation rate for a specific wavelength

$g(\lambda, x)$ decays exponentially in space according to α_c , hence

$$g(\lambda, x) = \alpha_c(\lambda) \Phi(\lambda) [1 - R_c(\lambda)] \exp(-\alpha_c(\lambda)x). \quad (2.121)$$

The total depth-dependent generation rate $G(x)$ is

$$G(x) = \int_0^{\lambda_g} g(\lambda, x) d\lambda, \quad (2.122)$$

where the upper limit of integration is defined by the wavelength corresponding to the energy gap of the material.

Impact Ionization

Impact ionization (II) is a phenomenon that occurs in situations where the energy of carriers is high. If a conduction electron impacts a bonded valence electron, this electron is displaced into the conduction band. Therefore, an electron hole pair is generated while the first electron still has enough energy to be maintained in the conduction band, resulting in three free carriers from one. The same process can take place starting from a high energy hole, resulting in two holes and a conduction electron. This is the opposite to Auger recombination, described in Section 2.4.2.

From the point of view of solar cells, high-energy carriers that originate the process can come from a photon with an energy higher than twice the bandgap. This implies that one photon generates more than one electron hole-pair, which is the principle of Impact Ionization Solar Cells (IISC) that can attain quantum efficiencies greater than one similarly to hot carrier solar cells (HCSC).

In this process energy is conserved but particle number is not, so one has to be careful when expressing the corresponding balance equations. There are different ways of quantifying the effect of impact ionization depending on the model. For the DD model, field dependent ionization coefficients are used, while hydrodynamic models allow for the use of a relation depending on carrier temperature. A study presenting a method for simulating II in a PN junction using a HD model was carried out by Quate *et al.* [13], comparing normally used ionization coefficients with the results of their study. Yet a simpler approach for quantifying II has been used in [60] for simulating high electron mobility transistors (HEMTs). This is given by

$$G_n^{II}(T_n, T_L, n) = n A_{II} \exp\left(\frac{-B_{II} E_g}{k_B T_n}\right), \quad (2.123a)$$

$$G_p^{II}(T_p, T_L, p) = p A_{II} \exp\left(\frac{-B_{II} E_g}{k_B T_p}\right), \quad (2.123b)$$

for electrons and holes, respectively. A_{II} and B_{II} are constants and presented in Table 2.10 for III-V materials.

Table 2.10: Impact ionization modeling constants for III-V materials.

Parameter	Value
$A_{II} [s^{-1}]$	10^{13}
B_{II}	1.0

2.4.2 Recombination

Carrier recombination is the opposite process to generation. Therefore, it is the loss of an electron or hole through the decay of an electron from the conduction to the valence band. There are several ways this phenomenon can occur and, depending on the specific mechanism, the energy can be released as a photon, heat as phonon emission or given up as kinetic energy to other carrier. This is a process that occurs naturally when the crystalline lattice is at a finite temperature where, in absence of an external stimulus, thermal recombination balances with thermal generation. Therefore, the recombination mechanisms described here do not include thermal recombination rate.

Recombination processes are usually divided in radiative and non-radiative, and their relative importance depends on the type of semiconductor (direct or indirect bandgap) and the specific device being studied. The difference between them is whether they emit a photon as a consequence of the energy decay or dissipate into other types of energy. The directly inverse process to photo-generation is called *band to band*, *direct* or simply *radiative recombination*; this mechanism is portrayed in the left of Fig.2.16. In the middle of the same figure, the most important recombination mechanism for solar cells is shown. It occurs through intermediate energy states called *trap states* and recombines one electron with one hole. The last of the mechanisms presented in this section is named Auger recombination and is also non-radiative. This mechanism involves three particles.

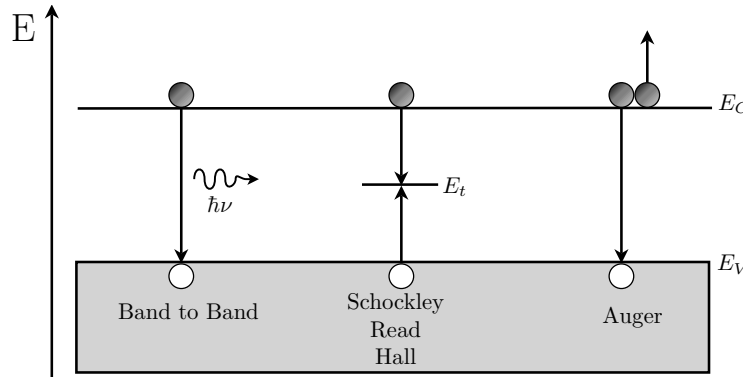


Figure 2.16: Schematic representation of different recombination mechanisms.

Both band to band and Auger recombination mechanisms are also referred to as unavoidable processes given that they depend directly on properties of the intrinsic material, while SRH is designated as an avoidable process because it is provoked by imperfections in the material. The total recombination rate R , will be the addition of all these mechanisms, *i.e.*

$$R = R_{rad} + R_{Aug} + R_{SRH}. \quad (2.124)$$

Radiative Recombination

Radiative, or spontaneous recombination, is more important for direct bandgap semiconductors (*e.g.* GaAs), but not so important for indirect semiconductors. This is desired for some devices like LEDs but not in solar cells, where it reduces the attainable carrier current. This type of recombination depends directly on the absorption coefficient of the material, but a simplified expression is often used with a material-dependent parameter, B_{rad} in this case. The simplified expression for radiative recombination is

$$R_{\text{rad}} = B_{\text{rad}} (np - n_i^2). \quad (2.125)$$

When studying a heavily doped semiconductor, minority carrier concentration is dominant and the expression for radiative recombination can be further reduced to

$$R_{\text{rad}} \approx \frac{n - n_0}{\tau_{n,\text{rad}}}, \quad (2.126)$$

for a p -type semiconductor, where

$$\tau_{n,\text{rad}} = \frac{1}{B_{\text{rad}} N_A}. \quad (2.127)$$

Similarly,

$$R_{\text{rad}} \approx \frac{p - p_0}{\tau_{p,\text{rad}}}, \quad (2.128)$$

if an n -type semiconductor is considered, where

$$\tau_{p,\text{rad}} = \frac{1}{B_{\text{rad}} N_D}. \quad (2.129)$$

Minority carrier concentrations at equilibrium for electrons and holes are approximated by Eqs.(2.41b) and (2.40b) respectively. Hence, in this case

$$p_0 = n_i^2 / N_A, \quad (2.130a)$$

$$n_0 = n_i^2 / N_D. \quad (2.130b)$$

Radiative recombination is not important for practical solar cells at the operating point, but in the limit of perfect material it is the mechanism which limits efficiency [31].

Auger Recombination

Auger recombination is a three particle process that consists of the collision between two similar free carriers resulting in the excitation of one of them into a higher level of kinetic energy and the recombination of the second with a hole (or electron depending on the case). In other words, the energy released from the recombination is transferred as kinetic energy

to a third carrier, which later thermalizes and converts this energy into heat. Each process is proportional to the densities of the three carriers involved. Therefore, for two electron collisions,

$$R_{\text{Aug},n} = A_p (n^2 p - n_0^2 p_0), \quad (2.131)$$

and for two holes collisions,

$$R_{\text{Aug},p} = A_n (np^2 - n_0 p_0^2). \quad (2.132)$$

Using the equilibrium relations described in subsection 2.1.4, total Auger recombination can be expressed as

$$R_{\text{Aug}} = (A_n n + A_p p) (np - n_i^2). \quad (2.133)$$

This mechanism is considerable when carrier densities are high. For instance for heavily doped materials or high-level injection, *e.g.* concentrated light. These are conditions where non thermal equilibrium could also be important to take into account. For high doping levels similar relations to Eqs.(2.126) and (2.128) are obtained, allowing to express carrier lifetimes as

$$\tau_{n,\text{Aug}} = \frac{1}{A_n N_A^2}, \quad (2.134a)$$

$$\tau_{p,\text{Aug}} = \frac{1}{A_p N_D^2}, \quad (2.134b)$$

for electrons and holes respectively.

Shockley-Read-Hall

Despite being a mechanism that does not occur in an ideal semiconductor, Shockley-Read-Hall (SRH) or recombination via trap states, is the most important recombination process in real semiconductors. This process occurs through energy levels located between valence and conduction bands, which momentarily capture a free carrier. This carrier can then be released again by thermal activation or recombined if a carrier of the opposite polarity is captured, leaving the trap empty again. Some of these localized states are close to one band edge, so they only capture one type of carrier temporarily and then release it again, given that the energetic distance with the other band edge does not allow them to capture a carrier of different polarity. These localized states are usually referred to as *traps*, while the ones able to capture both types of carriers are called *recombination centers*. Intuitively this means SRH recombination will be maximum when the traps are located at the middle of the band gap.

An expression for SRH recombination can be found through equilibrium statistics for steady-state conditions. This relation depends on the recombination center density N_T , and the energy level at which these are located E_T , which will determine electron and hole density at

the trap level n_T and p_T respectively. Thus, the expression for SRH recombination is [30],

$$R_{\text{SRH}} = \frac{np - n_i^2}{\tau_{n,\text{SRH}}(p + p_T) + \tau_{p,\text{SRH}}(n + n_T)}. \quad (2.135)$$

If E_T is known, carrier density at the traps can be found by

$$n_T = N_C(T_L) \exp\left(\frac{-E_C + E_T}{k_B T_L}\right), \quad (2.136a)$$

$$p_T = N_V(T_L) \exp\left(\frac{-E_T + E_V}{k_B T_L}\right), \quad (2.136b)$$

for electrons and holes, respectively. Carrier effective densities of states N_C and N_V are obtained from Eq.(2.27). Temperature dependency of carrier lifetime values $\tau_{n,\text{SRH}}$ and $\tau_{p,\text{SRH}}$, is modeled as

$$\tau_{n(p),\text{SRH}}(T_L) = \left(\frac{300[\text{K}]}{T_L}\right)^{3/2} \tau_{n(p),\text{SRH}}^{300}, \quad (2.137)$$

where T_L is measured in [K] and $\tau_{n(p),\text{SRH}}^{300}$ is the reference lifetime,

$$\tau_{n(p),\text{SRH}}^{300} = \frac{1}{\sigma_{T,n(p)} N_T v_{th,n(p)}^{300}}, \quad (2.138)$$

being $\sigma_{T,n(p)}$ the capture cross section of the traps and v_{th} the thermal velocity given by

$$v_{th} = \sqrt{\frac{3k_B T_L}{m^*}}, \quad (2.139)$$

for any carrier with an effective mass m^* .

SRH recombination also reduces to an expression analogous to Eq.(2.126) for a p -type semiconductor and Eq.(2.128) for n -type materials, which depends only on the recombination lifetime and excess of minority carriers. Therefore, using Eq.(2.124) a total carrier lifetime can be obtained depending on each recombination mechanism. This is

$$\frac{1}{\tau_{n(p)}} = \frac{1}{\tau_{n(p),\text{SRH}}} + \frac{1}{\tau_{n(p),\text{Aug}}} + \frac{1}{\tau_{n(p),\text{rad}}}, \quad (2.140)$$

which is the value usually found in references given that the simplification for doped materials is being considered and the total recombination rate R , calculated as

$$R \approx \frac{n - n_0}{\tau_n}, \quad (2.141a)$$

$$R \approx \frac{p - p_0}{\tau_p}, \quad (2.141b)$$

for a p -type and n -type material, respectively.

Surface Recombination

Surface recombination can be considered as a special case of trap assisted recombination, given that occurs in surfaces (or interfaces) where additional energy states are available due to material imperfections. This is specially important on the surface of the material because of dangling bonds, making the surface a region filled with recombination centers of different energy levels. The higher rate of recombination near the surface is interpreted as a *leakage* of current, particularly of minority carriers. This current is related to the *surface recombination velocity* S_n or S_p [31]. In steady state conditions, it can be found that

$$J_n(x_s) = -eS_n(n_s - n_0), \quad (2.142)$$

which is the amount of current escaping the device due to minority carrier recombination. Here, $J_n(x_s)$ and n_s are the electron current and density evaluated at the surface, x_s . In an ideal case this value is zero, given that the recombination velocity at the surface would be zero; a positive value would mean an external injection of carriers at the surface. Similarly for holes

$$J_p(x_s) = eS_p(p_s - p_0), \quad (2.143)$$

with $J_p(x_s)$ and p_s the hole current and densities evaluated at the surface. From Eq.(2.59), we note that Eqs.(2.142) and (2.143) allow to obtain expressions for minority carrier boundary conditions relating carrier density and velocity. For instance, for a non-degenerate PN junction, the value for majority carrier density at the boundaries will be that of the doping density and the value for minority carrier can be obtained with these expressions depending on the model used for approximating the current.

Surface recombination was an important problem in the first models of GaAs solar cells, where a major decay in the current was observed with respect to what was theoretically expected. Later on, this issue was solved using surface passivation techniques that tie dangling bonds reducing the amount of available recombination centers. Recombination of minority carriers near the surface is also reduced by the addition of a doped layer, which produces an electric field and repels the carriers. This layer is often referred to as the *back surface field*, BSF. Because of these techniques, surface recombination is a minor problem in current solar cells. Already in the mid 80's this problem was solved, for instance in [10] the values of S_n and S_p are small. These are used as reference parameters and listed in the following subsection.

Recombination Parameters for GaAs

The necessary parameters to calculate recombination values are presented ahead in Table 2.11. Most of them are taken from a Handbook of Semiconductor Parameters [26] and the specific ones that could not be found there were obtained from the work done by Palankovski [29].

Table 2.11: Recombination parameters for GaAs [26, 29].

Carrier	$B_{\text{rad}} [cm^3/s]$	$A_{n,p} [cm^6/s]$	$E_T [eV]$	$\sigma_T [m^2]$	$N_T [cm^{-3}]$	$S_{n,p} [cm/s]$
Electron(n)	10^{-10}	$5 \cdot 10^{-30}$	0.4	10^{-14}	$2 \cdot 10^{16}$	10^3
Hole(p)		$3 \cdot 10^{-30}$		10^{-13}		10^4

2.5 Analytical Solution for a PN Junction Solar Cell

PN junctions are a way of achieving the effect of selective contacts for electronic devices and the functional component of a solar cell. The doping level of the material is controlled achieving a potential drop that acts as a selective potential barrier for carriers. There are numerous methods for coupling layers of doped semiconductors depending on the requirements of the device, being even possible to use different materials (heterojunctions). The type of junction analyzed ahead is a PN homojunction.

In simple terms, a PN junction is established when a p -type semiconductor is physically assembled to an n -type material. Since carriers of opposite polarity are near by, there is carrier diffusion in the junction in order to reach equilibrium. Such flow leaves an area near the junction depleted of carriers, hence the name *depleted region*, and establishes the potential drop defined as the *built in potential* V_{bi} . Since the amount of carriers that diffuse to each side depends on the charge difference, V_{bi} is strongly dependent on doping density. At equilibrium conditions, we get

$$V_{\text{bi}} = \frac{k_B T_L}{e} \ln \left(\frac{N_D N_A}{n_i^2} \right). \quad (2.144)$$

This expression comes from Eq.(2.90) considering zero current flowing through the device, therefore thermal equilibrium is assumed. Any external applied voltage V_{app} shifts the potential level on one side respect to the other and the potential drop across the junction becomes

$$V = V_{\text{bi}} - V_{\text{app}}, \quad (2.145)$$

meaning that a negative applied bias extracts even more carriers to balance charges and, therefore, the depletion region width is increased. The opposite is true for a positive bias.

2.5.1 Depletion Region Approximation

The simplest way to obtain an approximation of carrier densities across the device is through the depletion region approximation (DRA). This approach consists of two main assumptions. First, it is assumed that a finite region near the junction contains no free carriers, hence the name depleted region; also called the space charged region (SCR). This implies that there is a constant net charge at the surrounding area near the junction, within the SCR. Therefore, the potential drop equivalent to the built-in voltage, takes place entirely in this region. Since

the length of this zone depends mainly on the doping densities and material properties, the total length of each side must be larger than its respective depleted region for the following analysis to be valid. The zones outside the space charged region are called the neutral regions, implying that they have constant potential, zero electric field and the majority carrier value is equivalent to the doping density. Consequently, the amount of current flowing through the device is determined by minority carrier density variations. Figure 2.17 presents a representation of each zone together with the electric potential V , field E , and total charge Q across the junction.

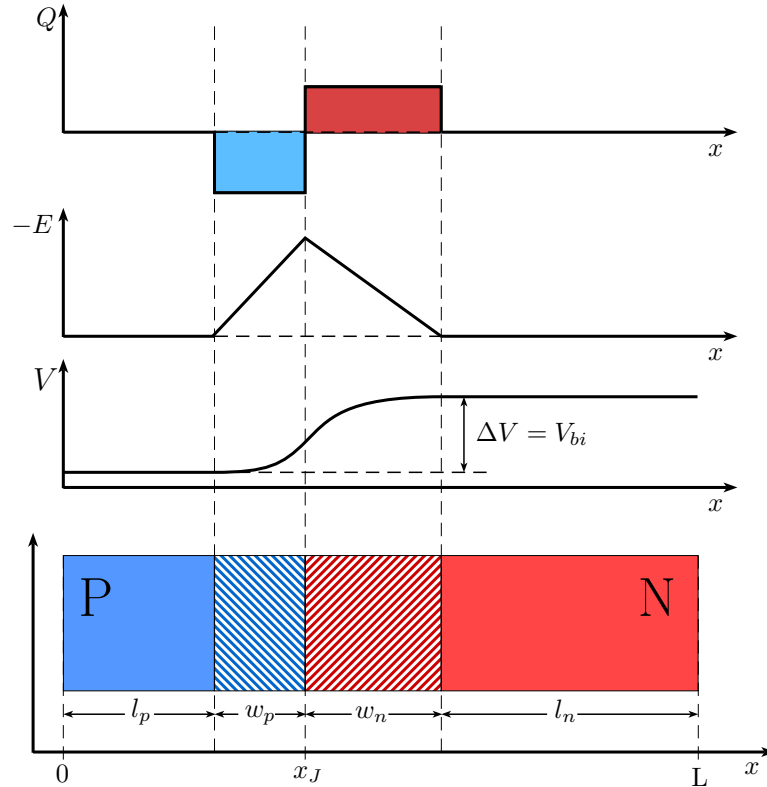


Figure 2.17: Schematic representation of different zones in a PN junction.

With the assumptions made above, and considering that semiconductor layers have high quality and an abrupt interface between the ‘P’ and ‘N’ sides with no intermediate energetic states due to imperfections, one can make further approximations that permit to reach to an analytical solution for the total current as a function of voltage.

In order to solve for current, transport equations as Drift-Diffusion in Eqs.(2.90) are used. These expressions are further simplified when considering each specific region separately. In this manner, no electric field is considered to be present at the neutral regions and the expression for current is only diffusion dependent and therefore decoupled from Poisson’s equation. Other main consequence for neutral regions is that recombination rate is linearized depending only on minority carriers according to Eq.(2.141). This allows to solve independently the effect of voltage from that of light, obtaining a solution in the dark under bias and a solution under illumination which are later superimposed. The derivation of the solution using this procedure can be found in most literature on semiconductor devices, for this reason only the

relevant equations are presented ahead.

The first significant value to obtain is the width of the depletion layer at each side of the junction (and therefore the total width). This is obtained solving Poisson's equation assuming the potential only varies through the SCR, which is considered true also when external bias is applied. This yields

$$w_p = \sqrt{\frac{2\epsilon_s(V_{bi} - V_{app})}{q} \left(\frac{N_A}{N_D(N_A + N_D)} \right)}, \quad (2.146a)$$

$$w_n = \sqrt{\frac{2\epsilon_s(V_{bi} - V_{app})}{q} \left(\frac{N_D}{N_A(N_A + N_D)} \right)}, \quad (2.146b)$$

at the p and n sides respectively. Thus, the total width of the SCR is

$$w_{SCR} = w_p + w_n = \sqrt{\frac{2\epsilon_s(V_{bi} - V_{app})}{q} \left(\frac{1}{N_A} + \frac{1}{N_D} \right)}. \quad (2.147)$$

With this the potential across the device is fully determined under the depletion region approximation, defined here as V_{DRA} . The most common reference system when defining the zones of a PN junction is to place $x = 0$ at the junction, in this case this is defined at the start of the device, as shown in Fig. 2.17 with l_p and l_n the lengths of the neutral regions at the p and n sides respectively. With this reference system the voltage profile is given by

$$V_{DRA}(x) = \begin{cases} V_P & 0 < x < l_p \\ (eN_A/\epsilon_s) \left((x - x_J)^2 + 2w_p(x - x_J) + w_p^2 \right) + V_P & l_p < x < x_J \\ (eN_D/\epsilon_s) \left((x - x_J)^2 + 2w_n(x - x_J) - w_n^2 \right) + V_N & x_J < x < x_J + w_n \\ V_N & x_J + w_n < x < L \end{cases} \quad (2.148)$$

where as mentioned, voltage describes parabolic profiles across the SCR.

2.5.2 Solution for J(V)

Having specified the length of each region it is possible to obtain the analytical expressions for the current at each portion under bias and under illumination. The specific solution presented here considers a generation profile given by Eq.(2.121) which provides a generation current. Through the use of the diffusion constants given by Eq.(2.89), the diffusion lengths are defined as

$$L_n = \sqrt{D_n\tau_n}, \quad (2.149a)$$

$$L_p = \sqrt{D_p\tau_p}, \quad (2.149b)$$

for electrons and holes, respectively. It is also assumed that each neutral region is thick compared to the respective diffusion length of the minority carrier.

With this, conditions are needed at the boundary of each section. For minority carriers at the edge between the SCR and the neutral regions, the condition is obtained assuming the separation in the Fermi level of carriers is constant through the SCR and given by the applied voltage, eV_{app} ; with this $n(l_p)$ and $p(x_J + w_n)$ are obtained through equilibrium statistics. On the other hand, the boundary conditions at the external surfaces are given by the expressions for surface recombination velocities in Eqs.(2.142) and (2.143), which considering absence of electric field reduce to

$$D_n \left. \frac{dn}{dx} \right|_{x=0} = -S_n (n(x=0) - n_0), \quad (2.150a)$$

$$-D_p \left. \frac{dp}{dx} \right|_{x=L} = S_p (p(x=L) - p_0). \quad (2.150b)$$

Solving the continuity equation under these conditions delivers in each case a voltage dependent, and a light dependent current [31]. Because the current needs to be constant across the device, the total current can be expressed as

$$J_T(V_{app}) = J_n(l_p) + J_p(l_p) = J_n(l_p) + J_p(x_J + w_n) + J_{scr}, \quad (2.151)$$

considering that the current of the space charge region J_{scr} , is the difference between evaluating at l_p and $x_J + w_n$. The differential system obtained from the depletion region approximation can only be solved analytically for a specific wavelength (energy) for the terms that depend on the generation profile. Thus, for $J_n(l_p)$

$$J_n(l_p) = J_{n,diff}(V_{app}, l_p) + J_{n,light}(l_p) = J_{n,diff}(V_{app}, l_p) + \int j_{n,light}(E, l_p) dE. \quad (2.152)$$

The general solution for each of this contributions is, respectively,

$$J_{n,diff} = en_i^2 \frac{D_n}{N_A L_n} \frac{S_n \cosh\left(\frac{l_p}{L_n}\right) + \frac{D_n}{L_n} \sinh\left(\frac{l_p}{L_n}\right)}{\frac{D_n}{L_n} \cosh\left(\frac{l_p}{L_n}\right) + S_n \sinh\left(\frac{l_p}{L_n}\right)} \left(\exp\left(\frac{eV_{app}}{k_B T_L}\right) - 1 \right), \quad (2.153)$$

$$j_{n,light}(E, l_p) = -\frac{e(1 - R_c) \Phi \alpha_c L_n}{\alpha_c^2 L_n^2 - 1} \times \left[\frac{\exp(-\alpha_c l_p) \left(S_n \cosh\left(\frac{l_p}{L_n}\right) + \frac{D_n}{L_n} \sinh\left(\frac{l_p}{L_n}\right) \right) - \left(S_n + \frac{D_n}{L_n} \alpha_c L_n \right)}{\frac{D_n}{L_n} \cosh\left(\frac{l_p}{L_n}\right) + S_n \sinh\left(\frac{l_p}{L_n}\right)} \right. \\ \left. + \alpha_c L_n \exp(-\alpha_c l_p) \right]. \quad (2.154)$$

Analogously for holes, the current evaluated at the border of the SCR and the n neutral region is

$$J_p(x_J + w_n) = J_{p,diff}(V_{app}, x_J + w_n) + J_{p,light}(x_J + w_n)$$

$$= J_{p,\text{diff}}(V_{\text{app}}, x_J + w_n) + \int j_{p,\text{light}}(E, x_J + w_n) dE. \quad (2.155)$$

The solution to each of these components is

$$J_{p,\text{diff}} = en_i^2 \frac{D_p}{N_D L_p} \frac{S_p \cosh\left(\frac{l_n}{L_p}\right) + \frac{D_p}{L_p} \sinh\left(\frac{l_n}{L_p}\right)}{\frac{D_p}{L_p} \cosh\left(\frac{l_n}{L_p}\right) + S_p \sinh\left(\frac{l_n}{L_p}\right)} \left(\exp\left(\frac{eV_{\text{app}}}{k_B T_L}\right) - 1 \right), \quad (2.156)$$

$$j_{p,\text{light}}(E, x_J + w_n) = -\frac{e(1-R_c)\Phi\alpha_c L_p}{\alpha_c^2 L_p^2 - 1} \exp(-\alpha_c(x_J + w_n)) \\ \times \left[\frac{\left(S_p \cosh\left(\frac{l_n}{L_p}\right) + \frac{D_p}{L_p} \sinh\left(\frac{l_n}{L_p}\right) \right) - \left(S_p - \frac{D_p}{L_p} \alpha_c L_p \right) \exp(-\alpha_c l_n)}{\frac{D_p}{L_p} \cosh\left(\frac{l_n}{L_p}\right) + S_p \sinh\left(\frac{l_n}{L_p}\right)} - \alpha_c L_p \right]. \quad (2.157)$$

The current density generated at the SCR is often referred to as the recombination-generation current. Recombination current is voltage dependent, while carrier generation is light dependent. Thus, similarly as for neutral regions, the current at the SCR is

$$J_{\text{scr}} = J_{\text{rec}}(V_{\text{app}}) + J_{\text{gen}} = J_{\text{rec}}(V_{\text{app}}) + \int j_{\text{gen}}(E) dE, \quad (2.158)$$

where both terms are integrated across the whole width of the SCR. Keeping in mind that the generation across the device is given by Eq.(2.121) and the number of carriers by the number of photons absorbed, the generation term is expressed as

$$j_{\text{gen}}(E) = e\Phi(1-R_c)\exp(-\alpha_c l_p)(1-\exp(-\alpha_c w_{\text{scr}})). \quad (2.159)$$

For the recombination current, a common approach is to consider SRH recombination to be dominant. With this, the integral across the SCR yields

$$J_{\text{rec}}(V_{\text{app}}) = \frac{en_i w_{\text{scr}}}{\sqrt{\tau_n \tau_p}} \frac{2 \sinh(eV_{\text{app}}/2k_B T_L) \pi}{e(V_{\text{bi}} - V_{\text{app}})/k_B T_L 2}, \quad (2.160)$$

which is the maximum value, considering a large forward bias. Expression in Eq.(2.160) is often approximated as

$$J_{\text{rec}}(V_{\text{app}}) \approx \frac{en_i w_{\text{scr}}}{\sqrt{\tau_n \tau_p}} \left(\exp\left(\frac{eV_{\text{app}}}{2k_B T_L}\right) - 1 \right) = J_{\text{rec},0} \left(\exp\left(\frac{eV_{\text{app}}}{2k_B T_L}\right) - 1 \right), \quad (2.161)$$

which depicts its behavior regarding voltage. Similarly, $J_{n,\text{diff}}$ and $J_{p,\text{diff}}$, from Eqs.(2.153) and (2.153) respectively, are combined into

$$J_{\text{diff}}(V_{\text{app}}) = J_{\text{diff},0} \left(\exp\left(\frac{eV_{\text{app}}}{k_B T_L}\right) - 1 \right), \quad (2.162)$$

with $J_{\text{diff},0}$ being

$$J_{\text{diff},0} = en_i^2 \frac{D_n}{N_A L_n} \frac{S_n \cosh\left(\frac{l_p}{L_n}\right) + \frac{D_n}{L_n} \sinh\left(\frac{l_p}{L_n}\right)}{\frac{D_n}{L_n} \cosh\left(\frac{l_p}{L_n}\right) + S_n \sinh\left(\frac{l_p}{L_n}\right)}$$

$$+en_i^2 \frac{D_p}{N_D L_p} \frac{S_p \cosh\left(\frac{l_n}{L_p}\right) + \frac{D_p}{L_p} \sinh\left(\frac{l_n}{L_p}\right)}{\frac{D_p}{L_p} \cosh\left(\frac{l_n}{L_p}\right) + S_p \sinh\left(\frac{l_n}{L_p}\right)}. \quad (2.163)$$

Recombination current J_{rec} should also incorporate a contribution of other types of recombination, which is very commonly neglected. In the case of radiative recombination the current presents a voltage dependency analogue to diffusion current in Eq.(2.162). Both of these voltage dependent currents are normally combined into what is referred to as the *dark current* J_{dark} , approximating its exponential behavior using an *ideality factor* m [31]. This yields

$$J_{\text{dark}} = J_{\text{diff}} + J_{\text{rec}} \approx J_{\text{dark},0} \left(\exp\left(\frac{eV_{\text{app}}}{mk_B T_L}\right) - 1 \right), \quad (2.164)$$

meaning that having $m = 1$ is similar to having an ideal diode and diffusion and/or radiative recombination currents dominate, while m reaching 2 implies SRH is dominant. In real cells a m has been observed to be closer to 2 at lower bias, while getting closer to the unity for higher voltages [31]. $J_{\text{dark},0}$, commonly referred to as J_0 , is called the recombination parameter and is widely used for solar cell modeling. A thorough discussion on the physical meaning of this parameter was performed by Cuevas [61]. This approximation helps presenting the current voltage dependency in a similar manner to the diode equation, while combining light generating currents gives

$$J_{\text{sc}} = J_{\text{n,light}} + J_{\text{p,light}} + J_{\text{gen}}, \quad (2.165)$$

which is called the short circuit current because is the value of the maximum obtainable current when $V_{\text{app}} = 0$. With this the current-voltage behavior is simply expressed as

$$J(V) = J_{\text{sc}} - J_{\text{dark},0} \left(\exp\left(\frac{eV_{\text{app}}}{mk_B T_L}\right) - 1 \right). \quad (2.166)$$

Figure 2.18 presents the characteristic curves given by the simplified current voltage expression in Eq.(2.166). Different values of the ideality factor m were used, showing how much the curve can be fitted using only this parameter.

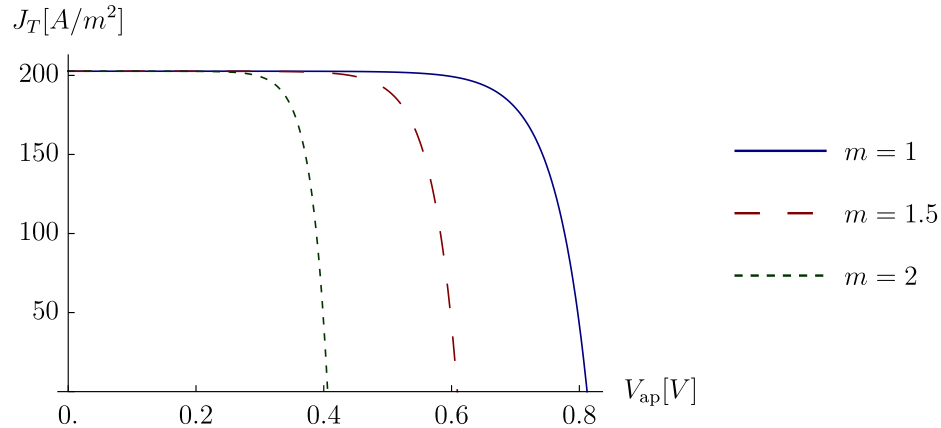


Figure 2.18: Current-voltage characteristic curves for solar cells using the depletion region approximation and different values of m .

The present literature review summarizes the basic theoretical concepts regarding semiconductor physics, required for both a correct execution of the methodology, described ahead, as well as a proper analysis of the results. The first section aims to mathematically explain the main physical concepts used to quantify the behavior of charge carriers within semiconductor materials. The origin and validity of these approximations is explained. These quantifications are considerably useful for a first order analysis regarding the range of operation under which the studied configuration is and, therefore, the degree of simplification that is allowed. The second section briefly describes the origin of the hydrodynamic model for semiconductors. The model is built using the Boltzmann transport equation as a starting point in order to define macroscopic variables that simplify the analysis. The Drift-Diffusion model is also presented, which can be obtained through further simplifications of the latter. The definition of these macroscopic variables implies the requirement of certain parameters, each with different empirical or analytical expressions depending on the operating conditions under consideration. Among these, transport parameters were defined in section 3, where different models for carrier mobilities and relaxation times were reviewed. High energy models are included, which are needed for the configurations analysed in the present work. Other key physical processes that affect the behavior of carriers within a semiconductor are the collision phenomena, which are described in section 4. The main expressions available to be used in conjunction with a hydrodynamic model are presented, classified as generation and recombination processes. In particular, the definition of surface recombination velocities is essential for the implementation of appropriate boundary conditions. Finally, the simplest way of obtaining a description of the behavior of carriers within a solar cell under operation is presented in section 5, which is the solution of the depletion region approximation model. This is extremely useful in order to verify if the solution given by a more complex model is within the expected order of magnitude, as well as to evaluate the importance of considering additional physics into the solution.

Chapter 3

Methodology

This chapter explains how the objectives of this thesis work are fulfilled, presenting the general methodology to obtain the solution of the problems. More specifically, the method utilized to obtain a solution for the simulation of single junction solar cells is presented. This is a similar methodology as proposed by Osses [18], along with certain concepts from the work of Jünger [32]. For this purpose, the general context of the problem to be solved is explained in Section 3.1 along with the studies that were performed. An example of a hydrodynamic (HD) model is presented in Section 3.2, which is used for explaining the methodology. The boundary conditions are given in Section 3.3. The solution of these problems is obtained using the mathematical methods explained in Sections 3.4 and 3.5. Lastly, the numerical methods used to solve the system and simulate the device are presented in Section 3.6.

3.1 Problem Description

According to what was stated in the objectives of this work, the general goal is to study the effects of hot carriers in the behavior of a single-junction solar cell. Nowadays, commercial solar cells are composed of several layers that deal with specific issues and improve their efficiency but the basic functional structure of all of them is the PN junction. This is true for all semiconductor devices. For this reason, single PN junctions have been thoroughly studied. In the case of a solar cell, these layers are distributed perpendicular to the thickness of the device and the ratio between the light absorbing area and the thickness is large, meaning they are suitable for one dimensional simulation. Although sometimes a two or three dimensional constitutive unit is simulated in order to include two dimensional effects of the transport of carriers to the contacts, one dimensional simulation is enough for most purposes. In this manner, all of the simulations in this thesis are done considering a single junction, one dimensional PN junction as depicted in Fig. 3.1. Here, length L represents the total thickness of both P and N layers which are united at the junction depth x_j . The origin $x = 0$ is defined at the P side of the junction, which is the sun-facing surface.

As explained in the literature review, a built-in potential gap develops between the junction which is defined here to be zero at the N side ($x = L$) and negative at the P boundary with the magnitude of the difference between the built in potential V_{bi} and the applied positive bias V_{app} . Incoming light enters through the P side of the junction and produces a length and

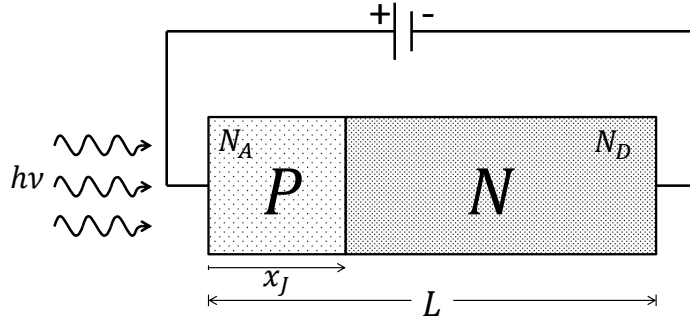


Figure 3.1: Scheme of a PN junction solar cell.

frequency dependent generation rate profile $g(x, \lambda)$, conforming a total generation profile of $G(x)$, according to Eq.(2.122). For single junction devices the doping profile is expressed as a function of the length $C(x)$ and is given in its dimensional form by

$$C(x) = \begin{cases} -N_A & 0 < x \leq x_J \\ N_D & x_J < x < L \end{cases}, \quad (3.1)$$

meaning the junction is considered to be abrupt. Both layers are established to be made up of the same material (GaAs in this case), maintaining a homogeneous energy gap through the device and changing only the polarity of the doping. This is referred to as a *homojunction*. The opposite case, called a *heterojunction*, generates a discontinuity in the gap level. This is currently implemented in solar cells, boosting the efficiency of newly developed amorphous silicon solar cells [62], even reaching an *internal quantum efficiency* (IQE) of near 100% [63]. Quantum wells, wires or dots are also an example of abrupt heterojunctions currently investigated for their use in solar cells. This method is physically more complicated to achieve, numerically harder to analyze and is left out of the scope of this study.

The key feature of hydrodynamic models in order to study the effect of hot-carriers is to consider that lattice and carrier temperatures are out of thermal equilibrium. This is fundamental in order to reproduce the role that high energy electrons or holes play in the performance of the device. Carrier temperature is often associated only to the velocity of the particles which, in turn, is expressed as a function of the electric field, as presented in Eq.(4.7). Using carrier temperature as a new variable means a new dimension into the analysis and might bring up unexpected outcomes that would have been kept unnoticed otherwise. Many times parameters of simpler models are fitted in order to explain phenomena that could be explained due to high energy carriers. For this reason, being consistent while trying to isolate these phenomena can be difficult. With this in mind, the most appropriate simplifications to be performed on each part of the model are discussed in Chapter 4.

3.2 The Hydrodynamic Model

From the expressions that describe the behavior of semiconductor devices presented at the literature review, a hydrodynamic model can be condensed for device simulation. The def-

initiation of a hydrodynamic model for semiconductors is not restricted to a single system of equations, but refers to the similarity they have with the governing equations in fluid dynamics. Transport equations presented in Section 2.2 are the general expressions to represent almost any semiconductor device, within the restrictions discussed therein.

The model presented below is an example in order to demonstrate the non-dimensional form of the system. It also serves to illustrate the procedure to obtain a numerical solution. Since these equations are written in a non-dimensional form in the following section, they are presented with the superscript $*$ to emphasize they are in their dimensional form. The main assumptions of this model are the following:

- Hole temperature is in equilibrium with lattice temperature $T_p = T_L$.
- The approximation $\frac{1}{2}m_n u_n^2 \ll k_B T_n$ is used for the energy flow term $n\mathbf{S}_n$.

With these assumptions, only the energy balance for electrons needs to be solved, and high-field effects are considered only for electrons. As it was stated, the problem is solved in one dimension, yielding

$$\frac{\partial^2 V^*}{\partial x^{*2}} = -\frac{e}{\epsilon_s} (p^* - n^* + C^*), \quad (3.2a)$$

$$\frac{\partial n^*}{\partial t^*} + \frac{\partial(u_n^* n^*)}{\partial x^*} = (G^* - R^*), \quad (3.2b)$$

$$\frac{\partial p^*}{\partial t^*} + \frac{\partial(u_p^* p^*)}{\partial x^*} = (G^* - R^*), \quad (3.2c)$$

$$\frac{\partial u_n^*}{\partial t^*} + u_n^* \frac{\partial u_n^*}{\partial x^*} = \frac{e}{m_n} \frac{\partial V^*}{\partial x^*} - \frac{k_B}{m_n n^*} \frac{\partial(n^* T_n^*)}{\partial x^*} - \frac{u_n^*}{\tau_{m,n}}, \quad (3.2d)$$

$$\frac{\partial u_p^*}{\partial t^*} + u_p^* \frac{\partial u_p^*}{\partial x^*} = -\frac{e}{m_p} \frac{\partial V^*}{\partial x^*} - \frac{k_B}{m_p p^*} \frac{\partial(p^* T_L^*)}{\partial x^*} - \frac{u_p^*}{\tau_{m,p}}, \quad (3.2e)$$

$$\begin{aligned} \frac{\partial T_n^*}{\partial t^*} + u_n^* \frac{\partial T_n^*}{\partial x^*} + \frac{2}{3} T_n^* \frac{\partial u_n^*}{\partial x^*} + \frac{2}{3n^* k_B} \frac{\partial}{\partial x^*} \left(-\frac{3k_B^2 \tau_{m,n}}{2} n^* T_n^* \frac{\partial T_n^*}{\partial x^*} \right) \\ = -\frac{T_n^* - T_L^*}{\tau_{\epsilon,n}} + \frac{2m_n}{3k_B \tau_{m,n}} \left(1 - \frac{\tau_{m,n}}{2\tau_{\epsilon,n}} \right) u_n^{*2}, \end{aligned} \quad (3.2f)$$

$$C_L \frac{\partial T_L^*}{\partial t^*} = \frac{\partial}{\partial x^*} \left(\kappa_L \frac{\partial T_L^*}{\partial x^*} \right) + \frac{3k_B n^*}{2} \left(\frac{T_n^* - T_L^*}{\tau_{\epsilon,n}} \right) + \frac{n^* m_n u_n^{*2}}{2\tau_{\epsilon,n}} + \frac{p^* m_p u_p^{*2}}{2\tau_{\epsilon,p}}, \quad (3.2g)$$

with C^* given by Eq.(3.1). Net generation rate is given by $G_n = G_p = G$ and $R_n = R_p = R$, considering only band to band processes. Equation (3.2a) comes from the one dimensional version of Gauss's law in Eq.(2.43). Continuity Eqs.(3.2b) and (3.2c) are obtained from Eqs.(2.58) with the collision terms expressed in generic form as in Eqs.(2.69). This means that the complete expressions for recombination, as presented in Section 2.4.2 is used indirectly. Velocity Eqs.(3.2d) and (3.2e), which come from the momentum balance, are the same as Eqs.(2.63) considering only collisions of each carrier with the lattice, therefore given by the expressions in Eqs.(2.72). Equation (3.2f) comes from the energy balance for elec-

trons in Eq.(2.66a), approximating the heat flux by Fourier's law as presented in eq.(2.79), Wiedemann-Franz law for thermal conductivity and the temperature scattering terms given by Eq.(2.75).

3.3 Boundary Conditions

When simulating electronic devices it is crucial to impose appropriate boundary conditions fitting the context of the problem. In this regard, the conditions assumed for each variable are discussed ahead along with their validity under specific circumstances. Every expression is given in a one-dimensional form. A discussion on the consequences of varying these values is presented in Chapter 4.

3.3.1 Voltage

Electrostatic potential, or voltage, presents a variation equivalent to the difference between the built in voltage V_{bi} (Eq.(2.144)), and the applied voltage V_{app} whether it is positive or negatively biased. Since this potential is relative to a reference value, any value could be chosen for one end, while maintaining the amount of voltage drop. In this manner, we choose the right side ($x = L$) to be zero, while the left side ($x = 0$) is equivalent to the aforementioned voltage difference, hence

$$V^*(0, t) = V_{app} - V_{bi}, \quad (3.3a)$$

$$V^*(L, t) = 0. \quad (3.3b)$$

This is particularly true for devices where quasi neutral regions (QNR) are large enough for the voltage to drop fully at the depletion region. In a more general form, the perpendicular electric field difference at the boundary between two media will depend on the sheet charge density at the interface. Since ohmic contacts are being considered, the charges are balanced at the metal-semiconductor interface, therefore

$$\frac{\partial V^*}{\partial x^*}(0, t) = \frac{\partial V^*}{\partial x^*}(L, t) = 0, \quad (3.4)$$

which is obtained as a consequence if conditions given by Eq.(3.3) are used. In cases where electric field is used as a variable this means

$$E^*(0, t) = E^*(L, t) = 0. \quad (3.5)$$

3.3.2 Majority Carrier Densities

As for voltage, the boundary condition for majority carrier concentration is readily defined when the QNR is fully developed. Here, the carrier densities reach an equilibrium value

as discussed in Section 2.1.4. This means the contact is assumed to be far enough from the junction so that carriers do not get ionized and the carrier concentration is obtained by Eqs.(2.38) and (2.39). Moreover, considering that single donors are used for both P and N sides and the doping level is high (as commonly used in solar cells), boundary conditions for majority carriers are

$$p^*(0, t) = \frac{1}{2} \left(N_A + \sqrt{N_A^2 + 4n_i} \right) \approx N_A, \quad (3.6a)$$

$$n^*(L, t) = \frac{1}{2} \left(N_D + \sqrt{N_D^2 + 4n_i} \right) \approx N_D, \quad (3.6b)$$

remarking that the p -type semiconductor is located from $x^* = 0$ until the junction and from $x^* = x_J$ until the full length, the device is n -type. This condition could change if the boundary comes too close to the SCR, or if the semiconductor is degenerate.

3.3.3 Minority Carrier Densities

Majority carrier concentrations are usually orders of magnitude higher than the ones of minority carriers. However, minority carriers have a greater effect on the current. This is one of the basic assumptions when obtaining the analytical solution for the solar cell, presented in Section 2.5. Minority carriers are much more affected by changes in the bias or the generation level, which changes the Fermi level, therefore accordingly with Eqs.(2.42) the density also changes.

The boundary condition for these carriers is found through the expression for the surface recombination leak current, presented in Chapter 2 by Eqs.(2.142) and (2.142). Using the expression for current as a function of carrier density and velocity, given in Eq.(2.59), these equations can be rewritten as,

$$J_n(0, t) = -en^*(0, t)u_n^*(0, t) = -eS_n(n^*(0, t) - n_0), \quad (3.7a)$$

$$J_p(L, t) = ep^*(L, t)u_p^*(L, t) = eS_p(p^*(L, t) - p_0). \quad (3.7b)$$

This is a condition that relates current with carrier density at the surface. If velocity is used as a variable this expression can be simplified considering the fact that for solar cells normally

$$n^*(0, t) \gg n_0, \quad (3.8a)$$

$$p^*(L, t) \gg p_0, \quad (3.8b)$$

consequently

$$u_n^*(0, t) \approx S_n, \quad (3.9a)$$

$$u_p^*(L, t) \approx S_p, \quad (3.9b)$$

would be the boundary conditions for carrier velocities at the minority boundaries. In several occasions the velocity is found as an expression of other variables, such is the case of the DD model, where Eq.(3.7) leads to

$$\frac{D_n}{n^*(0,t)} \frac{\partial n^*}{\partial x^*}(0,t) - \mu_n \frac{\partial V^*}{\partial x^*}(0,t) = -S_n, \quad (3.10a)$$

$$-\frac{D_p}{p^*(L,t)} \frac{\partial p^*}{\partial x^*}(L,t) - \mu_p \frac{\partial V^*}{\partial x^*}(L,t) = S_p. \quad (3.10b)$$

These equations simply reduce to Eqs.(2.150) when conditions in Eqs.(3.4) are fulfilled.

3.3.4 Temperatures

Lattice temperature is considered here to be the bulk temperature of the semiconductor as a solid body. In this sense the boundary condition is imposed depending on the surrounding layers of the device and it is a variable that is reasonably simple to control. Accordingly, many types of boundary conditions would be physically reasonable. In the context of this thesis, Dirichlet type boundary conditions are imposed, defined as

$$T_L^*(0,t) = T_{LP}, \quad (3.11a)$$

$$T_L^*(L,t) = T_{LN}. \quad (3.11b)$$

In most cases it will be considered that $T_{LP} = T_{LN}$. The use of symmetric boundary conditions for the lattice temperature is supported by the fact that results from thermal modeling of photovoltaic solar cells show that the temperature of the semiconductor layer is mostly uniform along the normal axis [64]. On the other hand, the definition of boundary conditions for carrier temperatures is not as straightforward as for lattice temperature. The most common assumption is to consider that ohmic contacts force thermal equilibrium between lattice and carriers, thus

$$T_L^*(0,t) = T_n^*(0,t) = T_p^*(0,t), \quad (3.12a)$$

$$T_L^*(L,t) = T_n^*(L,t) = T_p^*(L,t), \quad (3.12b)$$

assuming Dirichlet boundary conditions for the temperatures of electrons and holes as well. In special cases, such as hot carrier solar cells, hot carrier extraction is achieved by means of energy selective contacts, then the definition of the boundary condition is debatable. Some boundary conditions different to those given by Eqs.(3.12) are used in this thesis, which are discussed in Chapter 4.

3.4 Nondimensionalization

A common practice when modeling semiconductor devices is to use scaled and non dimensional systems, which simplify the numerical solution, and the analysis of the results [45, 65]. The scaling shown in this section is presented using the non-dimensional version of Eqs.(3.2). The reference length corresponds to the device length (solar cell thickness) L . Carrier densities are scaled with a reference doping level N_0 , usually corresponding to the lowest doping level. All temperatures are scaled using T_0 , normally equal to 300[K]. Reference values are used for voltage, time and velocities, defined as V_0 , τ_0 and u_0 respectively, explicated ahead. Therefore, the non-dimensional variables are

$$x = x^*/L, \quad (3.13a)$$

$$t = t^*/\tau_0, \quad (3.13b)$$

$$V = V^*/V_0, \quad (3.13c)$$

$$n = n^*/N_0, \quad (3.13d)$$

$$p = p^*/N_0, \quad (3.13e)$$

$$u_n = u_n^*/u_0, \quad (3.13f)$$

$$u_p = u_p^*/u_0, \quad (3.13g)$$

$$T_n = T_n^*/T_0, \quad (3.13h)$$

$$T_L = T_L^*/T_0. \quad (3.13i)$$

The terms on the left-hand side of each equation are the non-dimensional expression for the corresponding variable. In order to better understand the physical meaning of the non-dimensional groups, the following parameters are introduced

$$U_T = \frac{k_B T_0}{e}, \quad (3.14)$$

$$\iota = \tau_{m0} \sqrt{\frac{k_B T_0}{m_{n0}}}, \quad (3.15)$$

$$\lambda_D = \sqrt{\frac{\epsilon_s k_B T_0}{e^2 N_0}} = \sqrt{\frac{\epsilon_s U_T}{e N_0}}, \quad (3.16)$$

where U_T is the thermal voltage, ι the mean free path for electrons and λ_D the Debye length. These parameters are defined using reference magnitudes for momentum relaxation time and effective mass, corresponding to the low-field values τ_{m0} and m_{n0} , given by

$$\tau_{m0} = \tau_{m,n}^{LF}(T_0, N_D), \quad (3.17)$$

$$m_{n0} = m_n(T_0), \quad (3.18)$$

which are calculated according to the relations presented in Sections 2.3 and 2.1 respectively. High field effects are considered for electrons expressing m_n , $\tau_{m,n}$ and $\tau_{\epsilon,n}$ as

$$m_n = m_{n0}\varphi_m, \quad (3.19)$$

$$\tau_{m,n} = \tau_{m0}\varphi_k, \quad (3.20)$$

$$\tau_{\epsilon,n} = \tau_{\epsilon0}\varphi_\epsilon, \quad (3.21)$$

where φ_m , φ_k and φ_ϵ are non dimensional parameters expressing the variation caused by high field effects on electron effective mass, momentum and energy relaxation times respectively. Holes are assumed to be in thermal equilibrium with lattice. Therefore, $\tau_{m,p}$, m_p and $\tau_{\epsilon,p}$ are only dependent of T_L , and $T_p = T_L$. For convenience, specific reference voltage, time and velocity are used,

$$V_0 = U_T, \quad (3.22)$$

$$u_0 = \frac{eU_T\tau_{m0}}{m_{n0}L}, \quad (3.23)$$

$$\tau_0 = \frac{L}{u_0}. \quad (3.24)$$

In order to simplify the presentation of the system of equations, the following non-dimensional groups are defined:

$$\varepsilon_n = \left(\frac{v}{L}\right)^2, \quad (3.25a)$$

$$\lambda = \frac{\lambda_D}{L}, \quad (3.25b)$$

$$\nu_n = \frac{\tau_{m0}}{\tau_{\epsilon0}}, \quad (3.25c)$$

$$\nu_p = \frac{\tau_{m,p}}{\tau_{\epsilon,p}}, \quad (3.25d)$$

$$m_r = \frac{m_{n0}}{m_p}, \quad (3.25e)$$

$$\gamma = \frac{\tau_{m0}}{\tau_{m,p}}, \quad (3.25f)$$

$$\chi = \frac{C_L}{k_B N_0}, \quad (3.25g)$$

$$\psi = \frac{\kappa L \tau_{m0}}{k_B N_0 L^2}. \quad (3.25h)$$

Using these changes of variables, the system given by Eqs.(3.2) yields

$$\frac{\partial^2 V}{\partial x^2} = -\frac{1}{\lambda^2} (p - n + C), \quad (3.26a)$$

$$\frac{\partial n}{\partial t} + \frac{\partial(u_n n)}{\partial x} = (G - R), \quad (3.26b)$$

$$\frac{\partial p}{\partial t} + \frac{\partial(u_p p)}{\partial x} = (G - R), \quad (3.26c)$$

$$\varepsilon_n \left[\frac{\partial u_n}{\partial t} + u_n \frac{\partial u_n}{\partial x} \right] = \frac{1}{\varphi_m} \left(\frac{\partial V}{\partial x} - \frac{1}{n} \frac{\partial(nT_n)}{\partial x} \right) - \frac{u_n}{\varphi_k}, \quad (3.26d)$$

$$\varepsilon_n \left[\frac{\partial u_p}{\partial t} + u_p \frac{\partial u_p}{\partial x} \right] = -m_r \left(\frac{\partial V}{\partial x} + \frac{1}{p} \frac{\partial(pT_L)}{\partial x} \right) - \gamma u_p, \quad (3.26e)$$

$$\begin{aligned} \partial_t T_n + u_n \frac{\partial T_n}{\partial x} + \frac{2}{3} T_n \frac{\partial u_n}{\partial x} - \frac{1}{n} \frac{\partial}{\partial x} \left(\frac{\varphi_k}{\varphi_m} n T_n \frac{\partial T_n}{\partial x} \right) = \\ - \frac{\nu_n}{\varphi_\epsilon \varepsilon_n} (T_n - T_L) + \frac{2}{3} \varphi_m u_n^2 \left(\frac{1}{\varphi_k} - \frac{\nu_n}{2\varphi_\epsilon} \right), \end{aligned} \quad (3.26f)$$

$$\chi \frac{\partial T_L}{\partial t} = \frac{\psi}{\varepsilon_n} \frac{\partial^2 T_L}{\partial x^2} + \frac{3}{2} \frac{\nu_n}{\varphi_\epsilon \varepsilon_n} n (T_n - T_L) + \frac{\varphi_m \nu_n}{\varphi_\epsilon} \frac{n u_n^2}{2} + \frac{\gamma}{m_r} \frac{\nu_p}{2} p u_p^2. \quad (3.26g)$$

The expressions for doping density, carrier generation and recombination are also non-dimensionalized as $C = C^*/N_0$ and $(G - R) = (G^* - R^*)/G_0$. The non-dimensional group G_0 is equal to

$$G_0 = \frac{N_0 u_0}{L}. \quad (3.27)$$

Referring to Eq.(3.25a), it can be observed that the Knudsen number for the electron flow is equivalent to $K_n = \iota/L = \sqrt{\varepsilon_n}$. In fluid dynamics, K_n indicates whether continuum or statistical mechanics approach should be used to model a problem. For most fluid problems, the Knudsen number is small, considering how much larger the characteristic length is compared to the mean free path. However, for modern electronic devices the mean free path approaches the length of the device, which is what produces the need of more accurate models. Nevertheless, the problems solved in this work have a configuration such that $K_n \ll 1$, and therefore the use of macroscopic models is appropriate.

The non-dimensional groups given by Eqs.(3.25c) and (3.25d) relate the momentum scattering with the energy delivered as heat to the lattice. Therefore, they are closely related to the Prandtl numbers P_r for electrons and holes respectively [66]. This number has been proven to have a correlation with the existence of velocity overshoot in devices where high energy processes are important [11, 67].

The expression for ε_n can also be rearranged in order to be defined as

$$\varepsilon_n = \frac{u_0 L}{L^2/\tau_{m0}} = R_e, \quad (3.28)$$

which is a possible definition for a Reynolds number R_e for the electron flow. The term L^2/τ_{m0} expresses viscous effects of the electron cloud.

3.5 Asymptotic Approximation

Using the non-dimensional version of the model presented above, an asymptotic approximation is made in order to simplify the equations. Given that the Knudsen number is considered to be small, then it follows that $\varepsilon_n \ll 1$. This means that the kinetic energy corresponding to the velocity needed to cross the device in time τ_{m0} is very large compared to the thermal energy. Moreover, $\nu_n \ll 1$ and $\nu_p \ll 1$ will be satisfied if the kinetic energy associated with the saturation velocity is much smaller than the thermal energy [45]. Consequently, assuming $\varepsilon_n \rightarrow 0$, $\nu_n \rightarrow 0$ and $\nu_p \rightarrow 0$, the steady state version of Eqs.(3.26b), (3.26c), (3.26d), (3.26e), (3.26f) and (3.26g) is

$$\frac{\partial(u_n n)}{\partial x} = (G - R), \quad (3.29a)$$

$$\frac{\partial(u_p p)}{\partial x} = (G - R), \quad (3.29b)$$

$$u_n = \frac{\varphi_k}{\varphi_m} \left(\frac{\partial V}{\partial x} - \frac{1}{n} \frac{\partial(n T_n)}{\partial x} \right), \quad (3.29c)$$

$$u_p = -\mu \left(\frac{\partial V}{\partial x} + \frac{1}{p} \frac{\partial(p T_L)}{\partial x} \right), \quad (3.29d)$$

$$u_n \frac{\partial T_n}{\partial x} + \frac{2}{3} T_n \frac{\partial u_n}{\partial x} - \frac{1}{n} \frac{\partial}{\partial x} \left(\frac{\varphi_k}{\varphi_m} T_n n \frac{\partial T_n}{\partial x} \right) = -\frac{\nu_n}{\varphi_\varepsilon \varepsilon_n} (T_n - T_L) + \frac{2\varphi_m}{3\varphi_k} u_n^2, \quad (3.29e)$$

$$\psi \frac{\partial^2 T_L}{\partial x^2} + \frac{3}{2} \frac{\nu_n}{\varphi_\varepsilon} n (T_n - T_L) = 0. \quad (3.29f)$$

The following section presents the numerical method used to solve these equations under the assumption of only low-field effects. This means $\varphi_m = \varphi_k = \varphi_\varepsilon = 1$, and Eqs.(3.29c), (3.29e) and (3.29f) respectively become

$$u_n = \frac{\partial V}{\partial x} - \frac{1}{n} \frac{\partial(n T_n)}{\partial x}, \quad (3.30a)$$

$$u_n \frac{\partial T_n}{\partial x} + \frac{2}{3} T_n \frac{\partial u_n}{\partial x} - \frac{1}{n} \frac{\partial}{\partial x} \left(T_n n \frac{\partial T_n}{\partial x} \right) = -\frac{\nu_n}{\varepsilon_n} (T_n - T_L) + \frac{2}{3} u_n^2, \quad (3.30b)$$

$$\psi \frac{\partial^2 T_L}{\partial x^2} + \frac{3}{2} \nu_n n (T_n - T_L) = 0. \quad (3.30c)$$

Accordingly, the non-dimensional version of the DD current equations is

$$u_n = \frac{\partial V}{\partial x} - \frac{1}{n} \frac{\partial n}{\partial x}, \quad (3.31a)$$

$$u_p = -\mu \left(\frac{\partial V}{\partial x} + \frac{1}{p} \frac{\partial p}{\partial x} \right). \quad (3.31b)$$

3.6 Numerical Method

The following section presents a brief description of the procedure followed in order to obtain a numerical solution for the system presented in Section 3.2. Newton's method is applied on the discrete system of equations, and a solution is obtained after several iterations. A detailed description is presented in Appendix B, in case the numerical code needs to be employed or modified. The implemented routine is explained schematically, describing the steps taken in order to achieve convergence. Even though different versions of the HD model were solved in this work, the procedure to get a solution is the same. For this reason, the system in Eqs.(3.2) is used as an example.

3.6.1 Newton's Method

Even though the asymptotic approximation for the HD model simplifies the equations considerably, many non-linearities are still present. In order to deal with these non-linearities remaining in the system, Newton's method is applied. The system is expressed in terms of the vector w which gathers all the unknowns,

$$w = \begin{pmatrix} V \\ n \\ p \\ T_n \\ T_L \end{pmatrix}. \quad (3.32)$$

The variables u_n and u_p are left out because they are obtained explicitly by the expressions given by Eqs.(3.30a) and (3.29d) respectively. With this, the model comprised by Eqs.(3.26a), (3.29a), (3.29b), (3.30b) and (3.30c) can be written as a function of the variable w as

$$F(w) = \begin{pmatrix} F_V(w) \\ F_n(w) \\ F_p(w) \\ F_c(w) \\ F_L(w) \end{pmatrix} = 0, \quad (3.33)$$

where each homogeneous function is equivalent to

$$F_V = \frac{\partial^2 V}{\partial x^2} + \frac{1}{\lambda^2} (p - n + C) = 0, \quad (3.34a)$$

$$F_n = \frac{\partial(u_n n)}{\partial x} - (G - R) = 0, \quad (3.34b)$$

$$F_p = \frac{\partial(u_p p)}{\partial x} - (G - R) = 0, \quad (3.34c)$$

$$F_c = \frac{\partial}{\partial x} \left(T_n n \frac{\partial T_n}{\partial x} \right) - \frac{5}{3} \frac{\partial}{\partial x} (n T_n u_n) - n \frac{\partial}{\partial x} (T_n u_n) \quad (3.34d)$$

$$+ \frac{1}{3} n T_n \frac{\partial u_n}{\partial x} - \frac{\nu_n}{\varepsilon_n} n (T_n - T_L) + \frac{2}{3} n u_n^2 = 0,$$

$$F_L = \psi \frac{\partial^2 T_L}{\partial x^2} + \frac{3}{2} \nu_n n (T_n - T_L) = 0, \quad (3.34e)$$

with the expressions for u_n and u_p given by Eqs.(3.30a) and (3.29d) respectively. The linear application $F(w)$, satisfies

$$F(w + \delta w) = F(w) + DF(w) \cdot \delta w + o(\delta w) \quad (3.35)$$

where δw is a small variation from w , and $DF(w)$ corresponds to the Jacobian matrix of $F(w)$,

$$DF(w) = \begin{bmatrix} \frac{\partial F_V}{\partial V} & \frac{\partial F_V}{\partial n} & \frac{\partial F_V}{\partial p} & \frac{\partial F_V}{\partial T_c} & \frac{\partial F_V}{\partial T_L} \\ \frac{\partial F_n}{\partial V} & \frac{\partial F_n}{\partial n} & \frac{\partial F_n}{\partial p} & \frac{\partial F_n}{\partial T_c} & \frac{\partial F_n}{\partial T_L} \\ \frac{\partial F_p}{\partial V} & \frac{\partial F_p}{\partial n} & \frac{\partial F_p}{\partial p} & \frac{\partial F_p}{\partial T_c} & \frac{\partial F_p}{\partial T_L} \\ \frac{\partial F_c}{\partial V} & \frac{\partial F_c}{\partial n} & \frac{\partial F_c}{\partial p} & \frac{\partial F_c}{\partial T_c} & \frac{\partial F_c}{\partial T_L} \\ \frac{\partial F_L}{\partial V} & \frac{\partial F_L}{\partial n} & \frac{\partial F_L}{\partial p} & \frac{\partial F_L}{\partial T_c} & \frac{\partial F_L}{\partial T_L} \end{bmatrix}. \quad (3.36)$$

The iterations are performed considering that for a given approximation of the solution w^j , δw^j can be found such that $w^j + \delta w^j$ approximately satisfies $F(w^j + \delta w^j) \approx 0$. Therefore, using Eq.(3.35) and assuming $o(\delta w) \approx 0$, δw^j is obtained by solving

$$DF(w^j) \cdot \delta w^j = -F(w^j). \quad (3.37)$$

The same procedure is performed for the new approximation of the solution given by

$$w^{j+1} = w^j + \delta w^j. \quad (3.38)$$

When $\delta w \rightarrow 0$, the system converges to a solution. This is heavily dependent on the initial approximation w^0 .

3.6.2 Discretization

Newton's method is implemented through a one-dimensional finite difference scheme. The fundamentals of the finite difference method are not described here, but can be found extensively in literature [68]. The length of the device is divided in $N_u + 1$ intervals equally

spaced, which means there are N_u nodes between the boundaries. Each interval has an equal length given by

$$\Delta x = \frac{L}{N_u + 1}. \quad (3.39)$$

For the non-dimensional case, $L = 1$. This means each node is an unknown, and the numerical goal is to find the vector δw , which consists of $5 \times N_u$ unknowns. The position of a certain node i is denoted as x_i with $i \in \{1, \dots, N_u\}$. In the finite difference method, derivatives are approximated by using the nodes near by to a certain position. In this manner, the first derivative of a function v evaluated at x_i , is approximated by

$$\frac{\partial v}{\partial x}(x_i) \approx \frac{v_{i+1} - v_i}{\Delta x} \equiv \partial_x^R v, \quad (3.40a)$$

$$\frac{\partial v}{\partial x}(x_i) \approx \frac{v_i - v_{i-1}}{\Delta x} \equiv \partial_x^L v, \quad (3.40b)$$

$$\frac{\partial v}{\partial x}(x_i) \approx \frac{v_{i+1} - v_{i-1}}{2\Delta x} \equiv \partial_x^C v, \quad (3.40c)$$

depending whether it needs to be approximated to the right, left or centered respectively. The right-hand side of each equation is the notation used in this work in order to simplify the presentation of the methodology. Similarly, the second order derivative is approximated by

$$\frac{\partial^2 v}{\partial x^2}(x_i) \approx \frac{v_{i+1} - 2v_i + v_{i-1}}{\Delta x^2} \equiv \partial_{xx} v, \quad (3.41)$$

An intrinsic characteristic of PN junctions is the existence of abrupt gradients in the area surrounding the junction. This is specially true for electric potential and carrier concentrations. Therefore, special attention needs to be taken for the discretization to be centered and consistent. In this case, gradients or terms including gradients like velocities, are discretized at middle points between nodes. For example, electron velocity is expressed discretely as

$$u_{n_{i+1/2}} = \partial_x^R V - \frac{1}{\bar{n}_R} \partial_x^R (nT_n) \equiv u_n^R, \quad (3.42)$$

where $\bar{n}_R = n_{i+1/2}$ is the average value of electron density to the right of the i -th node

$$\bar{n}_R = \frac{n_{i+1} + n_i}{2}. \quad (3.43)$$

The expressions are analogue for electron velocity at $(i - 1/2)$, defined as $u_{n_{i-1/2}} = u_n^L$. In this manner, the discretization of the divergence of the velocity is obtained centered as

$$\frac{\partial u_n}{\partial x} \approx \frac{u_n^R - u_n^L}{\Delta x}. \quad (3.44)$$

The Jacobian in Eq.(3.36) is calculated for the discrete versions of the equations in $F(w)$. The specific components of the matrix $DF(w)$ are presented in Appendix B.

3.6.3 Boundary Conditions for Newton's Method

As mentioned in Section 3.3, most boundary conditions are Dirichlet, with the exception of minority carrier concentrations. In these cases, the boundary condition is fulfilled for the first prediction of a solution. Subsequent modifications caused by δw will not change the value at the borders. Therefore, the steady-state boundary conditions for each variation obtained by solving the system in Eq.(3.37) are given by

$$\delta V(0) = \delta p(0) = \delta T_n(0) = \delta T_L(0) = 0, \quad (3.45a)$$

$$\delta V(1) = \delta n(1) = \delta T_n(1) = \delta T_L(1) = 0. \quad (3.45b)$$

The minority carrier concentration depends on the surface recombination velocity, as presented in section 2.4.2. Accordingly with Eq.(3.9), it is assumed that

$$u_n^L(0) = S_n, \quad (3.46a)$$

$$u_p^R(1) = S_p, \quad (3.46b)$$

Surface recombination velocity is expressed in non-dimensional form by $S_n \rightarrow S_n/u_0$ and $S_p \rightarrow S_p/u_0$. For electrons, the discretized variables yield

$$\left(\frac{V_1 - V_0}{\Delta x}\right) - \left(\frac{2}{n_0 + n_1}\right) \left(\frac{n_1 T_{n1} - n_0 T_{n0}}{\Delta x}\right) = S_n, \quad (3.47)$$

where the sub-indexes indicate the node number, being n_0, V_0 and T_{n0} the boundary conditions of the front surface. Therefore, boundary condition for minority electrons depends on the boundary conditions of voltage and electron temperature, namely V_P and T_{nP} , which are known. The condition given by Eq.(3.47) is linearized in accordance with Newton's method for electrons and holes. This yields the boundary conditions for δn and δp , given by

$$\delta n(0) = \frac{n_1 \delta V_1 - 2n_1 \delta T_{n1} - (S_n \Delta x - V_1 + V_P + 2T_{n1}) \delta n_1}{S_n \Delta x - V_1 + V_P - 2T_{nP}}, \quad (3.48a)$$

$$\delta p(1) = \frac{p_{Nu} \delta V_{Nu} + 2p_{Nu} \delta T_{LNu} - (S_p \Delta x / \mu + V_N - V_{Nu} - 2T_{LNu}) \delta p_{Nu}}{S_p \Delta x / \mu + V_N - V_{Nu} + 2T_{LN}}. \quad (3.48b)$$

The relations obtained above depend on the first nodes to the interior of the device in a mixed boundary condition. The way in which this is implemented is presented in more detail in Appendix B.

3.6.4 Numerical Procedure

This section describes the procedure followed in order to obtain the solution to the system in Eqs.(3.2) at a given operating point. The main values that need to be defined at the initialization are the following:

- Applied Voltage, V_{app} .
- Cell thickness, L .
- Junction depth, x_J .
- Doping concentrations, N_A and N_D .
- Number of mesh points, N_u .
- Equivalent sun intensity.
- Average starting temperature.

These are the main parameters that may need to be modified in order to analyze several cases of study. Knowing the number of discrete points for the finite difference method, the mesh is established for $N_u + 1$ equally spaced intervals defined at Eq.(3.39).

Many of the properties that are used to obtain the non-dimensional version of the equations are dependent of the lattice temperature. For the majority of the cases it will be assumed that the increase in lattice temperature is small and, therefore, temperature dependent properties do not change considerably. Thus, the temperature at which properties are evaluated is

$$T_l = \frac{T_L(0) + T_L(L)}{2}. \quad (3.49)$$

With the main transport parameters, the value of the non-dimensional groups are obtained. Having these values it can be verified if the conditions of the problem are suitable for the approximations described above. Mainly, it is verified if $\varepsilon_n \ll 1$ and $\nu_n \ll 1$. If the asymptotic simplifications can be used, the values for the non-dimensional groups are obtained.

Having scaled the variables, the non-dimensional version of the generation profile is obtained according to Eq.(2.122). The non-dimensional boundary conditions are also defined with the exception of the minority carriers. If the neutral zones of the device are larger than the corresponding depleted layer, $w_n < l_n$ and $w_p < l_p$. Then, the depletion region approximation can be used; an electric potential profile $V(x)$ is obtained according to Eq.(2.148), defined as V_{DRA} . It is then straightforward to solve continuity equations for each carrier from Eqs.(3.29a) and (3.29b), using the DD expression for the currents in Eqs.(3.31), with the voltage as a known variable. This delivers a first approximation for the carrier concentration profiles n_{DRA} and p_{DRA} for electrons and holes respectively.

Temperature profiles for the first iteration, T_n^0 and T_L^0 , are assumed to be linear with respect to the boundary conditions which, along with the results from the DRA, constitute the initial iteration w^0 . This allows to start the iterations by solving the system given by Eq.(3.37) until δw^j becomes small enough, evaluated by the norm $|\delta w^j|$ and a minimum error er_m . In order to ensure the convergence into a solution, a numerical relaxation parameter θ is introduced, which weighs the value of the next iteration. A description of this procedure is presented in a diagram in Fig. 3.2.

The methodology followed in order to achieve the goals of the present study was presented in Chapter 3. A general characterization of the problem to be solved was detailed in section 4.2. A particular case of a hydrodynamic model fit for semiconductor simulation is presented in section 3.2, along with the boundary conditions in section 3.3. The non-dimensional version

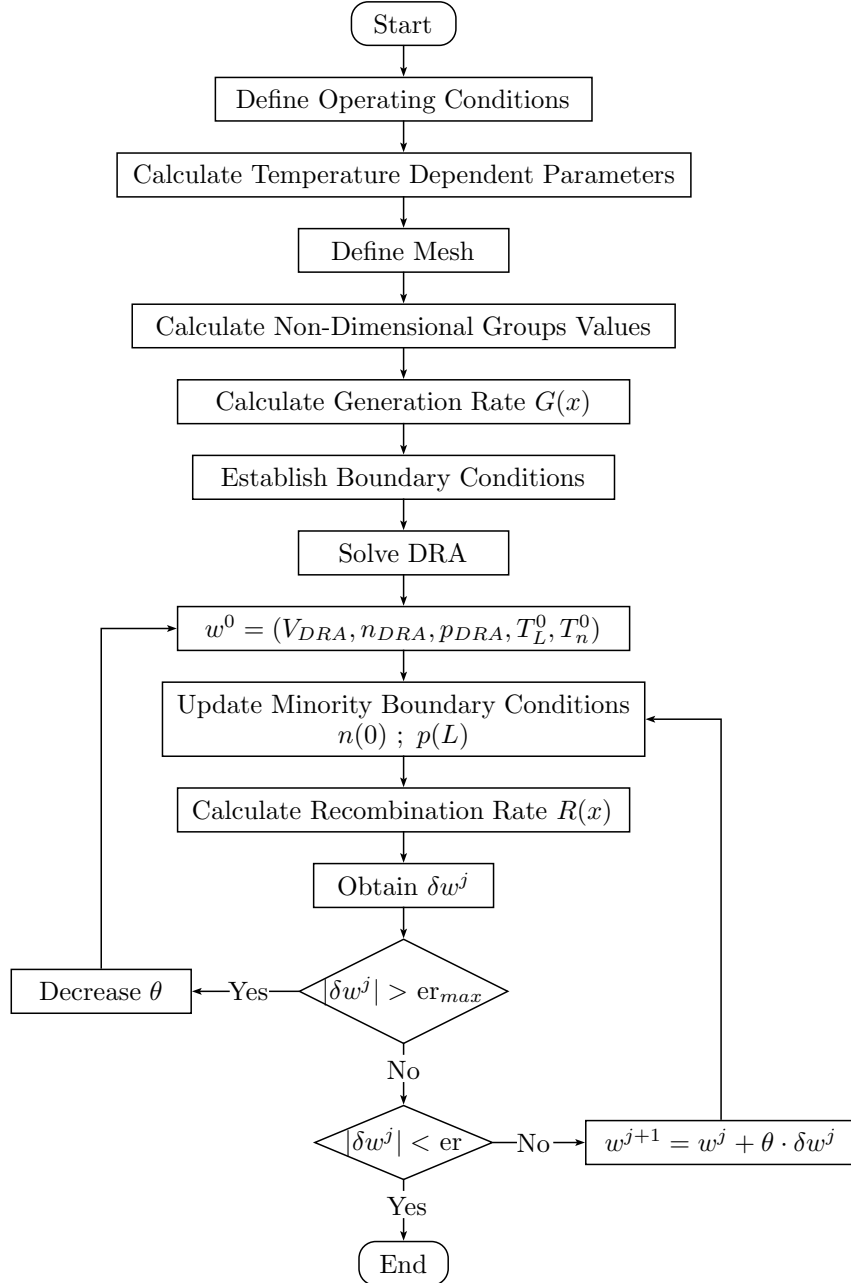


Figure 3.2: Numerical procedure diagram.

of the involved variables is explained and applied to this example of the HD model in section 3.4. With the use of this scaled version of the equations, flow parameters are analysed in section 3.5 in order to deliver an asymptotic approximation of the model, which simplifies several non-linearities. Finally, a brief description of the main features of the numerical method used to solve the model is presented in section 3.6. The results of applying this methodology are presented and analysed in the following chapter.

Chapter 4

Results

4.1 Numerical Verification of the Results

In order to draw conclusions from the numerical solutions of the model, it is necessary to get reliable results. To verify this, some simple example cases are solved, examining the accuracy and convergence of the numerical scheme. There are several variables that describe the solution of the hydrodynamic model for a solar cell, for this particular case the model is solved for electric potential, V , carrier densities, n and p , carrier temperatures, T_n or T_p , and lattice temperature, T_L . Electric field, E , and carrier velocities, u_n and u_p , are some variables which can be derived from the previous ones. In this section, these variables are only analysed from a numerical perspective, leaving the physical analysis for Section 4.2. The first case to be solved uses the asymptotic approximation presented in Section 3.5 and does not consider high field effects, therefore $\varphi_m = \varphi_k = \varphi_e = 1$. The energy balance is much simpler than the one presented in Eq. (3.30b), and is given by

$$\frac{1}{n} \frac{\partial}{\partial x} \left(T_n n \frac{\partial T_n}{\partial x} \right) - \frac{\nu_n}{\varepsilon_n} (T_n - T_L) + \frac{2}{3} u_n^2 = 0. \quad (4.1)$$

In this case, energy flux $n\mathbf{S}_n$ is represented using only Fourier's law, since no high energy phenomena needs to be modeled. Thermal conductivity is given by Wiedemann-Franz law. This model gives an insight of how the variables behave under normal operating conditions in order to make a comparison and understand the effect of high energy carriers.

As a first exercise, Newton's method is applied using a constant numerical relaxation parameter θ . Boundary conditions are linearized as described in Section 3.6. Light is assumed to enter the device through the p -side ($x = 0$), and its intensity measured in number of Suns. 1 Sun is equivalent to the *AM1.5* spectrum which is weighed in proportion for each wavelength in case of being different than unity. Only SRH recombination is considered in this case. Boundary conditions for each temperature are equal and equivalent to T_l , Eq.(3.49), the value at which temperature dependent properties are evaluated. The main physical and numerical parameters that characterize this example are summarized in Table 4.1.

Transport properties are calculated according with what was presented in Section 2.3, with the parameters in Table 4.1. These depend mainly on the bulk temperature $T_L(x)$, assumed

Table 4.1: Parameters used to solve case 1.

Parameter	Value	Units
N_A, N_D	10^{21}	$[m^{-3}]$
L	4	$[\mu m]$
x_J	$0.5L$	$[\mu m]$
V_{app}	0.5	[V]
T_i	300	[K]
#Suns	1	–
θ	0.1	–
N_u	2000	–
er	10^{-8}	–

constant and equal to T_i ; and on the doping values of each side of the junction, N_A and N_D . The transport and material properties obtained for this case are presented in Table 4.2 and 4.3. Energy relaxation time for holes is not presented given that for this example only the contribution of electrons is considered for heating effects.

Table 4.2: Transport properties for the device in case 1.

Property	Electrons (n)	Holes (p)	Units
$m_{n(p)}/m_0$	0.0634	0.49	–
$\tau_{m,n(p)}$	2.86×10^{-13}	1.2×10^{-13}	[s]
$\tau_{n(p)}$	2.8×10^{-9}	8×10^{-9}	[s]
$\tau_{\epsilon,n}$	5.72×10^{-13}	–	[s]
$S_{n(p)}$	–10	100	$[m/s]$

Table 4.3: Material properties for the device in case 1.

Property	Value	Units
k_L	46	$[W/m^2K]$
E_g	1.424	[eV]
V_{bi}	1.036	[V]

These properties in turn deliver the value of the non-dimensional groups associated with the hydrodynamic model, which are presented in Table 4.4. It can be seen how the condition $\epsilon_n \ll 1$ is fulfilled. Therefore, the use of the hydrodynamic model is appropriate. However, ν_n and ν_p are not negligible compared to 1. This is an important factor to take into consideration for the physical interpretation of the results in this thesis. Nevertheless, since the present section considers only the numerical perspective, these parameters are used.

Table 4.4: Non-dimensional groups values for case 1.

ND Group	Value
λ	3.4×10^{-2}
ε_n	3.7×10^{-4}
ν_n	0.5
ν_p	0.12
m_r	0.129
γ	2.383
ψ	59.5

Using these parameters, several results were obtained for different numbers of grid points N_u . Figure 4.1 shows the results for different convergence steps in Newton's method using $N_u = 2000$. First row presents electron and hole densities along with electric potential profile, while the second row shows electron and hole velocities and the electric field, which are not a direct solution of the model, but they are derived from the latter variables. Last two graphs correspond to electron and lattice temperature increases across the device. The initial iteration step, corresponding to $k = 0$, is shown in all of the graphs in the figure with the green dotted curve. The red dashed curves show an intermediate iterative step, arbitrarily selected to be $k = 10$, in order to show the evolution as the method converges. Similarly, the blue solid curves present the final iteration when δw is lower than the established error tolerance. The total number of iterations was 205 for this particular case and number of grid points. The number of iterations is reduced significantly if a relaxation parameter θ closer to one is used after each iteration, but in order to study the behavior of the convergence, a fixed parameter is used.

The initial condition is calculated starting from the DRA, as explained in Section 3.6. Electrostatic potential is taken as an input in order to solve decoupled transport equations for electrons and holes. This delivers initial conditions for $V(x)$, $n(x)$ and $p(x)$, with the corresponding values for $u_n(x)$, $u_p(x)$ and $E(x)$, while temperature profiles $T_n(x)$ and $T_L(x)$ are simply assumed linear with respect to their boundary conditions.

As described in Section 4.2, because of the operation regimes of solar cells, voltage profile across the cell is expected to behave similarly under different operating conditions, therefore DRA will deliver a good initial approximation for $V(x)$ in most cases. From the figure, it can be clearly noticed how the initial conditions for carrier densities calculated from the DRA also give a very valid approximation. However, temperature profiles, specially electron temperature, have important variations from spatial thermal equilibrium. Nonetheless, the major variations in carriers densities and velocities coincide with the biggest changes in temperature levels. This occurs mainly because solving out of thermal equilibrium provides additional information which has a counter effect in the rest of the variables in order to maintain the balance in energy flows. Regardless of this, the solved example is a simple case and using lower order approximations should provide good results.

It can also be noticed how lattice temperature surpasses the final curve at the intermediate

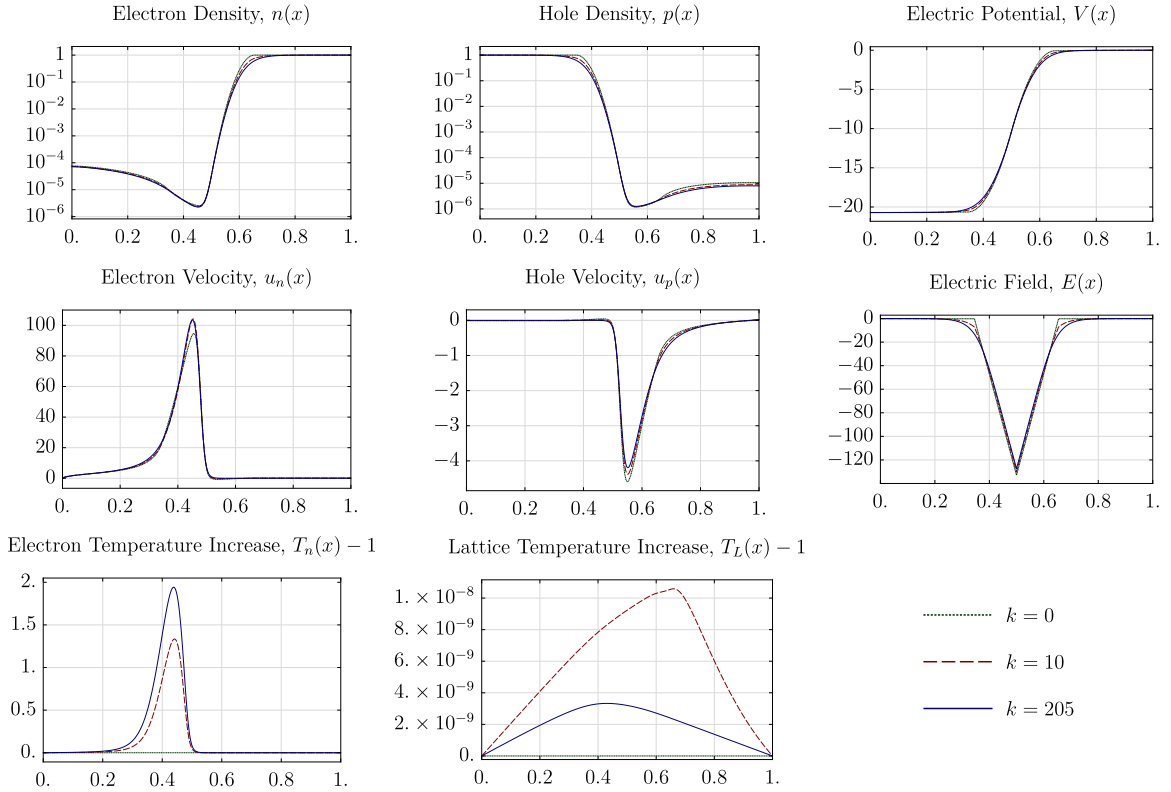


Figure 4.1: Different convergence steps towards of Newton's method for the solution of the HD model in case 1, using $N_u = 2000$.

iteration step, while the other variables tend gradually to the final solution. Numerical phenomena like these are expected given the oscillatory nature of Newton's method when reaching convergence. In fact, when reaching convergence all variables will fluctuate near a solution value until these fluctuations are considered small enough, this is only more noticeable in this case. When these deviations from the solution are too large, they can cause the method to become unstable. This is why it is important to use a good initial approximation or advance gradually enough towards the solution, which is accomplished through the relaxation parameter θ .

Numerically, the allowed error tolerance is only one factor to take into consideration. The use of different grid points number leads to problems in convergence since spatial gradients may be too big for a given variable. Special care needs to be taken for example for carrier densities, which in this example vary between magnitudes of $\sim 10^{16}$ to $\sim 10^{22}[m^{-3}]$ abruptly within the space charge region, that has a width of the order of $1 \mu m$. This means several orders of magnitude in a very short distance. Figure 4.2 presents the solution of the HD model in Case 1 for different numbers of mesh grid. Results for $N_u = 100, 500$ and 10000 are presented.

Due to the parameters used for case 1, there are no significant gradients, compared to what is observed using parameters of a real solar cell. This is why even a relatively coarse grid delivers valid results. Evidently, the variable that presents the most negligible differences is electrostatic potential. This corroborates the fact that voltage will present a similar shape

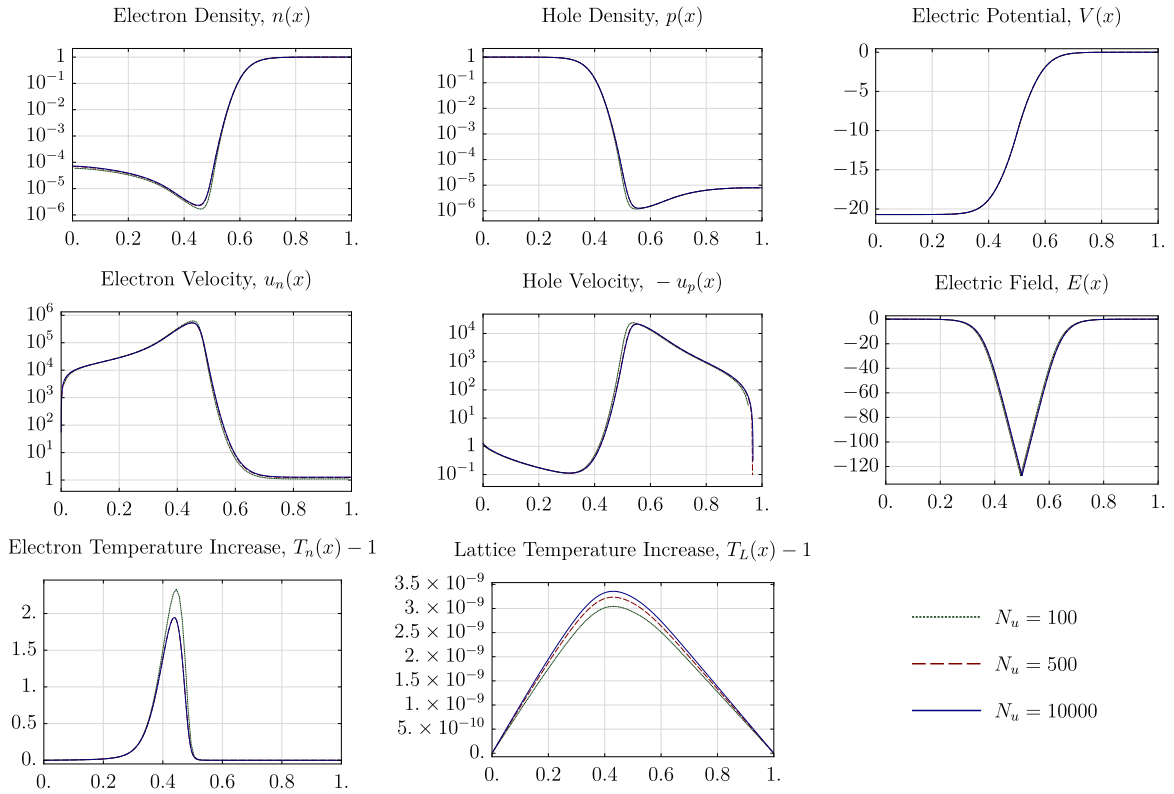


Figure 4.2: Solution of the HD model in case 1 for different mesh grid numbers, $N_u = 100, 500$ and 10000 .

in most cases, since rather small changes in carrier densities do not transmit important differences in voltage via Poisson's equation. Additionally, because of the smooth shape of voltage profile and its small gradients, a coarse mesh is sufficient to accurately represent its behavior. For the rest of the variables, the most noticeable difference can clearly be observed between $N_u = 100$ and 500 , while using $N_u = 10000$ produces virtually the same results. Since current needs to be conserved across the device, changes in carrier velocities will have a compensating effect in the corresponding carrier density as well as temperature. The more graphically noticeable differences when using $N_u = 10000$ can be observed in lattice temperature. This is explained because of the magnitude of changes in the specific variable. If these variations are compared in magnitude to those of other variables, the changes are much smaller. Even in this simple example there are zones where a coarse grid would be sufficient, given the practically null gradients. Because of this, developing a code where refining in specific areas is possible would be extremely useful in order to save memory and iteration time.

Using $N_u = 10000$ as an 'exact' solution, the convergence of each independent variable is studied. The norms L^∞ and L^1 are calculated from the difference of several grid numbers with this target solution. The results are shown in Figures 4.3 and 4.4, respectively. Norm L^∞ clearly presents a tendency to lower errors as the mesh is finer, which was expected, while L^1 shows less decaying behavior. This effect is explained because the norm L^1 corresponds to the total sum of all the deviations from the target solution, therefore, the unit of space needs to be taken into account. In both figures the values of $\|T_L\|_\infty$ are amplified in order

to better fit the orders of magnitude of the rest of the variables.

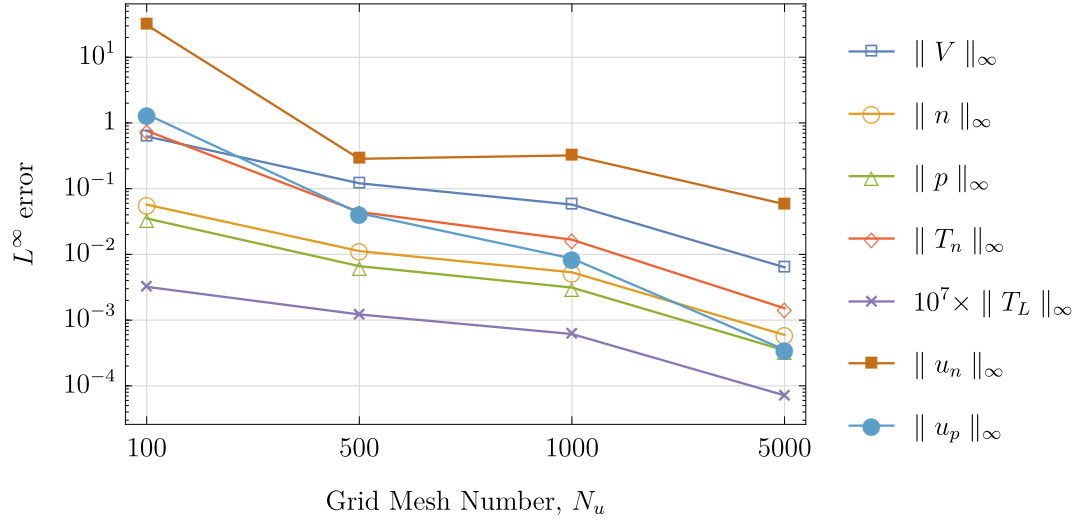


Figure 4.3: Convergence of each variable using the norm L^∞ .

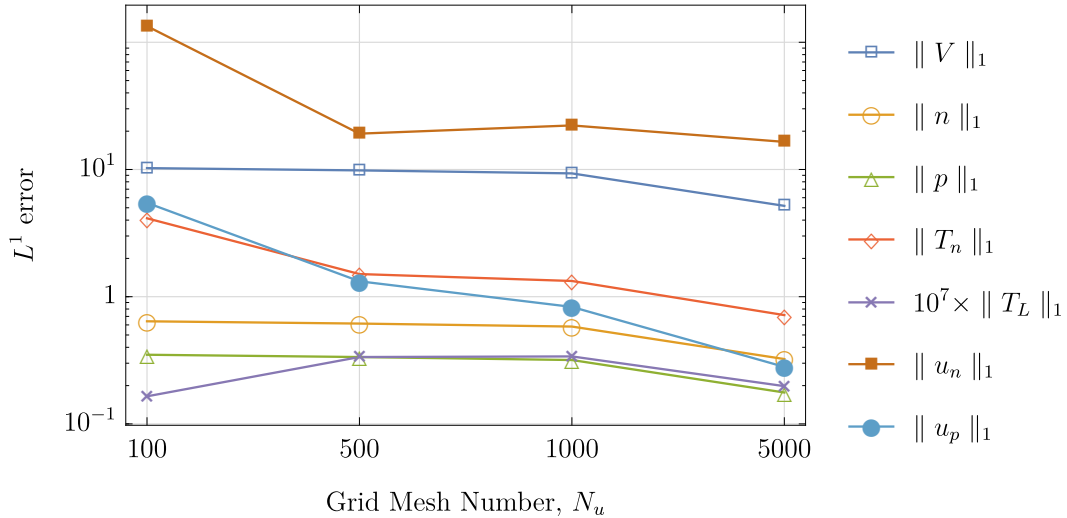


Figure 4.4: Convergence of each variable using the norm L^1 .

The norm L^∞ corresponds to the value of the maximum difference with respect to the target solution, therefore, the location of this error can be found. These locations are listed in Table 4.5 for the different grid numbers used. The non-dimensional value of x is presented.

As expected, the location of the L^∞ norm coincides with the highest gradients, or peaks of each variable, which are the regions where the method is less accurate. In this manner, the maximum error of the electric field always matches the junction depth x_j . For carrier densities, the most troubling areas for the convergence are when reaching the corresponding majority quasi neutral regions. This occurs because the biggest gradients are located in these areas as well. The maximum error for both velocities match their respective peak near the

Table 4.5: Non-dimensional location of the L^∞ norm.

Grid Number	Norm Location x						
	$\ V\ _\infty$	$\ n\ _\infty$	$\ p\ _\infty$	$\ T_n\ _\infty$	$\ T_L\ _\infty$	$\ u_n\ _\infty$	$\ u_p\ _\infty$
100	0.5	0.64	0.37	0.47	0.38	0.47	0.53
500	0.5	0.636	0.372	0.474	0.412	0.446	0.53
1000	0.5	0.635	0.372	0.475	0.413	0.478	0.53
5000	0.5	0.635	0.371	0.476	0.414	0.476	0.60

junction, slightly deviated towards the p -side for electrons and to the n -side for holes, while temperatures show the maximum value of error at their corresponding peak. Solving for cases with more abrupt gradients, whether it is because of higher doping levels or longer devices, generates the need for finer meshes in order to avoid numerical issues in the junction area such as smearing of the results or numerical viscosity effects [45].

Even though numerical differences seem to be of small order for each independent variable, there are areas where small changes have a major impact in the total current. This is the case for electron densities, where even though the biggest changes are noticeable at the majority regions, minority carrier densities are the ones that have a greater impact. For this reason, it is interesting to analyze the relative error rather than the absolute.

It can be seen how for low density meshes both velocities are the ones with a higher error. Particularly, the error for u_n is the highest in all cases. This is related to the fact that velocities are calculated from the gradients of the variables obtained as a result of the method. Therefore, the difference in precision of the results using a finer grid is amplified when calculating the respective gradients. This is directly related to the error when calculating the value of the total current, which is arguably the most important output of device simulation. Electric currents are comprised by the movement of carriers due to drift, diffusion and thermal diffusion, all originated from significant gradients which tend to compensate. Numerically, this means that gradients of high value add up to a value of current which is orders of magnitude smaller. Therefore, even though convergence is achieved, changes in current may not be negligible. This effect can be seen in Fig.4.5, where clearly changes in current are considerable compared to those in the rest of the variables at the same number of grid points.

Some numerical issues arise independently of the mesh grid number that is used. For instance, maintaining all other parameters, there is a critical length at which the boundary conditions for minority carriers density, in this case holes, become unstable. In order to exemplify this issue, the same parameters are used changing only the total length of the device. In this case to $L = 13 \mu m$, a length at which this instability occurs. This problem is depicted more clearly when solving a case ‘in the dark’, given that these instabilities occur at the same length independently of the number of grid points and whether or not photogeneration is present. Under no illumination conditions and forward bias, carriers move opposite to what occurs under light, and their densities at the boundaries of the SCR are defined approximately by the equilibrium minority density under an applied voltage. For holes, this will be defined as

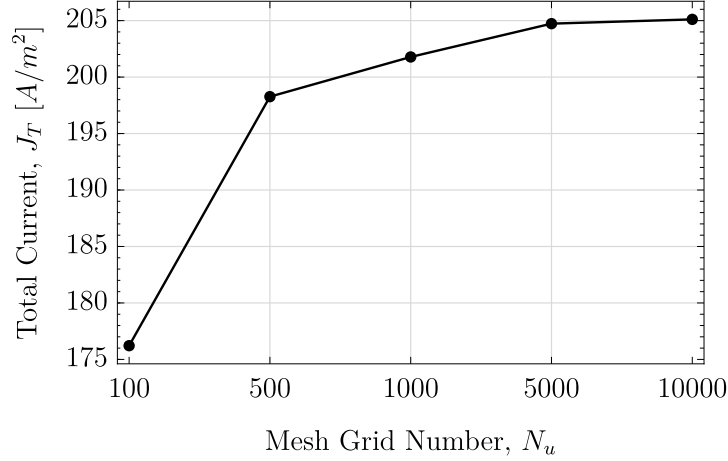


Figure 4.5: Value of the total current J_T for different mesh grid numbers.

p_n , given by

$$p_n = p_0 \exp\left(\frac{eV_{\text{app}}}{k_B T_L}\right). \quad (4.2)$$

The expression for electrons is analogous. Moving from the boundary of the depleted region towards the contacts, the density of each carrier decreases due to recombination, reaching a boundary condition that needs to fulfill the relations for surface recombination velocities. In this case, the boundary condition is expected to reach a density value above p_0 and below p_n ; this will be fulfilled regardless of the approximation that is used to solve for density.

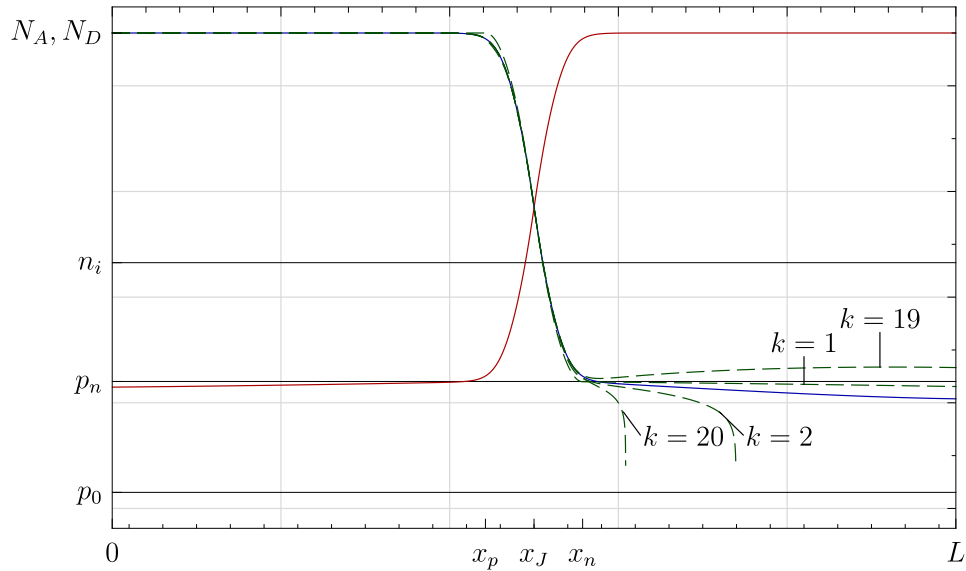


Figure 4.6: Effect of using a high relaxation parameter θ .

Figure 4.6 shows several results for carrier densities for a solar cell in the dark, under a forward applied voltage. The red solid curve presents the result for electron density, while the blue

solid curve shows the solution for holes, both using $\theta = 0.3$, and the green dashed curves correspond to several iteration steps, k , using $\theta = 1$. The densities equivalent to the doping levels N_A and N_D , intrinsic density n_i , thermal equilibrium density p_0 and hole equilibrium minority density under an applied voltage p_n are also shown in the graph. The first iteration $k = 1$ is calculated from the DRA, and it is clearly noticed how it is not far from the real solution. However, the calculation of $k = 2$ over compensates this difference and moves towards a negative density value which, nonetheless, also fulfills the surface recombination velocity condition. Subsequent iterations add up to increase this difference, and diverge instead of converging towards the solution, as can be seen in Fig. 4.7 where 20 iteration steps are shown for both values of θ .

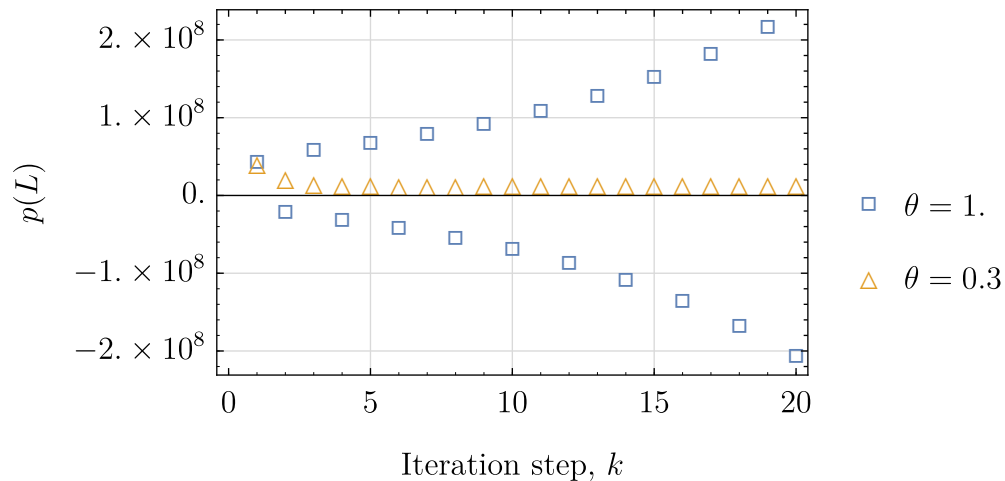


Figure 4.7: Minority boundary condition for hole density after several iteration steps, using two values of θ .

Even if a small parameter is used at first, returning to a higher value of θ makes the boundary condition unstable, therefore special care needs to be taken in order to achieve real convergence given that the error criteria can be satisfied for a density value different to the steady state solution. Because of these issues, some adjustments were made. First, a condition for θ was established which verifies if any density value is negative, and imposes a smaller value of θ if this is true. Second, the error criteria is defined according to the relative error, rather than the absolute. Finally, the maximum variation of electron temperature with respect to the former step, given by δT_n , was limited using a special relaxation parameter θ_T . This avoids abrupt changes in electron temperature, which as a consequence leads to a sudden decrease in electron density, sometimes reaching negative values, and produce the method to diverge. This relaxation parameter works only if the next step is predicted to vary more than 50%, and therefore it is given by

$$\theta_T = \frac{0.5}{\theta \|\delta T_n / T_n\|_\infty}, \quad (4.3)$$

if $\theta \|\delta T_n / T_n\|_\infty$ is higher than 0.5, and equal to 1 otherwise. Although this additional factor aids into the convergence of the method, does not provide a real solution to the cause of the stability problem. This arises from the fact that the movement direction of carriers changes over a small region near the surface, because of the surface recombination. The implemen-

tation of an upwind should help to avoid this numerical issue by changing the discretization scheme depending on the sign of carrier velocities. Therefore, the implementation of this, or a similar method, is fundamental for the robustness of the numerical scheme.

4.2 HD modeling of a single junction solar cell

In the present section, a brief description and discussion of the physical aspects of the results is presented. This general analysis of the variables involved is performed because under normal operating conditions they have a usual behaviour, which has been thoroughly studied and represented in analytical models such as the DRA. However, subtle differences in these results may generate important variations in output current or thermal behaviour. Furthermore, one of the objectives of this study is to analyse the behaviour of a solar cell under specific design or operating conditions, where high energy phenomena are present and their effects are not negligible. The equations and conditions to be solved are identical to the ones presented in Section 4.1.

Figure 4.8 shows the solution for the hydrodynamic model, given the conditions established in Table 4.1. All the results in this section are presented in non-dimensional form. Therefore, each variable is scaled by its corresponding factor as defined in Section 3.4. These factors depend on properties such as relaxation times or effective mass, which in turn depend on parameters such as the length of the device or the applied voltage. Therefore, different operating conditions will deliver different scaling factors. Distance (x), doping densities (n, p), and temperatures (T_n, T_L) are scaled directly by using the values for the length of the device L , minimum between the doping densities N_A or N_D (which in this case are equal), and the boundary condition for lattice temperature T_l , respectively. Under these conditions the scaling factors for the rest of the variables are given by $U_T = 0.026$ V for voltage, $U_T/L = 6465.4$ V/m for electric field and $u_0 = 5121.4$ m/s for carrier velocities.

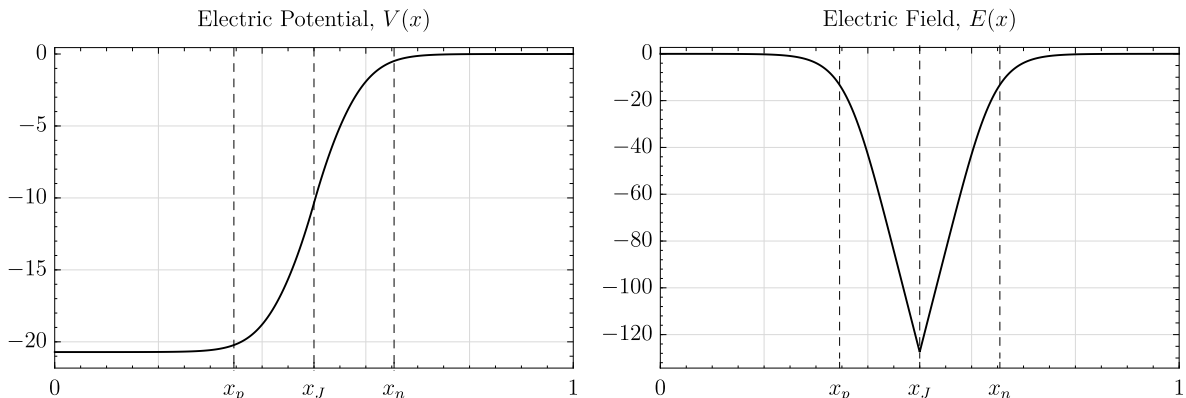


Figure 4.8a: Solution plots of the hydrodynamic model for case 1. Results of electric potential and field.

Using the depletion approximation, the depleted layer has a defined length given by Eq. (2.147). In this case equal to $1.24 \mu\text{m}$, corresponding to nearly 30% of the total length, which agrees with what is shown in the figures. These regions are defined by the dashed lines

on each graph, as a reference in order to explain the results. The ‘ p ’ quasi-neutral region is located between 0 and x_p ; the ‘ p ’ side of the SCR, with a length of w_p , between x_p and x_J ; the ‘ n ’ side of the SCR, with a length of w_n , between x_J and x_n ; and the ‘ n ’ quasi-neutral region between x_n and the total length of the device L , or 1 in the non-dimensional version. In this case both regions have equal lengths, since the doping levels are equal.

The open circuit voltage, V_{oc} of any regular solar cell is located below the built-in voltage, V_{bi} . Consequently, the Maximum Power Point (MPP) of operation will also be lower than V_{bi} . This means that under normal operating conditions the potential barrier set up by this voltage is not surpassed and the electric potential and field curves will depict a behavior as shown in Fig. 4.8a. The graphic on the left shows the electric field, where three zones can be clearly distinguished. The areas near the boundaries, in this case the contacts of the device, present a constant value of voltage which implies a zero net electric field. These are the areas outside of the SCR, which are referred to as quasi-neutral zones. In contrast, within the SCR a variation of voltage equivalent to $|V_{bi} - V_{app}|$ is developed. This voltage is originated from the diffusion of carriers at each side at the formation of the junction, and is increased or decreased by the applied voltage. For solar cells the total potential drop will always be smaller than V_{bi} . If the DRA is used, the voltage development has a parabolic shape by sections as defined in Eq.(2.148), also similar to the curve in the figure. In turn, solving the HD model delivers a less abrupt interface between one section and another, but the order of magnitude of the length and relative shape of each section is very similar. The same three zones are clearly present on the figure on the right, where there is zero electric field near the edges, and the voltage drop at the SCR causes a peak in the electric field, which makes the SCR the most active region of the device.

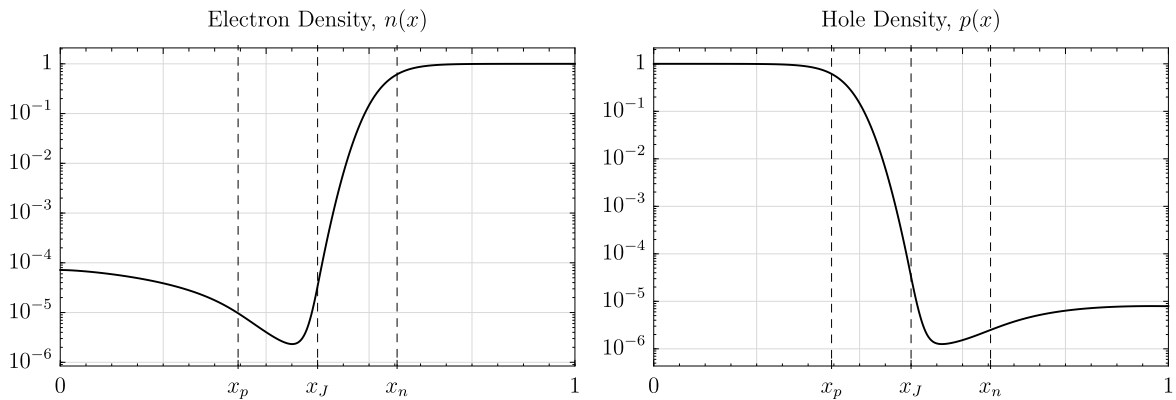


Figure 4.8b: Solution plots of the hydrodynamic model for case 1. Results of carrier densities for electrons (left) and holes (right).

Figure 4.8b shows the carrier density distribution across the device $n(x)$ and $p(x)$, while Fig. 4.8c presents carrier velocities $u_n(x)$ and $u_p(x)$, both in logarithmic scale. It has to be kept in mind that the variables are plotted non-dimensionally, which is why the maximum value of both carrier densities is 1, given that the device is symmetrically doped.

When the solar cell is under illumination, electron hole-pairs are generated across the whole depth of the device. This generates a difference in carrier density which is specially noticeable at the minority regions. This excess of carriers is transported across the device towards the

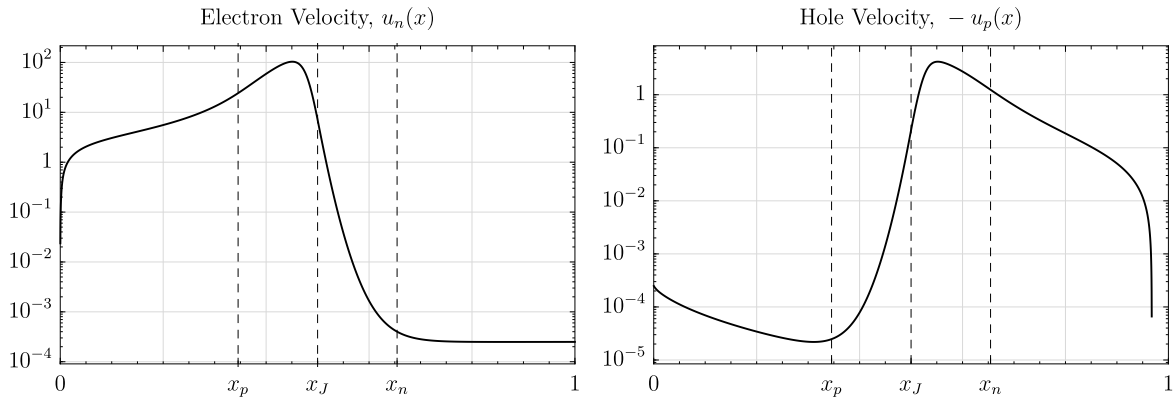


Figure 4.8c: Solution plots of the hydrodynamic model for case 1. Results of carrier velocities for electrons (left) and holes (right).

contacts. Therefore, both minority carriers move toward the junction, as can be seen in Fig.4.8c, where electron velocity is mainly positive, while hole velocity is negative. A small inversion in velocities occurs at the minority surfaces of the device caused by the surface recombination. This makes carrier velocity at these boundaries to rapidly decrease, reaching the corresponding values for surface recombination velocities. Therefore, $u_n(x=0) = S_n$ and $u_p(x=1) = S_p$. This ‘leakage’ of carriers implies a decrease in carrier density within this small section, and although it is imperceptible in the graphics, small variations in minority carrier densities at the boundaries can cause important changes in the attainable current from the device.

As carriers move through their respective minority region they suffer recombination, which is why a decrease in density can be noticed as the SCR is approached. Once the carriers enter the zone with a high electric field, they accelerate and gain their maximum velocity. This causes carriers to be absorbed faster and, as a result, a decrease in the density occurs. Peak velocity is therefore coincident with carrier density minimum. This minimum is located at the left side of the junction for electrons and at the right side for holes, *i.e.* at the minority side of the junction for each carrier.

When carriers reach the respective majority side of the junction they are collected almost instantly. For that reason, carriers generated within the junction have a very high probability of contributing into conduction. As carriers move through their respective majority region of the SCR, density increases in several orders of magnitude until reaching the doping density level. Evidently, velocity is decreased because of the higher number of carrier allowing conduction. In this particular case hole velocity has a steady increase as carriers approach the front surface. This is originated by the exponential decrease of pairs being generated as light penetrates into the device, creating the need for transport of holes to be accelerated near the contact in order to maintain balance.

The main heat sources and sinks in the lattice for solar cells are thermalisation, Joule effect, recombination processes, sub-bandgap losses, thermoelectric effects (Seebeck, Peltier and Thomson), radiation and convection with the surroundings. A thorough analysis of heat generation in Silicon solar cells considering most of these factors is performed by Couderc *et al.* [69]. Nonetheless, during their analysis they only solve transport equations for minority

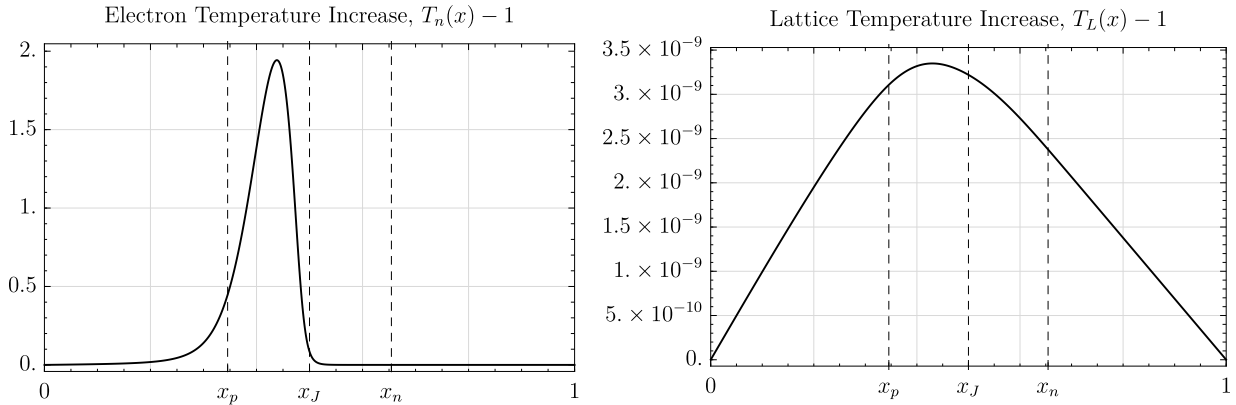


Figure 4.8d: Solution plots of the hydrodynamic model for case 1. Results of electron temperature increase (left) and lattice temperature increase (right).

carriers sections, adding these heat phenomena directly into the lattice heat balance equation. Hydrodynamic models are able to reproduce all of these heating effects, as discussed in Section 2.2, depending on the different terms included in the balance equations. An analysis of the contribution of these factors, some of which are often simplified, is included in this Thesis. However, neither radiation nor convection with the surroundings were directly included. Peltier effect is also an important source of heating in solar cells which is originated at the metal-semiconductor interface of the contacts. This phenomenon is not directly modeled in this work.

Figure 4.8d presents the non-dimensional increment of electron and lattice temperatures, $T_n(x) - 1$ and $T_L(x) - 1$ respectively, which are the result of the corresponding energy balance equations. It can be seen how lattice temperature is approximately constant across the device, with a peak reaching barely 0.01% of the boundary condition temperature. This fact was expected since no high field effects are considered and this case could be solved by simpler models delivering similar results. Furthermore, no heat is transferred from recombination nor sub-bandgap losses.

A lattice temperature profile with higher gradients would mean that properties such as bandgap, mobility, effective masses, thermal conductivity among others, would change their value in a more considerable manner. This complicates the thermal analysis since the devices exhibit a dynamic behavior regarding heating, opposite to the classical approach of considering them as a bulk material with a thermal conductivity depending on a constant lattice temperature. Zhang *et al.* [70] studied the effect of the junction temperature in the thermal resistance of the solar cell, using empirical relations developed by Huang *et al.* [71], to measure its junction temperature from the external temperature. They showed that there were important differences in thermal resistance under dark and illuminating conditions.

In contrast to lattice, the peak for carrier temperature reaches almost 200% of the original lattice temperature. This maximum clearly matches electron velocity peak, since electrons are the main contributor into heating for this case. In fact, it is well known that the heating of solid state devices, and solar cells in particular, is originated at the interfaces of junctions and contacts. The shape of this peak also originates from the expression for thermal conductivity

κ_n , which is highly dependent on carrier density, mobility and carrier temperature all of which have their higher gradients within the SCR. It can be seen how carrier temperature peak is restricted within the surroundings of the junction. Therefore, the term $\partial T_n / \partial x$ is not considerable near the boundaries which is where it would affect the total current.

However, some new technologies such as thin film solar cells present degradation or failures due to hot spot formation and thermal runaway. This may be related with the fact that the junction and, therefore, the internal hot spot, as the one shown in Fig. 4.8d, is closer to the surface. Hot spots of 300 [K] above the surrounding area have been reported [72]. The stability of hot spots has been studied by different approaches, but mainly through variations of the diode equation, coupled with thermal models for the lattice [73, 74].

Nevertheless, all of these studies have the limitation of not knowing the internal temperature profile of the cell with certainty, given that it is extremely hard to measure. A deeper investigation on the effects of the dynamics between carriers and lattice out of thermal equilibrium and their respective conditions at the boundaries, could lead to a better understanding of the causes and possible solutions for thermal issues in solar cells.

4.3 Effect of Hot-Carriers at the Contacts of a PN Junction Solar Cell

As a first set of results, the carrier temperature dependence at the boundary of the device was studied, in order to show the influence of carriers and lattice temperatures in the electrical performance of a GaAs PN junction solar cell. These were obtained during the course of the development of this thesis, in order to be presented at the XIV Pan-American Congress of Applied Mechanics, and were later published in the journal *Acta Mechanica* under the title *Hydrodynamic modeling of hot-carrier effects in a PN junction solar cell* [75]. For this reason, there were several assumptions and solution methods that were later modified. The main difference with what was presented at Chapter 3 is the use of a constant thermal conductivity for electrons κ_n , which leads to important differences in the non dimensional version of the equations. Another significant difference is the use of hole temperature at thermal equilibrium with electron temperature $T_p = T_n = T_c$. This assumption is revised in Section 4.4, for its use in further results. Perturbations method in asymptotic expansions was used in order to reduce the non-linearities of the equations, and only the zero order was solved as sufficient approximation of the solution. Aside from these facts, the model and method of solution are very much alike to the rest of the results of this thesis, and describe similar physics. The rest of the differences, along with the limitations and consequences of these assumptions are discussed at the end of this section.

The physical parameters used for this case are summarized in Table 4.6. A depth dependent generation rate was used in accordance to what is presented in Section 2.4.1. It was assumed for this case that the cell was under 1 Sun of illumination, with the AM1.5 spectrum. Even though the use of a constant thermal conductivity makes the calculations much simpler, there are not many references for values of κ_n . However, it is known that its value is much lower

than lattice thermal conductivity. Therefore, a small arbitrary value was used.

Table 4.6: Relevant parameters and properties for Case 2.

Parameter	Value	Units
N_A	10^{23}	$[m^{-3}]$
N_D	10^{22}	$[m^{-3}]$
L	10	$[\mu m]$
x_J/L	0.1	–
T_l	300	$[K]$
#Suns	1	–
κ_n	3	$[Wm^{-1}K^{-1}]$

Three different voltages (V_{app}) were applied on the illuminated cell using these parameters, 0.4, 0.6 and 0.8 V. Results are shown in Figs.4.9 for voltage, electric field, electron density, hole density, electron velocity, hole velocity, carrier temperature and lattice temperature, respectively. From these figures, voltage, electron density and hole density vary smoothly in space for the three applied bias, and depict a behavior similar to the one described in Section 4.2. Electron and hole velocities, shown in Figs. 4.9e and 4.9f, also present the expected peak near the junction, slightly shifted towards the respective minority side. It can be noticed that both velocities increase with decreasing the voltage, which is caused by an increase in the electric field at the junction, due to a higher voltage drop. This also correlates with the peak of temperature in the same region, as can be seen in Figs.4.9g and 4.9h. Lower temperatures and velocities, meaning lower energy charge carriers at the junction while increasing the voltage, also correlate with a more efficient behavior of the cell.

Even though the increase in lattice temperature is small compared to the one shown by electron temperature, it is considerable given that only Joule effect is assumed to heat up the device. Current density in solar cells is relatively small, however, its value gets higher at the front contacts. Nonetheless, since this effect cannot be considered in the one dimensional case, Joule effect heating is small compared to other heating sources. Even though the conditions of both examples are quite different, this can be compared to the solution of Case 1, which considers Wiedemann-Franz law for electron thermal conductivity. Because of the generally higher κ_n in this case, the increase in electron temperature is much more distributed across the device. This implies that the difference $T_c - T_L$ is higher in regions where the carrier density is higher, and therefore thermalization occurs at a higher rate, heating the lattice.

Differences between lattice and carrier temperature are known to affect the performance of GaAs PN junction solar cells. As was mentioned, the performance of a solar cell under light is analyzed by imposing specific boundary conditions for T_c . Results in Figs. 4.10 and 4.11 show different curves for total current and power output densities as a function of applied voltage for different boundary values of T_c and T_L . The maximum current and power output increase when the imposed carrier temperature boundary condition increases. This can be explained by favorable conditions for hot-carrier flow, which can be physically achieved by using energy selective contacts in order to reduce the carrier cooling rate. Quantum wells,

quantum wires and quantum dots have been proposed to be used with this purpose [76]. Nonetheless, hot-carrier extraction mechanism is not considered here, and the temperature is simply imposed. This behavior is further analyzed and compared to experimental references in the following subsection.

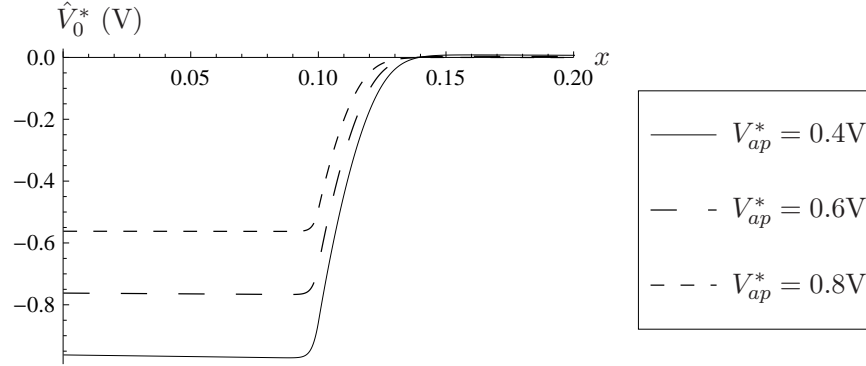


Figure 4.9a: Steady-state solution for voltage across a PN junction at different forward bias under 1 Sun of illumination and AM 1.5 spectrum.

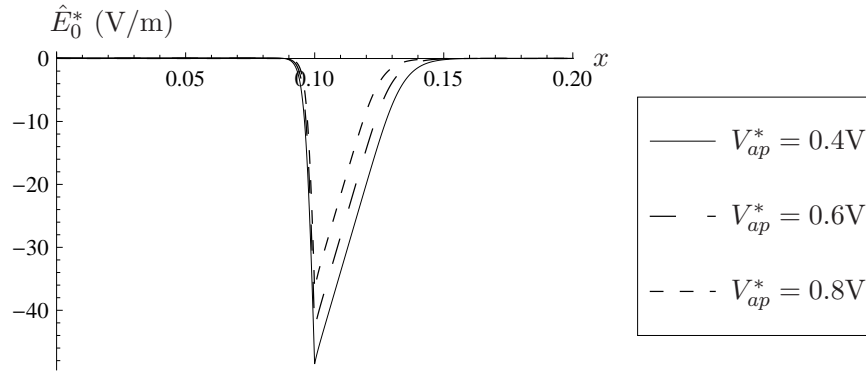


Figure 4.9b: Steady-state solution for electric field across a PN junction at different forward bias under 1 Sun of illumination and AM 1.5 spectrum.

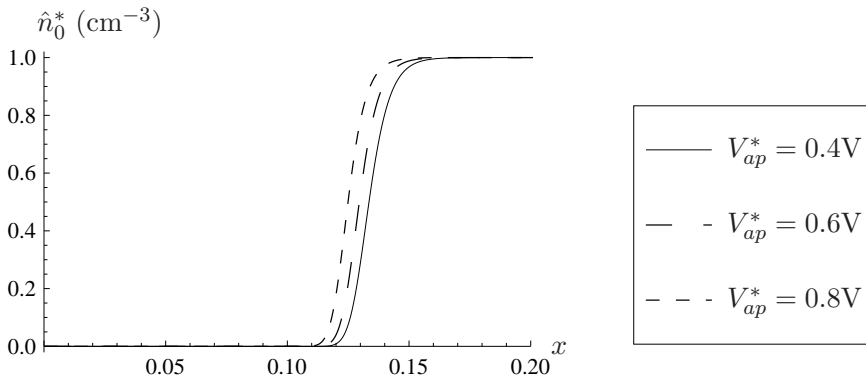


Figure 4.9c: Steady-state solution for electron density across a PN junction at different forward bias under 1 Sun of illumination and AM 1.5 spectrum.

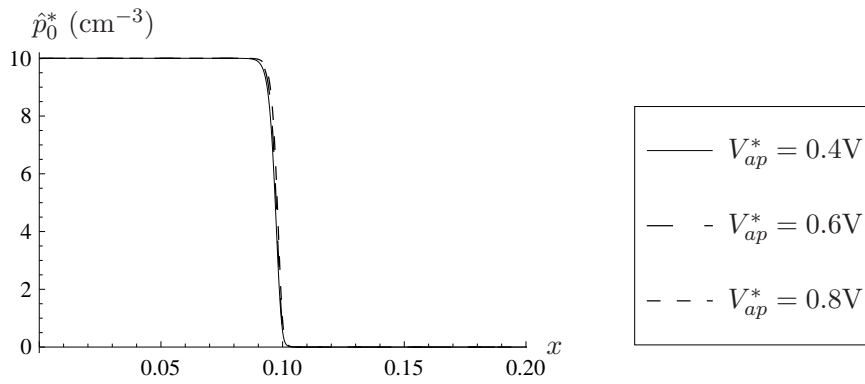


Figure 4.9d: Steady-state solution for hole density across a PN junction at different forward bias under 1 Sun of illumination and AM 1.5 spectrum.

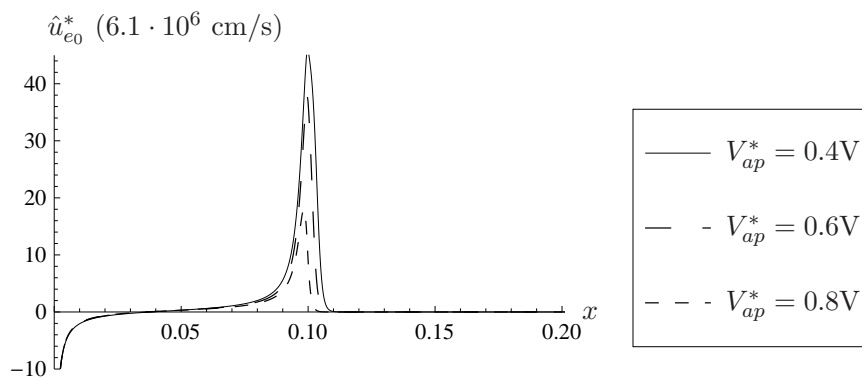


Figure 4.9e: Steady-state solution for electron velocity across a PN junction at different forward bias under 1 Sun of illumination and AM 1.5 spectrum.

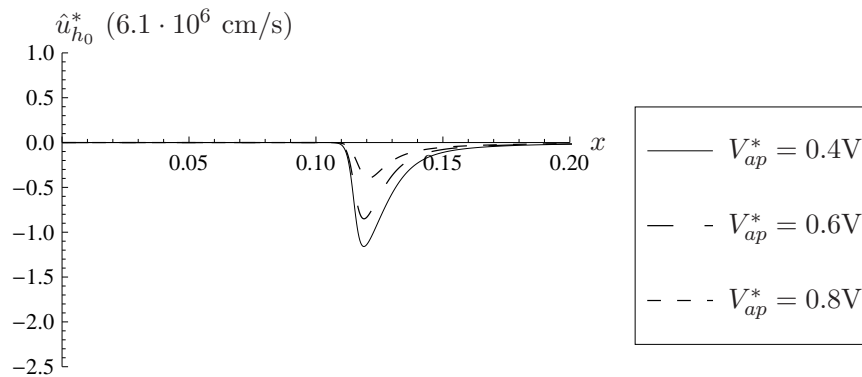


Figure 4.9f: Steady-state solution for hole velocity across a PN junction at different forward bias under 1 Sun of illumination and AM 1.5 spectrum.

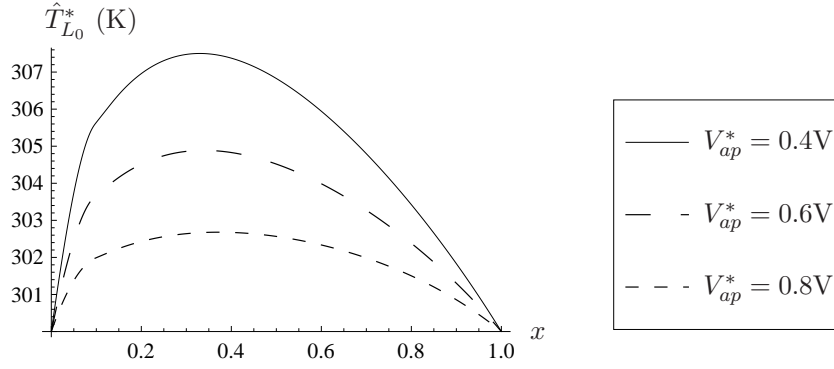


Figure 4.9g: Steady-state solution for lattice temperature across a PN junction at different forward bias under 1 Sun of illumination and AM 1.5 spectrum.

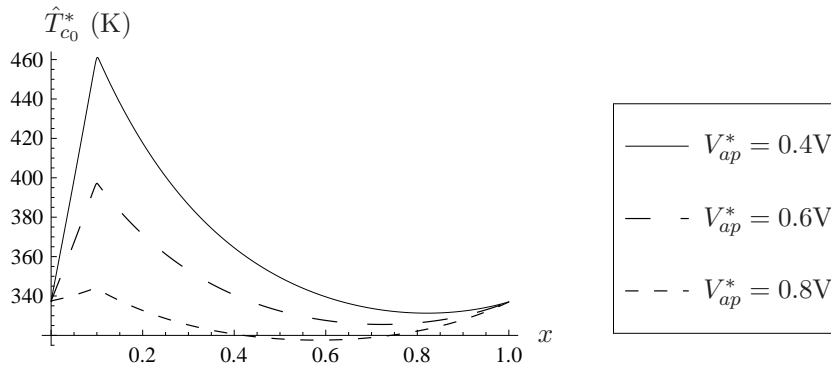


Figure 4.9h: Steady-state solution for carrier temperature across a PN junction at different forward bias under 1 Sun of illumination and AM 1.5 spectrum.

4.3.1 GaAs Solar Cell Characteristics and Comparison to Experimental Data

The voltage-current density characteristics in a GaAs PN junction solar cell with non-symmetric doping concentrations and sides, and with recombination and generation process was studied with the one-dimensional two-temperature hydrodynamic model. The calculated characteristic voltage-current density curves are shown in Figs.4.10 and 4.11. Even though the current density reaches orders of magnitude similar to those of a real operating solar cell, the value is small compared to a cell under 1 Sun of illumination, in other words, the simulated cell is very inefficient. Current is decreased because of the boundary condition used for minority carriers. In this case, the equilibrium condition,

$$n_s = n_0,$$

$$p_s = p_0,$$

was used, which would imply an instantaneous surface recombination. Therefore, substantially decreases the output current. Nonetheless, the behavior regarding temperature changes is analyzed as described below.

Figure 4.10a shows the current density as a function of the applied voltage, for different lattice and electron temperatures as boundary conditions. For each imposed lattice temperature, a corresponding electron temperature was found in order to match the experimental behavior of solar cells. As the cell temperature, T_L , increases, the open circuit voltage, V_{oc} decreases, while the short-circuit current, J_{sc} , is increased [77]. Results from the two-temperature hydrodynamic model, show a good agreement with measured voltage-current characteristics obtained when charge carrier temperature is higher than lattice temperature. The predicted V_{oc} temperature coefficient (dV_{oc}/dT_L) is approximately -2 mV/K as previously reported [78, 79]. The open-circuit voltage is in the order of 1 V at $T_L = 300 \text{ K}$, 0.88 V at $T_L = 350 \text{ K}$, and 0.76V at $T_L = 400 \text{ K}$, and increases when illumination intensity increases [78]. Figure 4.10b presents the corresponding change in power output because of this effect.

On the other hand, when the charge carriers heat up and the lattice temperature boundary conditions remain constant, the power output increases, as shown in Fig.4.11a. Figure 4.11b presents the power output for this case, where the higher peak power is noticeable. This behavior shows a linear dependence similarly to lattice temperature, only with a positive coefficient of approximately $dV_{oc}/dT_n = 3.2 \text{ mV/K}$. Although, this would be extremely difficult to measure experimentally. This is in agreement with hot electron devices [80].

4.3.2 Suggested Improvements in Design of Concentrator Solar Cell

The power output of a concentrator solar cell is increased as the open circuit voltage, V_{oc} , and the short circuit current, J_{sc} are increased. Both V_{oc} and J_{sc} depend on operational conditions such as lattice temperature, charge carrier temperature and light intensity, as well as device characteristics such as device length and doping densities.

The temperature dependence of V_{oc} is influenced by the temperature characteristic of saturation current. This current is proportional to the square root of the ratio between the diffusion constant and lifetime of electrons, which ratio is usually represented by a power-law lattice temperature dependence, T_L^ϕ , with ϕ constant [81]. Using the two-temperature hydrodynamic model, this ratio was observed to be proportional to the carrier temperature, T_c . Consequently, charge carrier temperature plays a fundamental role in the predicted value of V_{oc} and this suggests that some improvements can be done.

According to the results, when the lattice temperature remains constant, V_{oc} increases with charge-carrier temperature, as shown in Fig.4.11a. Even though many simplifications were considered for this example, the qualitative behavior regarding carrier temperatures at the contacts is still expected to be true. Therefore, the real challenge lies in developing energy selective contacts in order to allow hot-carrier extraction. One possibility is by using contacts at both edges of the PN junction with a high electronic thermal conductivity in order to prevent charge carrier temperature fluctuations and avoid the heat dissipation of the photogenerated carriers into the lattice. This heating is commonly known as the Peltier effect, and occurs because of the difference in the Peltier coefficients between the two media. These coefficients represent the amount of heat that carriers are able to transport. On the other

hand, lattice temperature boundary conditions are determined by lattice thermal conductivity as well as packaging layers in a PV module. Based on this analysis, the metal contacts and packaging layers have to be designed to dissipate the heat from hot charge carriers in a sufficiently large region away from the contact-semiconductor interface, in order to operate the solar cell at lower lattice temperatures.

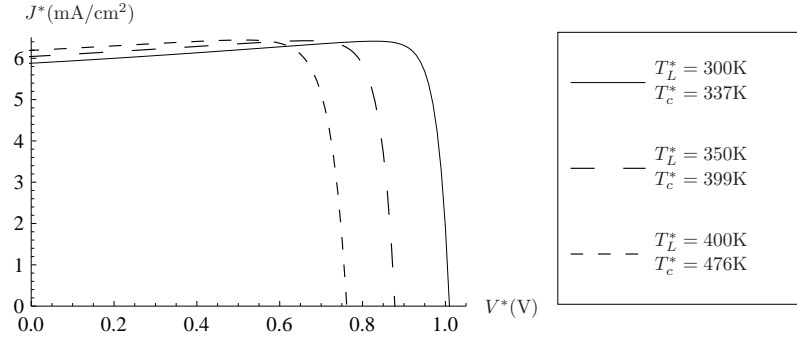


Figure 4.10a: Total current density vs. voltage characteristics for a GaAs PN junction solar cell under 1 Sun with AM 1.5 spectrum, at different lattice temperature boundary conditions, T_L , and different charge carrier temperatures, T_c .

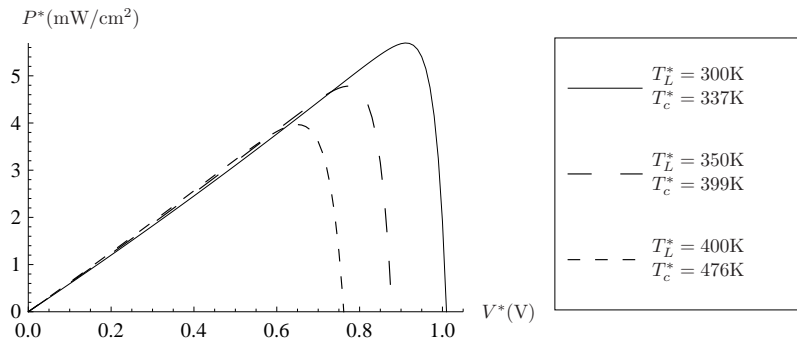


Figure 4.10b: Power output density vs. voltage characteristics for a GaAs PN junction solar cell under 1 Sun with AM 1.5 spectrum, at different lattice temperature boundary conditions, T_L , and different charge carrier temperatures, T_c .

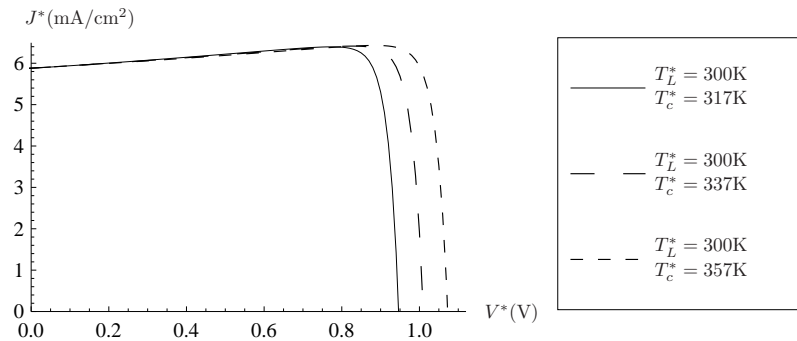


Figure 4.11a: Total current density vs. voltage characteristics for a GaAs PN junction solar cell under 1 Sun with AM 1.5 spectrum, $T_L = 300\text{K}$ (lattice temperature boundary conditions) at different charge carrier temperatures, T_c .

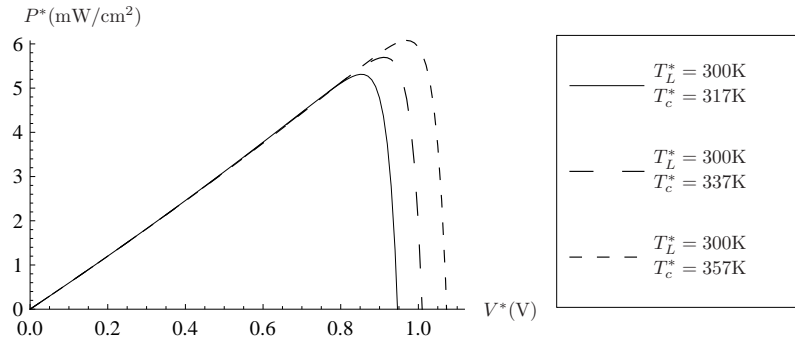


Figure 4.11b: Power output density vs. voltage characteristics for a GaAs PN junction solar cell under 1 Sun with AM 1.5 spectrum, $T_L = 300[K]$ (lattice temperature boundary conditions) at different charge carrier temperatures, T_c

4.3.3 Considerations Regarding the Assumptions for Case 2

Some of the methodology used to obtain the results for this section were later modified. This can be reviewed in greater detail in reference [75]. There were two main issues with the method used. The first is regarding the non-dimensionalization, where some interdependent non-dimensional groups exist. This can be verified with the relation between constants and independent variables, according to the π -Buckingham theorem [82]. In the current version of the non-dimensionalization, this is solved through the use of the thermal voltage U_T . The second issue, which is directly related to the first, is the use of a constant thermal conductivity for electrons, therefore considering it as an independent physical quantity. On the contrary, if the Wiedemann-Franz law is used, κ_n is expressed in terms of physical constants and independent variables that are already in use. This implies that if the asymptotic limit was imposed on R_e , with the first version of the non-dimensionalization and Wiedemann-Franz law. Subsequently, the thermal-conductivity term of the carrier heat-balance equation is also simplified, which implies spatial equilibrium.

As was mentioned, thermal equilibrium density was used for minority carriers boundary condition. This implies an infinite surface recombination velocity, or a semi infinite media. Therefore, it is not appropriate for solar cell modeling. Characteristic curves in Figs. 4.10a and 4.11a present an increase in the current value as the voltage increases, which is not the usual behavior of a solar cell, where the maximum value of current always occurs at J_{sc} . This behavior is caused by numerical errors at the minority boundary due to the infinite value of SRV.

4.4 Hole Temperature Assumption Verification

One of the most significant assumptions used to obtain the results presented in the previous section was to consider $T_p = T_n$. In a follow up work, this assumption is contrasted with the use of $T_p = T_L$. This is done by solving the resulting equation systems under both assumptions, and low field considerations.

The physical justification behind the electron-hole thermal equilibrium, is the fact that both electrons and holes suffer an increase of energy within the SCR, because of the high electric field therein. However, this raises the question of which energy balance should be solved. The course of action in the work presented in the previous section was to assume electron energy balance with an additional term corresponding to the energy delivered by holes. With this, and considering that ν_p is also neglected by the asymptotic approximation, the momentum and energy balance for holes when $T_p = T_n$, are given by

$$u_p = -\mu \left(\frac{\partial V}{\partial x} + \frac{1}{p} \frac{\partial(pT_n)}{\partial x} \right), \quad (4.4a)$$

$$\psi \frac{\partial^2 T_L}{\partial x^2} + \frac{3}{2} (\nu_n n + \gamma \nu_p p) (T_n - T_L) = 0. \quad (4.4b)$$

On the other hand, assuming holes are at thermal equilibrium with the lattice would be equivalent to consider instantaneous thermalization. This is not necessarily a direct assumption, since energy relaxation time for holes is larger than the one for electrons. However, holes in GaAs have a higher effective mass than electrons. Therefore, when energy is delivered to holes a bigger proportion of it corresponds to kinetic energy, rather than thermal. This is also related to the fact that holes have a more ‘flat’ behavior for energy with respect to the wave vector \mathbf{k} , which implies that when an electron-hole pair is photogenerated, a higher portion of the energy above E_g is delivered to electrons. In the case where $T_p = T_L$, the momentum and energy balance are given by

$$u_p = -\mu \left(\frac{\partial V}{\partial x} + \frac{1}{p} \frac{\partial(pT_L)}{\partial x} \right), \quad (4.5a)$$

$$\psi \frac{\partial^2 T_L}{\partial x^2} + \frac{3}{2} \nu_n n (T_n - T_L) = 0. \quad (4.5b)$$

The rest of the equations for both cases are given by Poisson’s equation (3.26a); steady state continuity equations (3.29a) and (3.29b); low-field momentum balance for electrons (3.30a); and low-field energy balance for electrons (3.30b). The conditions under which this case of example was solved are very similar to those of Case 1, with the difference of the p -side being shorter than the n -side, which is characteristic in solar cells. The parameters for this example, labeled as Case 3, are summarized in Table 4.7

Table 4.7: Relevant parameters and properties for Case 3.

Parameter	Value	Units
N_A	10^{22}	$[m^{-3}]$
N_D	10^{21}	$[m^{-3}]$
L	$4 \cdot 10^{-6}$	$[m]$
x_J	$0.2L$	$[m]$
V_{app}	0.5	$[V]$
T_l	300	$[K]$
#Suns	1	–

Under the given conditions, $\varepsilon_n = 2.43 \cdot 10^{-4}$, which corresponds to a Knudsen number of $K_n = 0.0156$, and it is relatively safe to use the asymptotic approximation as well. The built in voltage is $V_{bi} = 1.096[V]$. Figure 4.12 presents the electric potential (left) and electric field (right) for the steady state solution of Case 3. The solid lines correspond to $T_p = T_L$, while the dotted lines $T_p = T_n$.

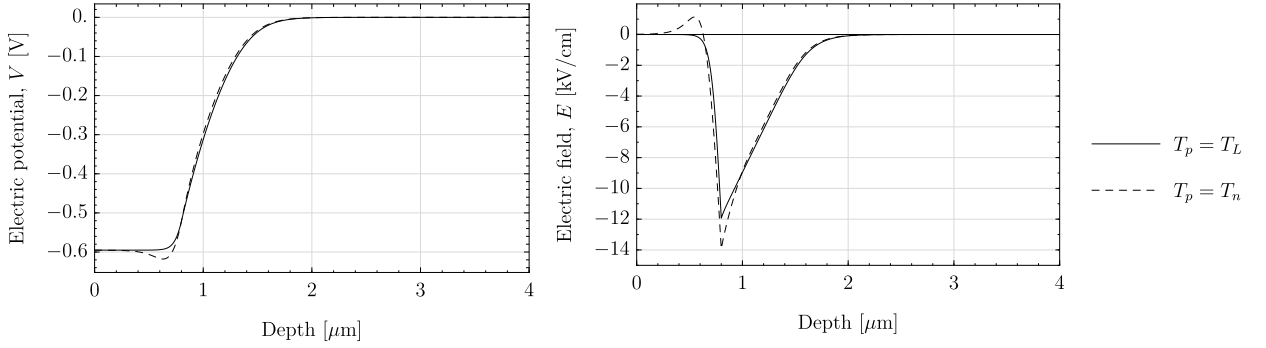


Figure 4.12: Electric potential and field under the assumptions of $T_p = T_L$ and $T_p = T_n$.

A clear depression can be seen in the voltage level near the junction for the case of electrons and holes at thermal equilibrium. This implies a larger voltage drop across the junction, and therefore a higher electric field, which can be seen in the figure to the right. Besides, in order to fulfill the boundary conditions given by $|V_{app} - V_{bi}|$, voltage increases again as the p -side is reached, which implies a negative differential voltage and, therefore, a reversed electric field. While it is possible to observe this kind of behavior in some electronic devices, it is not characteristic of a solar cell. Not only this, but it would have negative consequences, since it would repel electrons from reaching the SCR rather than attract them. In terms of energy this depression can be directly related to the quasi-Fermi levels of energy carriers, which are clearly modified by the assumption of $T_p = T_n$.

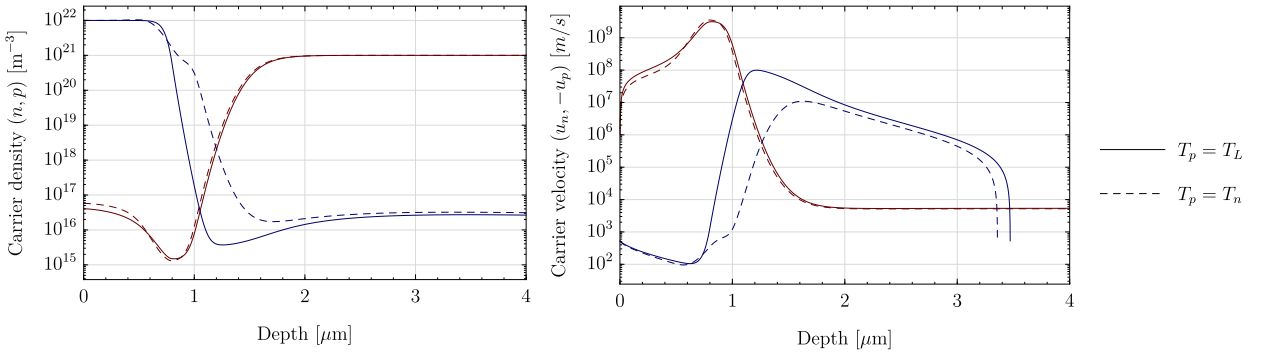


Figure 4.13: Carrier densities and velocities under the assumptions of $T_p = T_L$ and $T_p = T_n$. The red and blue lines correspond to electrons and holes respectively.

Figure 4.13 shows the effect of considering each assumption on carrier densities and velocities. The graph on the left presents carrier densities, red lines are for electrons, while holes are represented with blue. The same is true for carrier velocities, presented in the figure at

the right. Once again, the solid lines represent the curves using $T_p = T_L$, and the dashed lines $T_p = T_n$. Evidently, hole density and velocity are the variables that suffer the greater changes when comparing both assumptions. The difference is related to the assumption of thermal equilibrium for holes. This assumption is equivalent to solving hole mass balance with an imposed higher temperature level at the p-side of the junction, which increases the number of holes in order to maintain the balance. This increase in density is higher than the corresponding temperature gradient, and therefore hole velocity is decreased. Additionally, given the high density and low mobility of holes near the junction, they are not correctly transported into the p-side. Therefore, the characteristic depression in carrier density near the junction for solar cells under operating conditions is not observed. This implies this an unrealistic result.

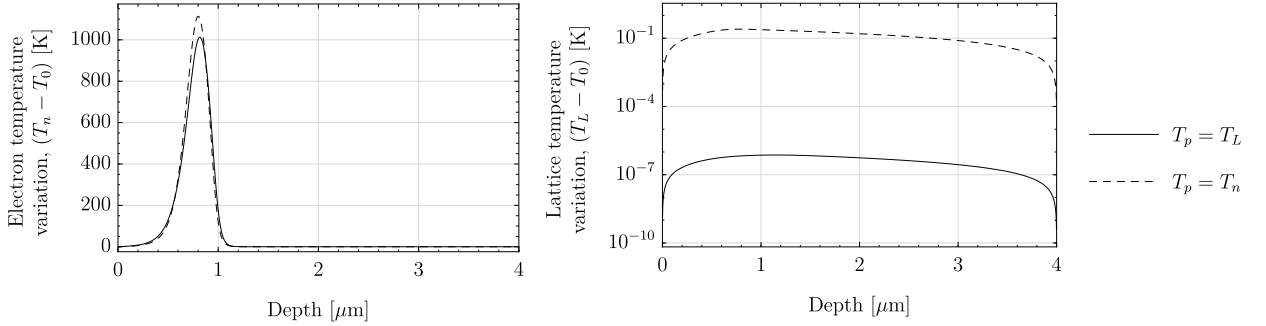


Figure 4.14: Electron and lattice temperature increase under the assumptions of $T_p = T_L$ and $T_p = T_n$.

Figure 4.14 shows the variation of electron (left) and lattice temperatures (right). Since the electron energy balance is practically the same in both cases, the temperature profile does not change significantly, which implies the contribution of holes is not important. Therefore, assuming $T_p = T_n$ is similar to imposing the thermal behaviour of electrons on holes. Hole current density can be expressed as

$$J_p = -\mu \left(p \frac{\partial V}{\partial x} + T_n \frac{\partial p}{\partial x} + p \frac{\partial T_n}{\partial x} \right), \quad (4.6)$$

where it can be noticed that a variation in $\partial T_n / \partial x$ directly affects the internal current behavior. If a peak of temperature is considered like the one in Fig. 4.14, then electric field and carrier densities must compensate, because the total current must remain constant across the device. As described above, under these conditions holes density will increase closer to the n -side, and this increase in the density implies a decrease in the mean hole velocity. At the same time, this ‘excess’ of holes builds up a negative charge, which is expressed in the changes in electric field. These changes in carrier densities also affect the recombination level, which in turn affects the attainable currents. Figure 4.15, presents the recombination level for both assumptions.

Evidently, under the assumption of $T_p = T_n$, the net recombination value is much higher. This means the total current in this case will be lower. The values of the total output current density in each case are

$$J_T (T_p = T_n) = 199.2 [A/m^2],$$

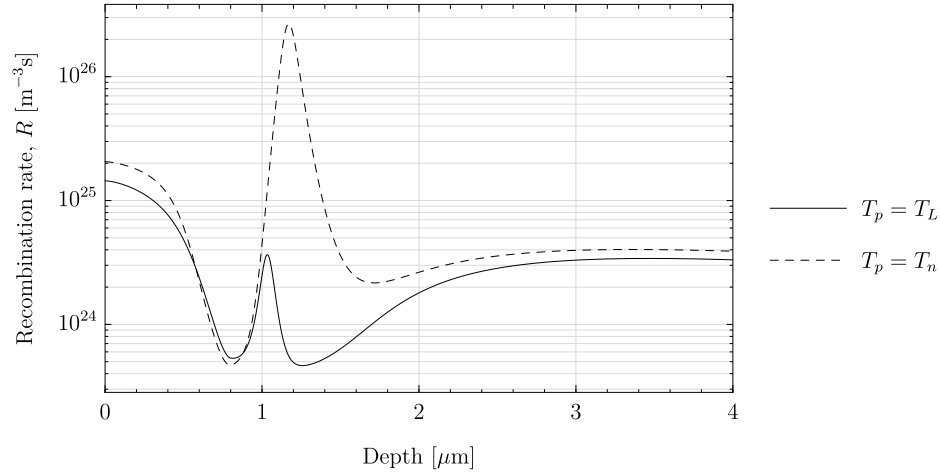


Figure 4.15: Recombination rate under the assumptions of $T_p = T_L$ and $T_p = T_n$.

$$J_T(T_p = T_L) = 205.7[A/m^2].$$

A change in total current density does not necessarily mean one or the other assumption is more accurate, but comparing the recombination profiles across the device, the one corresponding to $T_p = T_L$ presents a behavior more in accordance with the classical assumptions that there is zero recombination across the SCR.

In summary, assuming holes at thermal equilibrium with electrons leads to results that are much more questionable than assuming them at thermal equilibrium with the lattice. Additionally, the thermal equilibrium between electrons and holes is much more difficult to achieve than between holes and lattice, given that scattering processes between electrons and holes are much more rare than holes scattering with phonons. Solving for hole temperature as a separate variable would also lead to a peak temperature at the junction, but the maximum value and shape of the curve would be very different, which yields different results. These differences would be much more significant when adding more thermal effects such as heating through recombination, or over bandgap photons, to the carrier energy balance. Therefore, when trying to simplify the model, holes at thermal equilibrium with the lattice is a better assumption.

4.5 High Field Mobility Effects

As discussed in Section 2.3, high-field effects have a major impact on the transport conditions for charge carriers. These effects have been attempted to be quantified by different models that reproduce the experimental behavior of semiconductor materials. In order to provide the most accurate description of charge carriers behaviour for future works, the following section studies the implications of using different mobility models in charge transport parameters. For the modeling of velocity saturation, the temperature dependent model introduced by Baccarani & Wordeman is compared with the one by Hänsch. Similarly, for transferred electron effect different assumptions are analyzed for the model based on the population rate using Boltzmann distribution, and compared with the transferred electron empirical model and Monte Carlo data.

In order to compare electron temperature and electric field dependent models, both of them are analyzed under physical assumptions that allow to obtain a direct relation between these two variables. This is usually done by assuming a bulk semiconductor under the effect of a constant electric field, and no consideration for spatial or temporal gradients for carriers. This leads to Eq.(2.103), which using the definition of electron average energy is equivalent to assuming $(\partial_t T_n)_c = 0$ in Eq. (2.75a). In other words, a balance of the energy yielding from carriers to the lattice is done with no diffusive effect consideration. Electron temperature can then be written in terms of electric field as

$$T_n = \frac{2e^2 \tau_{\epsilon,n} \tau_{m,n}}{3k_B m_n} \left(1 - \frac{\tau_{m,n}}{2\tau_{\epsilon,n}} \right) E^2 + T_L. \quad (4.7)$$

Lattice temperature is considered to be constant, contrary to the HD model used in this work where an additional energy balance is included. The transport parameters $\tau_{m,n}$, m_n and $\tau_{\epsilon,n}$ are all averaged effective quantities and do not represent the properties of each single electron, but the electron cloud as a whole. Therefore, under high field conditions and considering the transferred electron effect, all of them depend on electron temperature T_n , making Eq.(4.7) an implicit expression. Most of the times, even when electron temperature is being considered as the independent variable for changes in transport properties, the concept of mobility is used in replacement of $\tau_{m,n}$ and m_n . This is done by assuming $\tau_{m,n} \ll \tau_{\epsilon,n}$, which is equivalent to the asymptotic approximation of $\nu_n \rightarrow 0$ in the non dimensional version of the equations presented in Section 3.5. With this, electron temperature depends on the electric fields according to

$$T_n = \frac{2e\tau_{\epsilon,n}\mu_n}{3k_B} E^2 + T_L, \quad (4.8)$$

obtaining a relation that directly applies the concept of mobility, without accounting separately for changes in effective mass and momentum relaxation time. Nonetheless, since our interest is in every independent transport parameter, Eq. (4.7) will be used for the evaluation of different transport models, regardless that the results are very similar.

4.5.1 Velocity Saturation Models

Models that represent the saturation of velocity are widely used for covalent semiconductors, for instance Si or Ge, but do not depict accurately the behavior of polar semiconductor such as GaAs or CdTe which have satellite bands. However, in this kind of materials, these models are useful for characterizing each band separately. A distribution function can then be used in order to determine the population of each band and its local contribution to conduction. This procedure is explained in the following section. In the present section, the model of Baccarani & Wordeman (BW) and the Hänsch model, are compared in order to define which of them will be used to determine the transport properties of electrons at each independent conduction band.

The starting point of BW model is the assumption of a constant diffusion coefficient D_n . This implies that $\gamma_F = -1$ for Eq. (2.102), and gives a relation for momentum relaxation time based on an experimentally measurable parameter. Consequently, energy relaxation time accounts for the necessary variations in temperature for the transport of carriers to obey the experimental behavior regarding electric field. In contrast, Hänsch model directly assumes a constant energy relaxation time, but derives a very good approximation for mobility while also maintaining self consistency. Despite these differences, both models describe the degrading behavior of mobility as energy is increased. Saturation velocity for GaAs is used according to the value given in Table 2.7. Even though as electric field increases, electron velocity should continue to decrease, this value is normally used for reference purposes.

Figure 4.16 shows the behavior of mobility as electric field increases, according to BW and Hänsch models. The value of $\tau_{\epsilon,n}$ for Hänsch model was taken as the low field value for BW model, $\tau_{\epsilon}^{\text{bw}}$, given by Eq. (2.104). Therefore, both models use the same low field momentum relaxation time. It can be observed how for low values of electric field the value of mobility remains practically constant. However, for values of electric field above 100 V/cm, mobility varies significantly. As a reference, a PN junction with doping levels of $N_A = 10^{16} \text{ cm}^{-3}$ and $N_D = 10^{15} \text{ cm}^{-3}$ for the p and n sides respectively, can reach local electric field values of the order of 10 kV/cm in the area near the junction. Doping values for high performance solar cells are even higher than these.

From Fig. 4.16, it can also be seen how mobility steadily decreases for both models for high electric fields. This correlates with electrons asymptotically reaching the saturation velocity value, as can be observed in Fig. 4.17. Even though a noticeable difference is observed between both models for the middle values of electric field, it is irrelevant to select only from these results the best model to use, given that this is not the actual behavior of electrons in GaAs. A comparison could be made instead on their applicability for independent band modeling.

The fact that Hänsch's model adjusts its behavior considering a constant energy relaxation time implies that using it becomes more arbitrary than using BW model. Figure 4.18 presents the variation of drift velocity with respect to the electric field, for three different choices of τ_{ϵ} . All of the relaxation times were evaluated at $T_L = T_n = 300 \text{ K}$, and a doping density of $N_D = 10^{16} \text{ cm}^{-3}$. The blue solid line corresponds to $\tau_{\epsilon 1} = \tau_{\epsilon,n}^{\text{bw}}$ and the red dashed line uses $\tau_{\epsilon 2} = \tau_{\epsilon,n}^{\text{mc}}$, from Eqs. (2.104) and (2.107) respectively. The green dotted line uses an

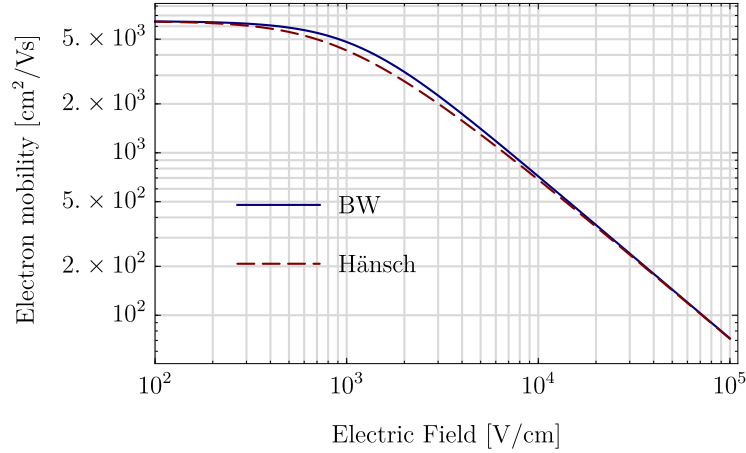


Figure 4.16: Mobility in GaAs as a function of electric field, according to Baccarani & Wordeman and Hänsch models.

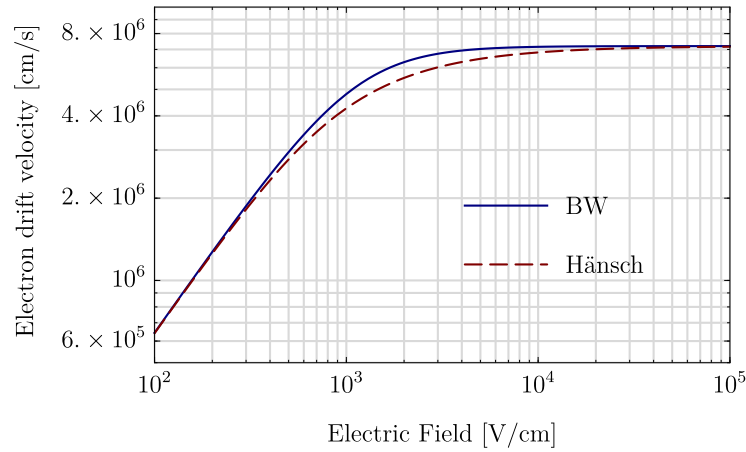


Figure 4.17: Drift velocity in GaAs as a function of electric field, according to Baccarani & Wordeman and Hänsch models.

arbitrary energy relaxation time given by $\tau_{e3} = \tau_{e,n}^{mc}/2$. It is observed that all the energy relaxation times show a good agreement with the expected results, even when there is almost an order of magnitude of difference between the highest and lowest values. This is expected, since Hänsch model uses τ_e as a parameter for the calculation of mobility, therefore it adjusts very well for a wide range of values.

The most important difference between both models can be observed when analyzing electron temperature as the independent variable. According to Eq. (4.7), the use of a different value of τ_e has significant effects on the rise of temperature due to the effect of the electric field. This variation is shown in Fig. 4.19, where T_n as a function of electric field is depicted for the BW model, and several values of $\tau_{e,n}$ for the Hänsch model. A difference of nearly one order of magnitude can be observed when using the Hänsch model, assuming different τ_e .

This difference in temperature needs to be compensated for different models to describe a similar behavior of mobility regarding electric field. Figure 4.20, presents the change in mobility using both models for GaAs at $T_L = 300[K]$, T_n ranging from 300 to 800 and two

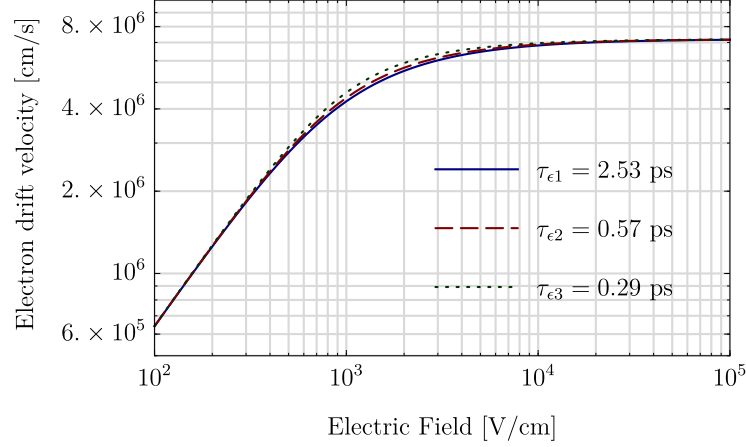


Figure 4.18: Drift velocity in GaAs as a function of electric field according to Hänsch model, considering different values for energy relaxation time.

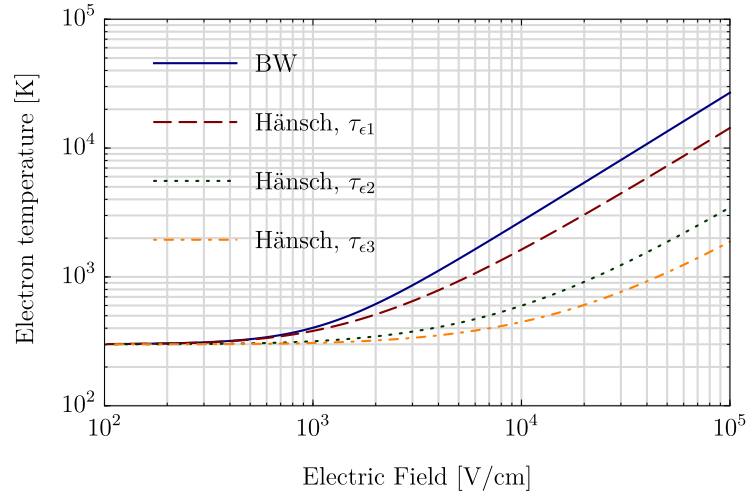


Figure 4.19: Electron temperature in GaAs as a function of electric field, according to Baccarani & Wordeman and Hänsch model, using different values for energy relaxation time.

doping levels, $N_D = 10^{16}$ and $N_D = 10^{18} \text{ cm}^{-3}$. The value of energy relaxation time for Hänsch model is equal to the low field value of BW model. It can be seen how for lower doping levels the difference between using one model or the other is significant, but for higher doping levels this difference becomes less important. This is related to the fact that energy relaxation time according to the BW model varies indirectly with the doping level through low field mobility. The choice of this parameter for Hänsch model increases the difficulty of obtaining a consistent model, and could be potentially used to adjust the model to fit experimental results. In this sense, it can be argued that BW model has the limitation of having less parameters to fit experimental data, given that β_C , the exponent in Canali model, is chosen to be equal to 2. However, using non-integer values for β_C would result in much more complex or non explicit expressions for τ_m and τ_e .

These results show that both models have different behavior regarding temperature, but predict the same results for electric field due to the effect of τ_e , which quantifies the effect of

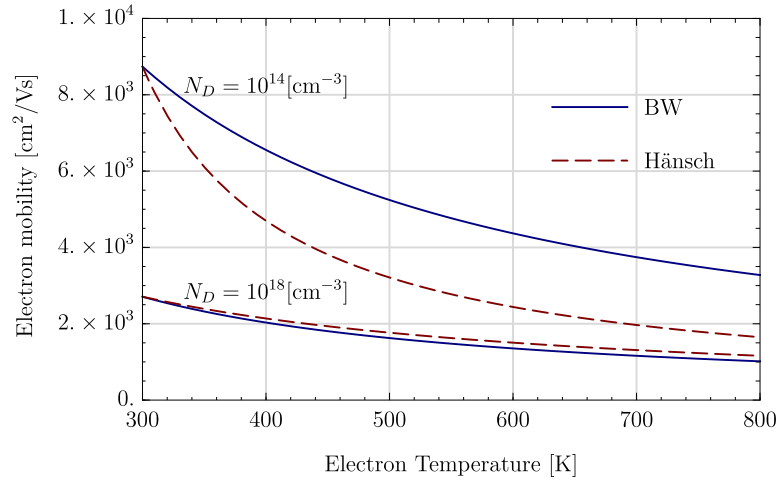


Figure 4.20: Mobility in GaAs as a function of carrier temperature (high field), according to Baccarani & Wordeman and Hänsch models, for two doping levels.

thermalization. This implies that when analyzing electronic devices using a HD model, the choice of the phenomenological relations for high energy transport parameters has significant effects on the thermal behavior described by the model. In this sense, the use of Hänsch model for each band in order to define the total effective transport parameters generates even more questions regarding the assumptions. As described, this model uses a constant energy relaxation time and as was shown, this parameter can be selected within a wide range of values, not affecting significantly on the resulting mobility of electrons, but having an important impact on electron temperature. For these reasons, BW model was selected over Hänsch for the modeling of independent bands in GaAs.

4.5.2 Baccarani & Wordeman Transferred Electron Model

As described in Section 2.3, transferred electron effect (TEE) occurs when electrons are excited from a low-mass central valley to a high-mass satellite valley. Under certain conditions this generates a negative differential mobility, which has many possible applications and effects. The models presented above are useful to determine the transport properties of charge carriers moving along a single band, assumed to be spherical and parabolic. Therefore, when studying materials where the TEE is important, other approaches are needed. The most common is to consider the dependency of drift velocity regarding the electric field, as presented in Eq.(2.108). This model is shown in Fig. 2.13 for two different references along with results from a Monte Carlo simulation.

The approach implemented on this work models each band independently, and accounts for the TEE through the use of the population ratio P_L , defined in Eq.(2.112).

As presented in the previous section, the basis of the BW model is to represent the behavior of carriers at high energies as they reach the saturation velocity. Here, the main input parameters that adjust the model to empirical data are the low-field mobility and the saturation velocity. This means that in order to model both band separately, four parameters

are needed; the low-field electron mobility of each band, defined as μ_{n0}^{Γ} and μ_{n0}^L , and the corresponding saturation velocities $v_{n,\text{sat}}^{\Gamma}$ and $v_{n,\text{sat}}^L$. From these parameters, the only one that is readily experimentally measurable is μ_{n0}^{Γ} , since this is the mobility measured at low fields, where most of the electrons are located within the Γ -band. As discussed in Section 2.3, this parameter is mainly affected by doping density and temperature of the sample. In turn, the low-field mobility for electrons in the L -band is not a measurable parameter since these electrons only exist under high energy conditions. In the same manner, saturation velocities for each band are never reached, since they correspond to the average velocity that would be achieved if the transference of electrons did not exist. Consequently, the total average electron velocity is bounded by these two values, being $v_{n,\text{sat}}^{\Gamma}$ the upper limit and $v_{n,\text{sat}}^L$ the lower. These velocities are not experimentally measurable, although $v_{n,\text{sat}}$ should be closer to $v_{n,\text{sat}}^L$. Since at high electric fields coulombic type scattering becomes less effective for increasing carrier energy [83], saturation velocities are much more stable regarding changes on doping level and/or quality of the sample.

The value of mobility that electrons would have if they traveled only through the L -band at low fields is not directly noticeable on their average behavior. However, it does affect the way this band is modeled and therefore it is important for the approach used in this work. One of the few references that can be found for the value of μ_{n0}^L is a study by Nichols *et al.* [84], which attempts to isolate the effect of each independent band in the mobility of GaAs samples. An even greater decrease in mobility because of temperature compared to mobility of the Γ -band was reported here, although this is not considered in the present work. From this, a value of $\mu_{n0}^L \sim 2500 \text{ cm}^2/\text{Vs}$ can be extracted [21].

The total value of saturation velocity is an important parameter in order to reach the desired performance of many devices, therefore, many studies have been done in order to find its value with precision. Most common studies use indirect measurements through Gunn or IMPATT diodes [85]. This implies the obtained value depends on material parameters such as the diffusion constant. Other more direct method is the time-of-flight technique, but this is harder to accomplish for very high fields [83, 86]. These studies have shown that for very high fields, the saturation velocity in GaAs continues to decrease as the electric field increases, which can be explained by more electrons being transferred to the L -valley or even to the upper X -valley. Considering this, the value of $v_{n,\text{sat}}^L$ will be assumed to be that of the total saturation velocity for electrons at very high fields. Just as μ_{n0}^L , the saturation value for electrons at the Γ -valley, $v_{n,\text{sat}}^{\Gamma}$, is useful only in a method where both bands are modeled separately given that at very high fields, most electrons are moving through the L -valley. Because of this, not much reference is found either for this value. The only reference that could be found was a study on heterojunction bipolar transistors (HBTs) by Palankovski [29], where $v_{n,\text{sat}}^{\Gamma} = 2.5 \cdot 10^5 \text{ m/s}$ was used. An interesting step towards the validation of this model would be to obtain these parameters from Monte Carlo simulations.

Using these parameters, the average velocity for electrons moving through each individual valley can be calculated. These are shown in Fig. 4.21, where the upper curve represents the velocity of the faster electrons in the Γ -band, and the lower curve the slower electrons moving in the L -band. The transferred electron model using the parameters from Barnes [49] is also depicted as a reference. Electron drift velocity is plotted rather than mobility because it describes more graphically the effect of transferred electrons. It can be observed

how the curve of the TE model shows a peak value which is higher than the predicted value for the Γ -valley electrons at the corresponding field. Since the value of low-field mobility, $\mu_{n,0}^\Gamma$, has been thoroughly studied, this may suggest a higher value of saturation velocity for electrons in the Γ -valley, or a different behavior regarding electric field than the one described by Caughey & Thomas [42], such as a higher value of β_C in Eq.(2.99), on the model given by Canali. Unfortunately, using the Canali model does not allow to derive such a simple expression for relaxation times as a function of carrier temperature as the one given by Baccarani & Wordeman. The effect of varying $v_{n,\text{sat}}^\Gamma$ is studied ahead.

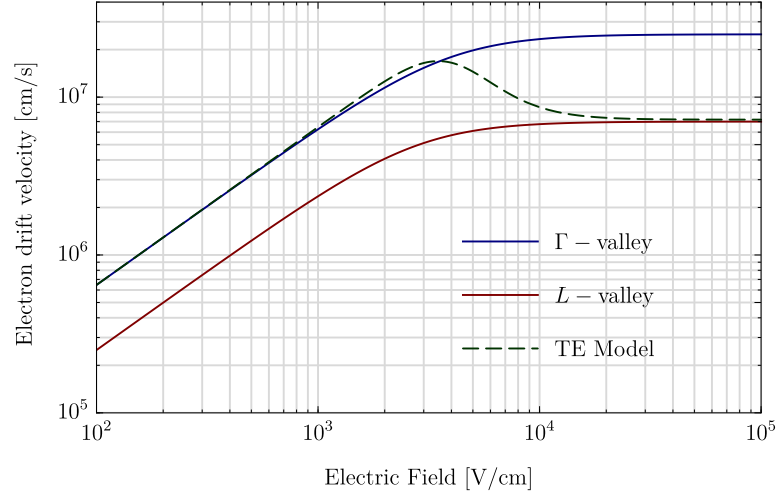


Figure 4.21: Average electron drift velocity for individual valleys using the BW model, along with the field dependent transferred electron model.

Having the behavior of electrons on each valley, it is straightforward to model the effect of TEE in mobility using Eq.(2.116). However, another difficulty arises when considering calculation of the total energy relaxation time, given that this is not an intrinsic property of electrons moving in a certain band, but a result of the rate of thermalization of hot electrons. Therefore, it can not be calculated by simply weighting the parameter for each band, as in Eq.(2.116). Due to this, two different averaging functions are compared. The first one considers energy relaxation time as an intrinsic property of each electron in the corresponding valley, therefore

$$\tau_{\epsilon,n} = f_1(\tau_{\epsilon,n}^\Gamma, \tau_{\epsilon,n}^L) = \frac{\tau_{\epsilon,n}^\Gamma + P_L \tau_{\epsilon,n}^L}{1 + P_L}. \quad (4.9)$$

The second option arises from considering only the thermalization in the collision component of carrier temperature. Therefore,

$$n(\partial_t T_n)_c \approx -n_\Gamma \frac{T_n^\Gamma - T_L}{\tau_{\epsilon,n}^\Gamma} - n_L \frac{T_n^L - T_L}{\tau_{\epsilon,n}^L}, \quad (4.10)$$

which if $T_n^\Gamma = T_n^L$ is assumed, delivers

$$\tau_{\epsilon,n} = f_2(\tau_{\epsilon,n}^\Gamma, \tau_{\epsilon,n}^L) = \frac{(1 + P_L) \tau_{\epsilon,n}^\Gamma \tau_{\epsilon,n}^L}{P_L \tau_{\epsilon,n}^\Gamma + \tau_{\epsilon,n}^L}. \quad (4.11)$$

However, this assumption would be valid only when $3k_B T_n \gg m_n u_n^2$, which restrains the validity of the model. Figure 4.22 presents the comparison between the two functions, along with the results using the TE model. It can be clearly observed how the first weighting function delivers a much better approximation with the TE model as a reference. This occurs because of the dependency of energy relaxation times with temperature. Figure 4.23 shows the electron temperature dependence of total energy relaxation time τ_ϵ , using the two weighting functions f_1 and f_2 . It can be seen that the increase in total energy relaxation time when using f_1 is much sharper than when using f_2 . A higher τ_ϵ implies a lower energy transfer from carriers to the lattice, which means higher temperatures are reached and more electrons are transferred to the satellite band. This implies that when f_1 is used, mobility decreases at lower electric fields than when using f_2 , as can be seen in Fig. 4.22. It can also be noticed that the peak average velocity in the TE model does not agree with the one delivered by the present model. Therefore, some parameters can be altered in order to obtain a better approximation.

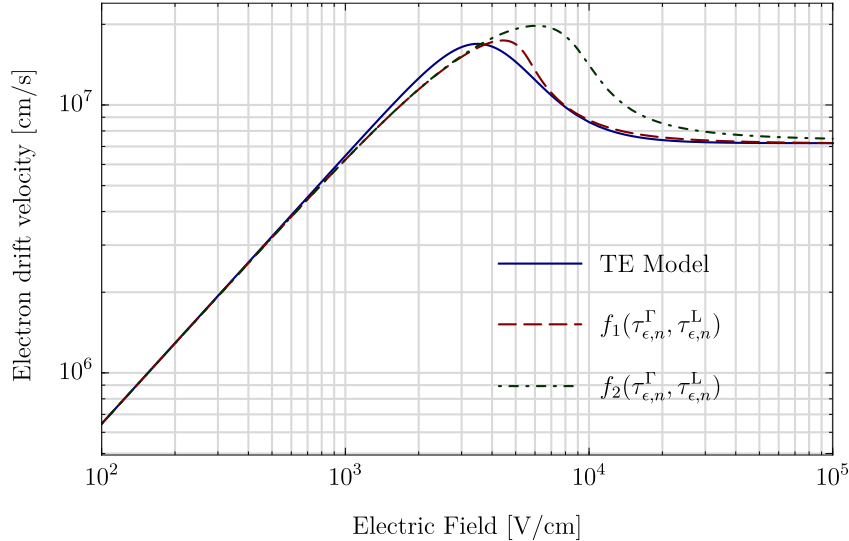


Figure 4.22: Total average electron drift velocity using the BW model for each band, along with the transferred electron model. Two different weighing functions for the total energy relaxation time are used.

One way of achieving a better fitting with the parameters in hand, is to increase the saturation velocity of electrons in the Γ -valley, taking in consideration that this is one of the most uncertain parameters, along with the low-field mobility of electrons in the L-valley. Therefore, increasing $v_{n,\text{sat}}^\Gamma$ would require an adjustment of $\mu_{n,0}^L$. Through trial and error, a value of $v_{n,\text{sat}}^\Gamma \sim 4 \cdot 10^7$ cm/s is obtained for the peak value of the TE model to be lower than the curve for electrons at the Γ -valley. Figure 4.24 shows three curves for different values of $\mu_{n,0}^L$, corresponding to 2.5, 3.5 and 5 cm²/Vs. The mentioned value of $v_{n,\text{sat}}^\Gamma$ was used in all cases. Even though the Γ -valley curve is always above the one given by the TE model, the peak velocity reaches values that are much higher. Because of the larger difference in velocities of electrons in both valleys, the change in mobility is also much more abrupt. Increasing the L-valley mobility only slightly decreases the velocity peak and makes the mobility change much steeper than it is expected to be.

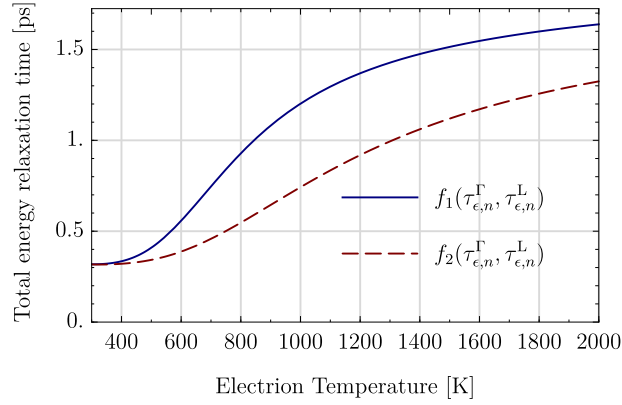


Figure 4.23: Total energy relaxation time $\tau_{\epsilon,n}$ as a function of electron temperature, using the two different weighing functions f_1 and f_2 .

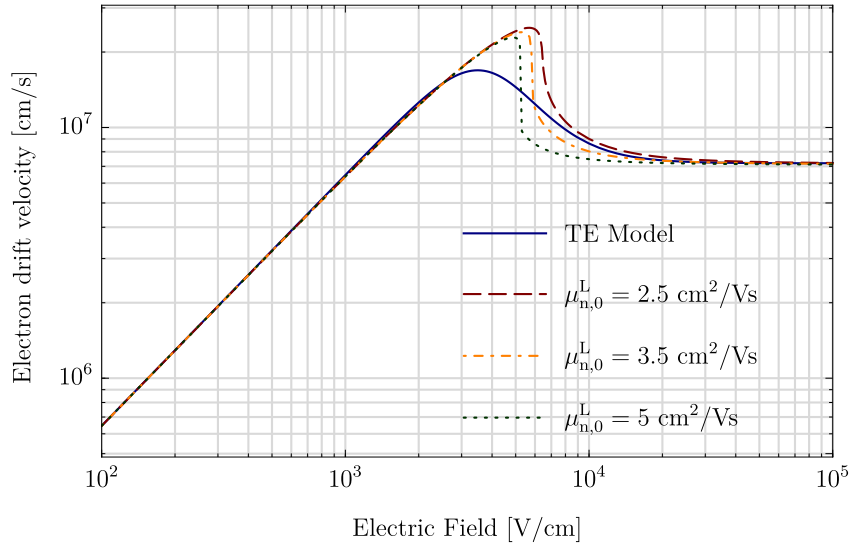


Figure 4.24: Total average electron drift velocity using the BW model for each band, along with the transferred electron model. Three different values of $\mu_{n,0}^L$ are used, for a saturation velocity of $v_{n,\text{sat}}^\Gamma = 4 \cdot 10^7$.

It is concluded that the shifting of the peak velocity value regarding electric field can be corrected by adjusting some parameters, particularly $v_{n,\text{sat}}^\Gamma$. However, in order to do this a different distribution function would be needed for P_L , instead of the Maxwell-Boltzmann distribution. This would make the calculations of transferred electrons much more complex, and no references have been found where this is done. As discussed above, a different behavior regarding electric field can also be assumed through the use of a different parameter β_C for the Γ -valley electrons, which also makes the calculation of the transport parameters for the corresponding band much more difficult. A very interesting exercise would be to perform Monte Carlo calculations of these parameters, modeling the behavior of each band as if no transference of electrons existed. With this, the need of a different population ratio P_L would be verified. Therefore, under these conditions the better fitting achieved is through the use of the mentioned parameters found in references, despite the displacement of the peak velocity value.

Finally, in order to verify the accuracy of the model, a comparison is made with a study by Tait [52], where phenomenological transport parameters are derived from large scale Monte Carlo particle simulations, in order to be used in a hydrodynamic model. In the cited study, different values of effective mass and saturation velocity for electrons in the satellite valley are used, compared to this work. In order to compare these parameters with the ones given by the transferred electron model using Baccarani & Wordeman relations (BWTE model), the same values are used. Figure 4.25 compares the high-field electron drift velocity using different models. The blue solid line shows the results for the transferred electron field dependent model (TE model); the red dashed line the results using the Baccarani & Wordeman model for each band (BWTE model); and the black triangles the results from the Monte Carlo simulations.

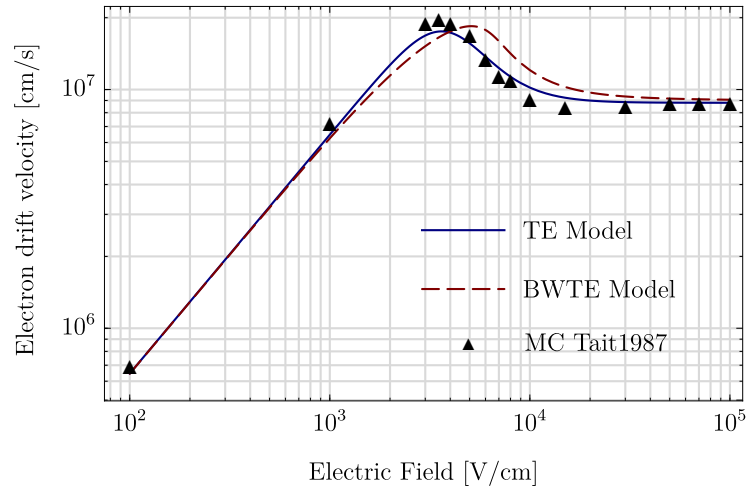


Figure 4.25: High-field electron drift velocity using the field dependent and Baccarani & Wordeman based transferred electron models, along with Monte Carlo results from Tait [52].

A very good agreement is observed between the TE model and the Monte Carlo results for electron velocity. In the case of the BWTE model, a larger difference can be observed, showing a displacement of the curve near the peak value, which is shifted towards higher fields for the BWTE model. As described above, the most probable cause of these differences is the expression used for the population ratio of electrons. However, the temperature dependency of the BWTE model allows to obtain an insight on the causes of these differences, through the analysis of the rest of the transport parameters involved. Figures 4.27 to 4.29 present the field dependent behavior of effective mass, temperature, momentum relaxation time and energy relaxation time, respectively.

Given the general expression for electron mobility $\mu = e\tau_m/m_n$, the main variables that affect the velocity of electrons are momentum relaxation time and total effective mass. These parameters also depend on electron temperature, which in turn is affected by the rate of thermalization, determined by the energy relaxation time τ_e . Figure 4.26 shows the comparison of electron momentum relaxation time between the BWTE model and Monte Carlo results. The major differences can be seen in the medium fields region, where the peaks of τ_m coincide with the corresponding peaks of electron velocity. A steady decrease is observed

for high electric fields, which is necessary in order to achieve velocity saturation, considering a constant effective mass. It is then concluded that the higher differences for medium fields are related to different behavior of total electron effective mass.

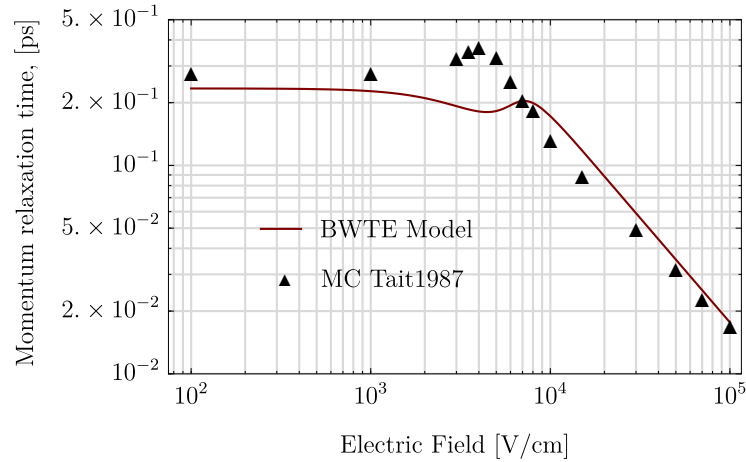


Figure 4.26: High-field behavior of momentum relaxation time for electrons using the Baccarani & Wordeman based transferred electron model, along with Monte Carlo results from Tait [52].

Figure 4.27 presents the comparison of total electron effective mass between the BWTE model and Monte Carlo results. It is verified that the mid-field region is where the larger differences between results are seen. For high-field conditions, total effective mass depends on the amount of electrons on each band, therefore it depends directly on the total energy of electrons. The approach used in this work is to use the population ratio P_L , which assumes that electron energy can be approximated through their temperature. Neglecting the population at the X -valley, electrons can only have the mass corresponding to Γ and L valleys. Therefore, the comparison between Monte Carlo results and BWTE model shows the accuracy of the approximation used to calculate this ratio. It is expected that both curves have similar values for both very low and very high electric fields, given that the same effective masses of independent bands are being used, which can be seen in Fig. 4.27. However, the Monte Carlo results show that the onset of electron transfer to the satellite band occurs earlier than P_L predicts, and the transfer process is not as abrupt as shown by the BWTE model. This confirms that the main relation to be optimized in this model is the population ratio, P_L .

As can be seen in Fig. 4.28, the behavior of electron temperature varies importantly with respect to the electric field for both models, which is directly related to the behavior of energy relaxation time, shown in Fig. 4.29. In relation to the rest of the parameters analysed, these are clearly the ones that show a larger deviation from the Monte Carlo results. They also show similar inflexion points, given their coupling through thermalization. Since the model is based on fitting the behavior of mobility, electron temperature, by means of the energy relaxation time, is the variable that controls these differences and makes the model fit better. Another important result is the verification of the fact that energy relaxation time does not behave as an intrinsic property similar to effective mass, therefore, a different expression is needed in order to obtain more reliable temperature results. As expected, higher levels

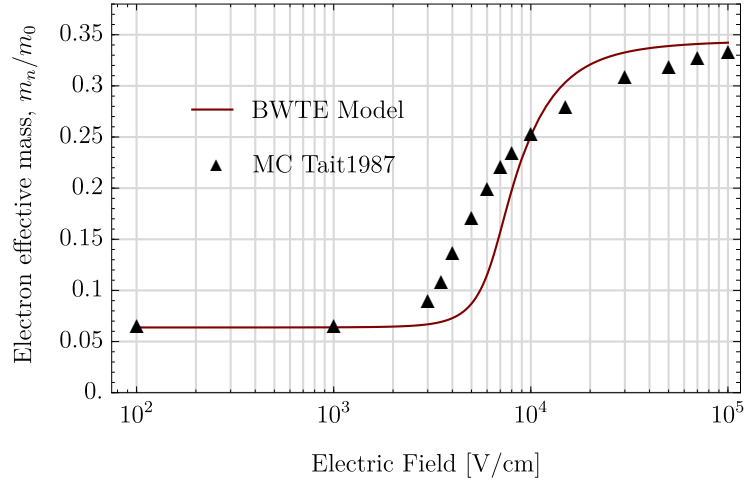


Figure 4.27: High-field behavior of electron effective mass using the Baccarani & Wordeman based transferred electron model, along with Monte Carlo results from Tait [52].

of electron temperature are directly related to higher values of total effective mass, which means that in the Monte Carlo simulations, electrons on average gain more energy at lower fields. This correlates with the coupling of energy relaxation time and the population ratio with electron temperature. On the other hand, the similarity in the highest field value of the results of both models is not relevant, given that for even higher electric fields the difference in results would be larger.

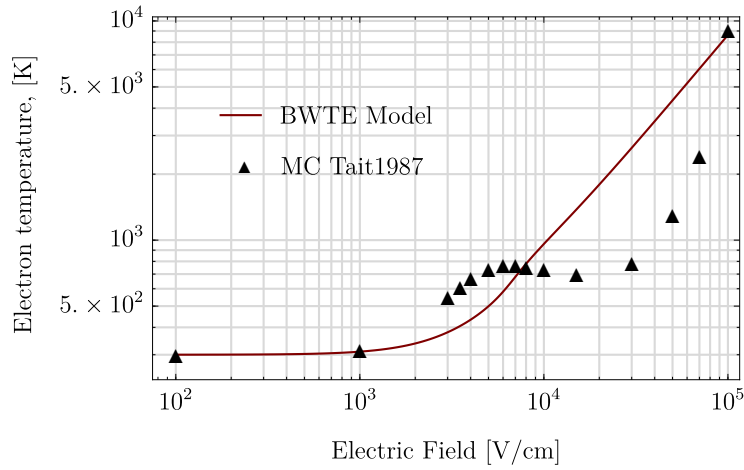


Figure 4.28: High-field behavior of electron temperature using the Baccarani & Wordeman transferred electron model, along with Monte Carlo results from Tait [52].

Therefore, both the energy relaxation time $\tau_{\epsilon,n}$ and the population ratio P_L need to be improved in order to achieve more accurate results for electron temperature, that in turn lead to better transport parameters using the BWTE model. In this sense, the most critical expression to improve seems to be P_L , specially considering the assumptions made in order to obtain the expression. Given that most transport parameters depend directly on electron

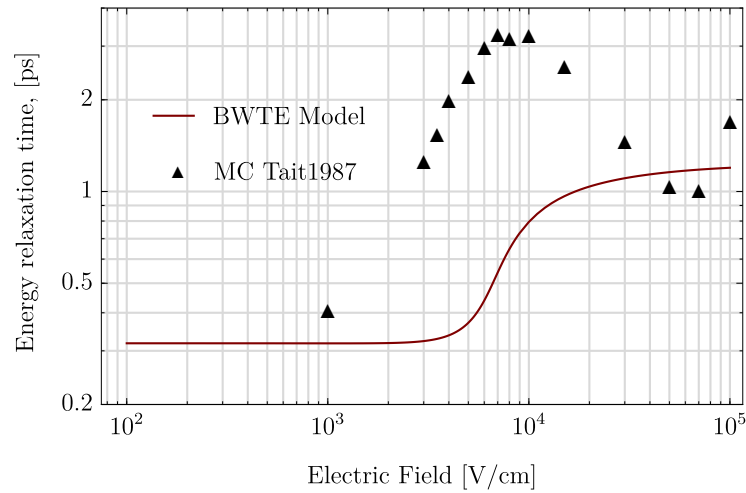


Figure 4.29: High-field behavior of energy relaxation time for electrons using the Bacarani & Wordeman transferred electron model, along with Monte Carlo results from Tait [52].

temperature, the fact that this variable is not accurately predicted is relevant and should be further studied.

Conclusions

The main conclusions of the studies performed in the present work are described in the following chapter.

Numerical Verification of the Results

On the first place, a simple case of a symmetric solar cell under a spatially constant carrier generation rate was solved, where no high-field effects were considered. Convective energy flux is not included in the energy balance, only heating by means of collision phenomena, and heat transfer is modelled using Fourier's law. Boundary conditions for carrier densities and electric potential are imposed according to Section 3.3, while thermal boundary conditions are assumed constant for both electrons and lattice. This was performed in order to describe the general behaviour of charge carriers within a solar cell under operation, as well as to validate the numerical method used for the subsequent results.

An analysis of the numerical method is presented in Section 4.1. The convergence of the scheme was analysed for the solution of a solar cell example case. For the solved case, the solution of the HD model was obtained taking the DRA as an initial condition for a mesh of $Nu=2000$ and a constant relaxation parameter. Several iterations of the method are presented in order to show the variation of each variable. The DRA was observed to be a good approximation for voltage and carrier densities, while special care needs to be taken for temperature in order to avoid divergence, specially carrier temperature which varies greatly in space. Given that high-field effects are not being taken into account, electron temperatures and velocities present higher values than what would be expected in reality. This observations corroborate the importance of the selection of the initial conditions. Much improvement can be achieved in convergence time by selecting an appropriate relaxation parameter θ . A mesh sensibility analysis was also performed through the study of the location and magnitude of the residuals with respect to a solution using a fine mesh. This showed the importance of an adequate spatial interval for variables that present high gradients in small regions.

Additionally, the use of non-homogeneous discretization of space is required in order to efficiently solve cases where doping differences are higher or the dimensions of the device are larger. It is also important to take special care with the convergence of velocities and current, since these are obtained from balances of high magnitude gradients. The obtained value is therefore very sensitive to the accuracy of the method.

Some numerical instabilities are presented at the minority carrier boundaries, when increasing the length of the device. These are caused by the treatment of the carrier density spatial gradient direction. This can be solved through the use of an adapted discretization method, such as the upwind scheme.

HD modeling of a single junction solar cell

Section 4.2 presents a general description of the physical behaviour observed in the involved variables. The non-dimensional version of the results is presented. The length of the depletion region, *i.e.* where major variations in the magnitude of each variables occur, is observed to be virtually the same as given by the DRA. Voltage through the device is the variable that presents less deviation from the result given by the DRA. This will be the case for solar cells as long as the length of each doped side is sufficiently larger than the corresponding depleted region and, therefore, the quasi-neutral zones develops.

The behaviour of charge carriers along the device is also well depicted, presenting constant values of carrier densities at the majority carrier regions corresponding with low values of carrier velocities. On the other hand, at the minority sides of the cell, generated carriers exhibit a decreasing density value as they approach the junction and recombine, at the same time as an increasing velocity magnitude in accordance to the high electric fields value near the junction. It is also observed that the behaviour of carriers near the minority side surface is well modelled, presenting an inversion in the velocity value. The expression for the minority carriers boundary condition has to be reconsidered when the thickness of the doped region is small, as in thin film solar cells. In that case, a constant surface recombination velocity value might not be the best approximation of the phenomenon.

Lattice temperature exhibits a practically constant value for this case. This is because thermalization because of sub-bandgap losses nor recombination heating are considered. Considering variations in transport properties because of high energy values could also contribute to the heating of the lattice. In contrast, electron temperature presents an important peak at the minority side of the junction, matching electron velocity peak. Since high magnitude variations are not located near the surface of the cell, electron temperature gradient does not generate a direct effect on the attainable current. However, the high values of electron temperature near the junction cause variations on the transport properties, which directly affect the amount of carriers that are captured into the majority region. Because of this it is of great importance to consider high-field models into the transport equations.

When studying devices that do not present a clear quasi-neutral region, such as thin-film solar cells, the effect of carrier temperature near the surface should be considerable. In those cases, surface boundary conditions should be reconsidered in order to accurately represent the physics involved. On one hand, the value of surface recombination velocity can no longer be considered as a constant value. Additionally, the assumption of thermal equilibrium between lattice and carrier temperatures is questionable.

Hot-Carriers at the Contacts of a Solar Cell

The performance of a GaAs PN junction solar cell under different thermal boundary conditions was studied. In this case, holes are assumed to be at thermal equilibrium with electrons. On the first place, three different output voltage values were considered for the same thermal boundary conditions. An increase in the velocity of carriers is observed as voltage is decreased, which is attributed to the higher electric field near the junction. Carrier temperature peak is also observed to decrease as voltage is increased, which correlates to the cell working closer to the MPP. Heating of the lattice through the Joule effect is considerable, even though the concentration of current at the contacts is not considered due to the 1D characteristics of the simulation. The relatively high heating level of the lattice is explained because of the constant value assumed for electron thermal conductivity. Therefore, a comprehensive analysis which involve carrier-lattice thermal interaction should consider a model for electron thermal conductivity, such as the Wiedemann-Franz model.

Different thermal boundary conditions were imposed on the model of the solar cell. When varying lattice temperature, electron temperature was selected in order to achieve a reference value for the temperature coefficient, dV_{oc}/dT_L . As observed in experience, when the solar cell is working under higher lattice temperatures, lower performance values are achieved. Therefore, output current is reduced. Additionally, electron temperature boundary condition was varied while lattice temperature remained constant. It was observed that imposing higher electron temperature on the boundaries of the device, increases the total output current and, therefore, the efficiency of the cell. A positive value of $dV_{oc}/dT_n = 3.2 \text{ mV/K}$ was obtained for the open circuit linear thermal dependence factor for electron temperature at the boundaries. This is a direct consequence of hot carrier extraction, given that the excess of energy is not transformed into lattice heating.

This results indicate that important improvements can be achieved in the performance of the solar cell by means of improving the thermal management at the contacts. While electron temperature at the contacts needs to be maintained at high levels, lattice temperature is desired to be as low as possible. The two-temperature thermal modeling contributes to predict the thermal resistance of solar cells, to improve the thermal control strategies and the design of cooling systems to be used in photovoltaic modules.

Hole Temperature Assumption Verification

One of the main assumptions regarding charge carriers temperature was also analysed by the comparison of two conditions, holes temperature equal to electron temperature, $T_p = T_n$, and holes temperature equal to lattice temperature, $T_p = T_L$. High field effects on transport parameters were not considered on these calculations. It was observed that the contribution of holes into the carrier energy balance is rather small, which implies that considering holes temperature equal to electron temperature is virtually equivalent to imposing the temperature profile of electrons to holes. These have a temperature peak at the p -side of the junction, which by the solution of mass and momentum balances implies an increase in holes density,

along with a decrease in their velocity. The high density and low velocity values of holes near the junction causes that the expected depression in density value of solar cells under operation is not observed. In turn, this increase in hole density builds-up electric charge in this region, causing an inversion of the electric field, which is also not expected under normal operating conditions. Even though lattice temperature is low in both cases a difference in several orders of magnitude can be seen in the transmission of energy to the lattice, which is higher in the case of $T_p = T_n$ because of the high thermalization rate caused by the high energy of holes at a high density area. An important difference between both cases can also be seen in the total current value, because of the effect of temperature on the recombination levels. Therefore, it is really important to use the most adequate assumption because it has great effect when obtaining quantitative results. As a conclusion, the assumption of $T_p = T_L$ is a better and more physically justified assumption than $T_p = T_n$.

High Field Mobility Effects

In order to provide the most accurate description of charge carriers behaviour for future works, section 4.5 studies the implications of using different mobility models in charge transport parameters. Temperature dependent and field dependent models are compared assuming a bulk of semiconductor under a constant electric field, in this way, a relation between electric field and temperature is obtained.

On the first place, temperature dependent models for single valley semiconductors are analysed. In particular, the model proposed by Baccarani & Wordeman is compared to the one by Hänsch. It was observed that both models accurately described the decrease of electron mobility as electric field is increased. Additionally, different values of energy relaxation times were evaluated for the Hänsch model. With all of them, a good representation of electron velocity according to electric field is obtained. However, a great difference is observed in the respective level of carrier temperature. An important difference is also observed between both models when comparing different doping levels. As a result, even though both models provide an accurate description of carriers behaviour, due to the additional difficulty of selecting a correct value of energy relaxation time for the Hänsch model, and the effect this can have on the values of the transport parameters, the BW model was used for the subsequent analysis.

On the second place, the use of an electron temperature dependent transferred electron model is studied, which applies the Baccarani & Wordeman model in order to represent the transport parameters on each independent band. A brief review of references for the transport parameters on each band is presented.

Within this model, given that the population ratio, P_L , is used in order to define the importance of each band on the average transport properties, two different averaging functions are studied for energy relaxation time. The first one assumes the energy relaxation time as an intrinsic property of electrons on the central and satellite bands, while the second arises from assuming thermal equilibrium of electrons on each band. It was observed that the first assumption delivers results which fit very good with the TE field dependent model, while

the second one presents a decrease of carrier velocity at much higher electric fields. A slight difference in the electric field corresponding to the peak velocity value was also observed. Better results were not obtained assuming different values of $\mu_{n,0}^L$ and $v_{n,sat}^\Gamma$. In order to improve this, a different distribution function for the population ratio would be needed.

Finally, the results are compared with a reference which provided phenomenological transport parameters from large scale Monte Carlo simulations. A very good agreement is observed for carrier velocity between the results obtained from the BWTE and Monte Carlo models, with slight differences at middle field values caused mainly by the distribution function used for the population ratio. When momentum relaxation time and effective mass are analysed, a relatively good agreement can be seen for both. However, a noticeable difference is observed for the average mass value between the BWTE model and Monte Carlo results, in particular at the onset of electron transfer from one band to the other, which is directly attributed to the population ratio, P_L . When analysing electron temperature, which is the independent variable in the relations, a great difference is observed between both results. It is deduced that this is caused by the effect of the averaging expression for the energy relaxation time, along with the distribution function for the population ratio, which increases this difference.

In conclusion, the BWTE model delivers results with a good fit to results from Monte Carlo simulations for momentum relaxation time, average effective mass and, in turn, carrier velocity, but show a greater difference for carrier temperature and energy relaxation time. In order to obtain more accurate results, the averaging expression for the energy relaxation time $\tau_{\epsilon,n}$ and the distribution function for the population ratio P_L need to be improved.

Future Work

As a continuation or related work to what is presented in this thesis, the following topics are suggested:

- Study of thermal contribution of different heat losses on a solar cell, comparing their quantification through analytical expressions with a hydrodynamic model considering high field effects.
- Using the hydrodynamic model for the improvement of the understanding of thermal behavior in novel technologies such as thin film or perovskite solar cells.
- In depth study of boundary thermo-electrical effects as the distance between the junction and the cell surface gets shorter, such as in thin film solar cells.
- Two, or three, dimensional study of hot spot generation and dissipation using a hydrodynamic model.
- Implement a model using L -band electrons as a third carrier in order to develop an improved expression for band population distribution function.

Bibliography

- [1] Tom Randall. Fossil fuels just lost the race against renewables. *Bloomberg*, April 14th 2015.
- [2] Renewable Energy Policy Network for the 21st Century REN21. Renewables 2016: Global Status Report, 2016.
- [3] Ministerio de Energía, Gobierno de Chile. Una mirada participativa del rol y los impactos de las energías renovables en la matriz eléctrica futura, March 8th, 2016.
- [4] William Shockley and Hans J Queisser. Detailed balance limit of efficiency of p-n junction solar cells. *Journal of applied physics*, 32(3):510–519, 1961.
- [5] Martin A Green. Third generation photovoltaics: Ultra-high conversion efficiency at low cost. *Progress in Photovoltaics: Research and Applications*, 9(2):123–135, 2001.
- [6] Matthew C Beard, Joseph M Luther, and Arthur J Nozik. The promise and challenge of nanostructured solar cells. *Nature nanotechnology*, 9(12):951–954, 2014.
- [7] Alexis De Vos. Detailed balance limit of the efficiency of tandem solar cells. *Journal of Physics D: Applied Physics*, 13(5):839, 1980.
- [8] Antonio Luque and Antonio Martí. Theoretical limits of photovoltaic conversion. *Handbook of Photovoltaic Science and Technology*, Wiley, Chichester, UK, 2003.
- [9] LC Hirst, RJ Walters, MF Führer, and NJ Ekins-Daukes. Experimental demonstration of hot-carrier photo-current in an InGaAs quantum well solar cell. *Applied Physics Letters*, 104(23):231115, 2014.
- [10] Ronald C Knechtli, Robert Y Loo, and G Sanjiv Kamath. High-efficiency GaAs solar cells. *Electron Devices, IEEE Transactions on*, 31(5):577–588, 1984.
- [11] G Baccarani and MR Wordeman. An investigation of steady-state velocity overshoot in silicon. *Solid-State Electronics*, 28(4):407–416, 1985.
- [12] Carl L Gardner. Numerical simulation of a steady-state electron shock wave in a submicrometer semiconductor device. *IEEE Transactions on Electron Devices*, 38(2):392–398, 1991.
- [13] Wolfgang Quade, Massimo Rudan, and Eckehard Schöll. Hydrodynamic simulation of

- impact-ionization effects in pn junctions. *Computer-Aided Design of Integrated Circuits and Systems, IEEE Transactions on*, 10(10):1287–1294, 1991.
- [14] Kamran Mohseni, Ali Shakouri, Rajeev J Ram, and Mathew C Abraham. Electron vortices in semiconductor devices. *Physics of Fluids (1994-present)*, 17(10):100602, 2005.
- [15] D Chen, Z Yu, K-C-C Wu, R Goossens, and RW Dutton. Dual energy transport model with coupled lattice and carrier temperatures. In *Simulation of Semiconductor Devices and Processes*, pages 157–160. Springer, 1993.
- [16] A Majumdar, K Fushinobu, and K Hijikata. Heat generation and transport in submicron semiconductor devices. *Journal of Heat transfer*, 117:25–31, 1995.
- [17] Markus Brunk and Ansgar Jüngel. Heating of semiconductor devices in electric circuits. In *Scientific Computing in Electrical Engineering SCEE 2008*, pages 261–272. Springer, 2010.
- [18] Juan Osses-Márquez and Williams R Calderón-Muñoz. Thermal influence on charge carrier transport in solar cells based on GaAs PN junctions. *Journal of Applied Physics*, 116(15):154502, 2014.
- [19] William D Callister, David G Rethwisch, et al. *Materials science and engineering: An introduction*, volume 7. Wiley New York, 2007.
- [20] Michael Shur. *Physics of semiconductor devices*. Prentice-Hall, Inc., 1990.
- [21] JS Blakemore. Semiconducting and other major properties of gallium arsenide. *Journal of Applied Physics*, 53(10):R123–R181, 1982.
- [22] Umesh Mishra and Jasprit Singh. *Semiconductor device physics and design*. Springer Science & Business Media, 2007.
- [23] Simon M Sze and Kwok K Ng. *Physics of semiconductor devices*. John Wiley & Sons, 2006.
- [24] James R Chelikowsky and Marvin L Cohen. Nonlocal pseudopotential calculations for the electronic structure of eleven diamond and zinc-blende semiconductors. *Physical Review B*, 14(2):556, 1976.
- [25] YP Varshni. Temperature dependence of the energy gap in semiconductors. *Physica*, 34(1):149–154, 1967.
- [26] ME Levinshtein, SL Rumyantsev, and MS Shur. Handbook series of semiconductor parameters, vol 1: Elementary semiconductors and A3B5 compounds Si, Ge C, GaAs, GaP, GaSb InAs, InP, InSb. *World Sci Publ Co*, 1996.
- [27] Martin A Green. Intrinsic concentration, effective densities of states, and effective mass in silicon. *Journal of Applied Physics*, 67(6):2944–2954, 1990.

- [28] Biswaranjan R Nag. *Electron transport in compound semiconductors*, volume 11. Springer Science & Business Media, 2012.
- [29] Vassil Palankovski. *Simulation of heterojunction bipolar transistors*. PhD thesis, Technischen Universitat Wien, 2000.
- [30] Robert F Pierret and Gerold W Neudeck. *Advanced semiconductor fundamentals*, volume 6. Addison-Wesley Reading, MA, 1987.
- [31] Jenny Nelson. *The physics of solar cells*, volume 1. World Scientific, 2003.
- [32] Ansgar Jünger. *Transport equations for semiconductors*, volume 773. Springer, 2009.
- [33] Mark Lundstrom. *Fundamentals of carrier transport*. Cambridge University Press, 2009.
- [34] Kjell Blotekjaer. Transport equations for electrons in two-valley semiconductors. *Electron Devices, IEEE Transactions on*, 17(1):38–47, 1970.
- [35] Tibor Grasser, Ting-Wei Tang, Hans Kosina, and Siegfried Selberherr. A review of hydrodynamic and energy-transport models for semiconductor device simulation. *Proceedings of the IEEE*, 91(2):251–274, 2003.
- [36] Shin-Chi Lee and Ting-Wei Tang. Transport coefficients for a silicon hydrodynamic model extracted from inhomogeneous monte-carlo calculations. *Solid-State Electronics*, 35(4):561–569, 1992.
- [37] Angelo Marcello Anile and Vittorio Romano. Hydrodynamical modeling of charge carrier transport in semiconductors. *Meccanica*, 35(3):249–296, 2000.
- [38] W van Roosbroeck. Theory of the flow of electrons and holes in germanium and other semiconductors. *Bell System Technical Journal*, 29(4):560–607, 1950.
- [39] N.D Arora, J.R Hauser, and D.J Roulston. Electron and hole mobilities in silicon as a function of concentration and temperature. *IEEE Transactions on Electronic Devices*, 29(2):292–295, 1982.
- [40] M Sotoodeh, AH Khalid, and AA Rezazadeh. Empirical low-field mobility model for III–V compounds applicable in device simulation codes. *Journal of applied physics*, 87(6):2890–2900, 2000.
- [41] Guido Masetti, Maurizio Severi, and Sandro Solmi. Modeling of carrier mobility against carrier concentration in arsenic-, phosphorus-, and boron-doped silicon. *Electron Devices, IEEE Transactions on*, 30(7):764–769, 1983.
- [42] D.M Caughey and R.E Thomas. Carrier mobilities in silicon empirically related to doping and field. *Proceedings of the IEEE*, 55(12):2192–2193, 1967.
- [43] R Quay, C Moglestue, Vassil Palankovski, and Siegfried Selberherr. A temperature dependent model for the saturation velocity in semiconductor materials. *Materials Science*

- in Semiconductor Processing*, 3(1):149–155, 2000.
- [44] C Canali, G Majni, R Minder, and G Ottaviani. Electron and hole drift velocity measurements in silicon and their empirical relation to electric field and temperature. *Electron Devices, IEEE Transactions on*, 22(11):1045–1047, 1975.
- [45] Ansgar Jüngel and Shaoqiang Tang. A relaxation scheme for the hydrodynamic equations for semiconductors. *Applied numerical mathematics*, 43(3):229–252, 2002.
- [46] W Hänsch, M Orlowski, and W Weber. The hot-electron problem in submicron mosfet. *Le Journal de Physique Colloques*, 49(C4):C4–597, 1988.
- [47] Benito Gonzalez, Vassil Palankovski, Hans Kosina, A Hernandez, and Siegfried Selberherr. An energy relaxation time model for device simulation. *Solid-State Electronics*, 43(9):1791–1795, 1999.
- [48] Siegfried Selberherr. *Analysis and simulation of semiconductor devices*. Springer Science & Business Media, 2012.
- [49] John J Barnes, Ronald J Lomax, and George I Haddad. Finite-element simulation of gaas mesfet’s with lateral doping profiles and submicron gates. *IEEE transactions on electron devices*, 23(9):1042–1048, 1976.
- [50] Hans Hjelmgren. Numerical modeling of hot electrons in n-gaas schottky-barrier diodes. *IEEE Transactions on Electron Devices*, 37(5):1228–1234, 1990.
- [51] Xing Zhou and Hong Siang Tan. Monte carlo formulation of field-dependent mobility for alxga1-xas. *Solid-state electronics*, 38(6):1264–1266, 1995.
- [52] Gregory B Tait and Clifford M Krowne. Efficient transferred electron device simulation method for microwave and millimeter wave CAD applications. *Solid-state electronics*, 30(10):1025–1036, 1987.
- [53] Max Planck. On the law of distribution of energy in the normal spectrum. *Annalen der Physik*, 4(553):1, 1901.
- [54] ASTM Standard. G159, standard tables for references solar spectral irradiance at Air Mass 1.5: Direct normal and hemispherical for a 37 tilted surface (withdrawn 2015). *Society for Testing Matls., West Conshocken, PA, USA*, 1998.
- [55] Tables and graphs of the complex index of refraction for common microfabrication materials. <http://www.photonics.byu.edu/tabulatedopticalconstants.phtml>. Accessed: 2015-10-14.
- [56] MD Sturge. Optical absorption of gallium arsenide between 0.6 and 2.75 eV. *Physical Review*, 127(3):768, 1962.
- [57] HC Casey Jr, DD Sell, and KW Wecht. Concentration dependence of the absorption coefficient for n- and p- type GaAs between 1.3 and 1.6 eV. *Journal of Applied Physics*,

- 46(1):250–257, 1975.
- [58] WG Spitzer and JM Whelan. Infrared absorption and electron effective mass in n-type gallium arsenide. *Physical Review*, 114(1):59, 1959.
- [59] Edward D Palik. *Handbook of optical constants of solids*, volume 3. Academic press, 1998.
- [60] R Quay, H Massler, W Kellner, T Grasser, V Palankovski, and S Selberherr. Simulation of gallium-arsenide based high electron mobility transistors. In *Simulation of Semiconductor Processes and Devices, 2000. SISPAD 2000. 2000 International Conference on*, pages 74–77. IEEE, 2000.
- [61] Andres Cuevas. The recombination parameter J_0 . *Energy Procedia*, 55:53–62, 2014.
- [62] Markus C Scharber, David Mühlbacher, Markus Koppe, Patrick Denk, Christoph Wadtauf, Alan J Heeger, and Christoph J Brabec. Design rules for donors in bulk-heterojunction solar cells - towards 10% energy-conversion efficiency. *Advanced Materials*, 18(6):789–794, 2006.
- [63] Sung Heum Park, Anshuman Roy, Serge Beaupre, Shinuk Cho, Nelson Coates, Ji Sun Moon, Daniel Moses, Mario Leclerc, Kwanghee Lee, and Alan J Heeger. Bulk heterojunction solar cells with internal quantum efficiency approaching 100%. *Nature Photonics*, 3(5):297–302, 2009.
- [64] Jong Pil Kim, Ho Lim, Ju Hun Song, Young June Chang, and Chung Hwan Jeon. Numerical analysis on the thermal characteristics of photovoltaic module with ambient temperature variation. *Solar Energy Materials and Solar Cells*, 95(1):404–407, 2011.
- [65] Angelo Marcello Anile and Vittorio Romano. Hydrodynamical modeling of charge carrier transport in semiconductors. *Meccanica*, 35(3):249–296, 2000.
- [66] Chan L Tien, Aruvana Majumdar, and Frank M Gerner. *Microscale Energy Transport*. Taylor & Francis, 1998.
- [67] Stephen Lewis Teitel and JW Wilkins. Ballistic transport and velocity overshoot in semiconductors: Part i- uniform field effects. *IEEE Transactions on Electron Devices*, 30(2):150–153, 1983.
- [68] Grégoire Allaire. *Numerical analysis and optimization:: an introduction to mathematical modelling and numerical simulation*. 2007.
- [69] Romain Couderc, Mohamed Amara, and Mustapha Lemiti. In-depth analysis of heat generation in silicon solar cells. *IEEE Journal of Photovoltaics*, 6(5):1123–1131, 2016.
- [70] Jihong Zhang, Yulin Gao, Yijun Lu, Lihong Zhu, Ziquan Guo, Guolong Chen, and Zhong Chen. Transient thermal resistance test of single-crystal-silicon solar cell. *IEEE Transactions on Electron Devices*, 59(9):2345–2349, 2012.

- [71] BJ Huang, PE Yang, YP Lin, BY Lin, HJ Chen, RC Lai, and JS Cheng. Solar cell junction temperature measurement of pv module. *Solar Energy*, 85(2):388–392, 2011.
- [72] Anthony C Vasko, Aaroehi Vijn, and Victor G Karpov. Hot spots spontaneously emerging in thin film photovoltaics. *Solar Energy*, 108:264–273, 2014.
- [73] VG Karpov, A Vasko, and A Vijn. Hot spot runaway in thin film photovoltaics and related structures. *Applied Physics Letters*, 103(7):074105, 2013.
- [74] Mauricio D Perez and Nima E Gorji. Modeling of temperature profile, thermal runaway and hot spot in thin film solar cells. *Materials Science in Semiconductor Processing*, 41:529–534, 2016.
- [75] Williams R Calderón-Muñoz and Cristian Jara-Bravo. Hydrodynamic modeling of hot-carrier effects in a pn junction solar cell. *Acta Mechanica*, pages 1–14, 2016.
- [76] Stephen M Goodnick and Christiana Honsberg. Ultrafast carrier relaxation and nonequilibrium phonons in hot carrier solar cells. In *Photovoltaic Specialists Conference (PVSC), 2011 37th IEEE*, pages 002066–002070. IEEE, 2011.
- [77] GMMW Bissels, MAH Asselbergs, GJ Bauhuis, P Mulder, EJ Haverkamp, E Vlieg, and JJ Schermer. Anomalous iv-characteristics of a gaas solar cell under high irradiance. *Solar Energy Materials and Solar Cells*, 104:97–101, 2012.
- [78] Kensuke Nishioka, Tatsuya Takamoto, Takaaki Agui, Minoru Kaneiwa, Yukiharu Uraoka, and Takashi Fuyuki. Evaluation of temperature characteristics of high-efficiency ingap/ingaas/ge triple-junction solar cells under concentration. *Solar energy materials and solar cells*, 85(3):429–436, 2005.
- [79] MY Feteha and GM Eldallal. The effects of temperature and light concentration on the gainp/gaas multijunction solar cell’s performance. *Renewable Energy*, 28(7):1097–1104, 2003.
- [80] Matthew C Beard and Randy J Ellingson. Multiple exciton generation in semiconductor nanocrystals: Toward efficient solar energy conversion. *Laser & Photonics Reviews*, 2(5):377–399, 2008.
- [81] Kensuke Nishioka, Tatsuya Takamoto, Takaaki Agui, Minoru Kaneiwa, Yukiharu Uraoka, and Takashi Fuyuki. Annual output estimation of concentrator photovoltaic systems using high-efficiency ingap/ingaas/ge triple-junction solar cells based on experimental solar cell’s characteristics and field-test meteorological data. *Solar Energy Materials and Solar Cells*, 90(1):57–67, 2006.
- [82] Edgar Buckingham. On physically similar systems; illustrations of the use of dimensional equations. *Physical review*, 4(4):345, 1914.
- [83] PA Houston and AGR Evans. Electron drift velocity in n-gaas at high electric fields. *Solid-State Electronics*, 20(3):197–204, 1977.

- [84] KH Nichols, Camellia ML Yee, and CM Wolfe. High-temperature carrier transport in n-type epitaxial gaas. *Solid-State Electronics*, 23(2):109–116, 1980.
- [85] B Kramer and A Mircea. Determination of saturated electron velocity in gaas. *Applied Physics Letters*, 26(11):623–625, 1975.
- [86] PM Smith, M Inoue, and Jeffrey Frey. Electron velocity in si and gaas at very high electric fields. *Applied Physics Letters*, 37(9):797–798, 1980.

Appendices

Appendix A

HD model derivation

Hydrodynamic set of equations from original HD model, with non specified collision terms. The equations below will be expressed for any carrier, electron or hole, designated as ρ , every variable contained in this section is dependent of the specific carrier.

A.1 Zeroth moment

Multiplying Boltzmann's transport equation by the zeroth moment delivers the continuity equation for semiconductors.

$$\partial_t \rho + \nabla \cdot (\rho \mathbf{u}) = (\partial_t \rho)_c \quad (\text{A.1})$$

Where $(\partial_t \rho)_c$ accounts for collision (source and sink) terms, in this case generation and recombination of electrons. Then for electrons and holes respectively:

$$\partial_t n^* + \nabla \cdot (n^* \mathbf{u}_n^*) = (\partial_t n^*)_c \quad (\text{A.2})$$

$$\partial_t p^* + \nabla \cdot (p^* \mathbf{u}_p^*) = (\partial_t p^*)_c \quad (\text{A.3})$$

A.2 First moment

Multiplying Boltzmann's transport equation by the first moment $\hbar \mathbf{k}/m^* = \mathbf{p}/m^*$ delivers the momentum balance equation for semiconductors.

$$\partial_t (\mathbf{p}) + \nabla \cdot (\mathbf{p} \otimes \mathbf{u}) = e\rho \nabla V - \nabla (\rho k_B T) + (\partial_t (\mathbf{p}))_c \quad (\text{A.4})$$

Then, using a parabolic band model, meaning constant effective mass m^* , the carrier momentum can be written as:

$$\mathbf{p} = m^* \rho \mathbf{u} \quad (\text{A.5})$$

And momentum equation A.4 is expressed as:

$$\partial_t (m^* \rho \mathbf{u}) + \nabla \cdot (m^* \rho \mathbf{u} \otimes \mathbf{u}) = e \rho \nabla V - \nabla (\rho k_B T) + (\partial_t (m \rho \mathbf{u}))_c \quad (\text{A.6})$$

The second term can be expanded given that mass is considered constant and using the expression for the divergence of a tensorial product as:

$$\nabla \cdot (m^* \rho \mathbf{u} \otimes \mathbf{u}) = m^* (\mathbf{u} \nabla \cdot (\rho \mathbf{u}) + \rho \mathbf{u} \nabla \cdot \mathbf{u}) \quad (\text{A.7})$$

Then equation A.6 turns to:

$$\begin{aligned} m^* (\rho \partial_t \mathbf{u} + \mathbf{u} \partial_t \rho + \mathbf{u} \nabla \cdot (\rho \mathbf{u}) + \rho \mathbf{u} \nabla \cdot \mathbf{u}) &= e \rho \nabla V - \nabla (\rho k_B T) + m^* (\rho (\partial_t \mathbf{u})_c + \mathbf{u} (\partial_t \rho)_c) \\ m^* \rho \partial_t \mathbf{u} + m^* \mathbf{u} [\partial_t \rho + \nabla \cdot (\rho \mathbf{u}) - (\partial_t \rho)_c] + m^* \rho \mathbf{u} \nabla \cdot \mathbf{u} &= e \rho \nabla V - \nabla (\rho k_B T) + m^* \rho (\partial_t \mathbf{u})_c \end{aligned} \quad (\text{A.8})$$

Where the expression in square brackets equals zero from A.1 and hence the expression in terms of carrier velocity is obtained.

$$m^* \rho \partial_t \mathbf{u} + m^* \rho \mathbf{u} \nabla \cdot \mathbf{u} = e \rho \nabla V - \nabla (\rho k_B T) + m^* \rho (\partial_t \mathbf{u})_c \quad (\text{A.9})$$

And dividing by $m^* \rho$:

$$\partial_t \mathbf{u} + \mathbf{u} \nabla \cdot \mathbf{u} = \frac{e}{m^*} \nabla V - \frac{k_B}{m^* \rho} \nabla (\rho T) + (\partial_t \mathbf{u})_c \quad (\text{A.10})$$

So expressing for electrons and holes using dimensional variables:

$$\partial_t \mathbf{u}_n^* + \mathbf{u}_n^* \nabla \cdot \mathbf{u}_n^* = \frac{e}{m_e^*} \nabla V - \frac{k_B}{m_e^* n^*} \nabla (n^* T_n^*) + (\partial_t \mathbf{u}_n^*)_c \quad (\text{A.11})$$

$$\partial_t \mathbf{u}_p^* + \mathbf{u}_p^* \nabla \cdot \mathbf{u}_p^* = -\frac{e}{m_h^*} \nabla V - \frac{k_B}{m_h^* p^*} \nabla (p^* T_p^*) + (\partial_t \mathbf{u}_p^*)_c \quad (\text{A.12})$$

where the first term on the right side has a negative sign because of the opposite electrical charge of holes.

A.3 Second moment

The equation obtained from integrating BTE using the second moment $\hbar^2|\mathbf{k}|^2/2m^*$ is the energy balance depending on the kinetic energy density:

$$\partial_t \xi + \nabla \cdot (\xi \mathbf{u} + \mathbf{q}) - e \rho \mathbf{u} \cdot \nabla V + \nabla \cdot (\rho k_B T \mathbf{u}) = (\partial_t \xi)_c \quad (\text{A.13})$$

Where the energy density is

$$\xi = \frac{3}{2} \rho k_B T + \frac{1}{2} \rho m^* u^2 \quad (\text{A.14})$$

And the heat flow is approximated by Fourier's law.

$$\mathbf{q} = -k_\rho \nabla T \quad (\text{A.15})$$

Using expression A.14 the transient term becomes:

$$\begin{aligned} \partial_t \xi &= \partial_t \left(\frac{3}{2} \rho k_B T + \frac{1}{2} \rho m^* u^2 \right) \\ &= \frac{3}{2} \rho k_B \partial_t T + \left(\frac{3}{2} k_B T + \frac{1}{2} m^* u^2 \right) \partial_t \rho + m^* \rho \mathbf{u} \cdot \partial_t \mathbf{u} \end{aligned}$$

Similarly for the collision terms:

$$(\partial_t \xi)_c = \frac{3}{2} \rho k_B (\partial_t T)_c + \left(\frac{3}{2} k_B T + \frac{1}{2} m^* u^2 \right) (\partial_t \rho)_c + m^* \rho \mathbf{u} \cdot (\partial_t \mathbf{u})_c$$

The second term in A.13, using Fourier's law is expanded as:

$$\begin{aligned} \nabla \cdot (\xi \mathbf{u} + \mathbf{q}) &= \nabla \cdot \left(\left(\frac{3}{2} k_B T + \frac{1}{2} m^* u^2 \right) (\rho \mathbf{u}) - k_\rho \nabla T \right) \\ &= \left(\frac{3}{2} k_B T + \frac{1}{2} m^* u^2 \right) \nabla \cdot (\rho \mathbf{u}) + \rho \mathbf{u} \cdot \nabla \left(\frac{3}{2} k_B T + \frac{1}{2} m^* u^2 \right) - \nabla \cdot (k_\rho \nabla T) \\ &= \left(\frac{3}{2} k_B T + \frac{1}{2} m^* u^2 \right) \nabla \cdot (\rho \mathbf{u}) + \rho \mathbf{u} \cdot \left(\frac{3}{2} k_B \nabla T + m^* \mathbf{u} \nabla \cdot \mathbf{u} \right) - \nabla \cdot (k_\rho \nabla T) \end{aligned}$$

Also the fourth term in A.13 is expanded as:

$$\nabla \cdot (\rho k_B T \mathbf{u}) = \rho k_B T \nabla \cdot \mathbf{u} + k_B \mathbf{u} \cdot \nabla (\rho T)$$

Replacing these expressions, equation A.13 is rewritten as:

$$\frac{3}{2} \rho k_B \partial_t T + \left(\frac{3}{2} k_B T + \frac{1}{2} m^* u^2 \right) \partial_t \rho + m^* \rho \mathbf{u} \cdot \partial_t \mathbf{u} + \left(\frac{3}{2} k_B T + \frac{1}{2} m^* u^2 \right) \nabla \cdot (\rho \mathbf{u})$$

$$\begin{aligned}
 & + \rho \mathbf{u} \cdot \left(\frac{3}{2} k_B \nabla T + m^* \mathbf{u} \nabla \cdot \mathbf{u} \right) - \nabla \cdot (k_\rho \nabla T) - e \rho \mathbf{u} \cdot \nabla V + \rho k_B T \nabla \cdot \mathbf{u} + k_B \mathbf{u} \cdot \nabla (\rho T) \\
 & = \frac{3}{2} \rho k_B (\partial_t T)_c + \left(\frac{3}{2} k_B T + \frac{1}{2} m^* u^2 \right) (\partial_t \rho)_c + m^* \rho \mathbf{u} \cdot (\partial_t \mathbf{u})_c \quad (\text{A.16})
 \end{aligned}$$

Reorganizing the terms we can write:

$$\begin{aligned}
 & \frac{3}{2} \rho k_B \partial_t T + \left(\frac{3}{2} k_B T + \frac{1}{2} m^* u^2 \right) [\partial_t \rho + \nabla \cdot (\rho \mathbf{u}) - (\partial_t \rho)_c] \\
 & + m \rho \mathbf{u} \cdot \left[\partial_t \mathbf{u} + \mathbf{u} \nabla \cdot \mathbf{u} - \frac{e}{m^*} \nabla V + \frac{k_B}{m^* \rho} \nabla (\rho T) - (\partial_t \mathbf{u})_c \right] \\
 & \frac{3}{2} k_B \rho \mathbf{u} \cdot \nabla T - \nabla \cdot (k_\rho \nabla T) + k_B \rho T \nabla \cdot \mathbf{u} = \frac{3}{2} k_B \rho (\partial_t T)_c \quad (\text{A.17})
 \end{aligned}$$

Where the expressions in square brackets on the first and second lines equal zero from equations A.1 and A.10 respectively, hence we get:

$$\frac{3}{2} \rho k_B \partial_t T + \frac{3}{2} k_B \rho \mathbf{u} \cdot \nabla T - \nabla \cdot (k_\rho \nabla T) + k_B \rho T \nabla \cdot \mathbf{u} = \frac{3}{2} k_B \rho (\partial_t T)_c \quad (\text{A.18})$$

Finally, dividing the whole expression by $3k_B\rho/2$ the energy balance as a function of carrier temperature is obtained:

$$\partial_t T + \mathbf{u} \cdot \nabla T + \frac{2}{3} T \nabla \cdot \mathbf{u} - \frac{2}{3k_B\rho} \nabla \cdot (k_\rho \nabla T) = (\partial_t T)_c \quad (\text{A.19})$$

Hence, for electrons and holes:

$$\partial_t T_n^* + \mathbf{u}_n^* \cdot \nabla T_n^* + \frac{2}{3} T_n^* \nabla \cdot \mathbf{u}_n^* - \frac{2}{3k_B n^*} \nabla \cdot (k_n \nabla T_n^*) = (\partial_t T_n^*)_c \quad (\text{A.20})$$

$$\partial_t T_p^* + \mathbf{u}_p^* \cdot \nabla T_p^* + \frac{2}{3} T_p^* \nabla \cdot \mathbf{u}_p^* - \frac{2}{3k_B p^*} \nabla \cdot (k_p \nabla T_p^*) = (\partial_t T_p^*)_c \quad (\text{A.21})$$

Appendix B

Components of the Jacobian Matrix

The following appendix presents the composition of the Jacobian matrix used to solve the finite difference scheme. As presented in Section 3.6, this is composed by

$$DF(w) = \begin{bmatrix} \frac{\partial F_V}{\partial V} & \frac{\partial F_V}{\partial n} & \frac{\partial F_V}{\partial p} & \frac{\partial F_V}{\partial T_c} & \frac{\partial F_V}{\partial T_L} \\ \frac{\partial F_n}{\partial V} & \frac{\partial F_n}{\partial n} & \frac{\partial F_n}{\partial p} & \frac{\partial F_n}{\partial T_c} & \frac{\partial F_n}{\partial T_L} \\ \frac{\partial F_p}{\partial V} & \frac{\partial F_p}{\partial n} & \frac{\partial F_p}{\partial p} & \frac{\partial F_p}{\partial T_c} & \frac{\partial F_p}{\partial T_L} \\ \frac{\partial F_c}{\partial V} & \frac{\partial F_c}{\partial n} & \frac{\partial F_c}{\partial p} & \frac{\partial F_c}{\partial T_c} & \frac{\partial F_c}{\partial T_L} \\ \frac{\partial F_L}{\partial V} & \frac{\partial F_L}{\partial n} & \frac{\partial F_L}{\partial p} & \frac{\partial F_L}{\partial T_c} & \frac{\partial F_L}{\partial T_L} \end{bmatrix}. \quad (3.36 \text{ rev.})$$

Using non dimensional version of $\kappa_n = nT_n$, the functions comprising $F(w)$ as presented at Section 3.6 as an example of a HD model, are

$$F_V = \frac{\partial^2 V}{\partial x^2} + \frac{1}{\lambda^2} (p - n + C) = 0, \quad (3.34a \text{ rev.})$$

$$F_n = -\frac{\partial(u_n n)}{\partial x} + (G - R) = 0, \quad (3.34b \text{ rev.})$$

$$F_p = -\frac{\partial(u_p p)}{\partial x} + (G - R) = 0, \quad (3.34c \text{ rev.})$$

$$F_c = \frac{\partial}{\partial x} \left(T_n n \frac{\partial T_n}{\partial x} \right) - \frac{\nu_n}{\varepsilon_n} n (T_n - T_L) - n \frac{\partial}{\partial x} (T_n u_n) + \frac{1}{3} n T_n \frac{\partial u_n}{\partial x} + \frac{2}{3} n u_n^2 = 0, \quad (3.34d \text{ rev.})$$

$$F_L = \psi \frac{\partial^2 T_L}{\partial x^2} + \frac{3}{2} \nu_n n (T_n - T_L) = 0. \quad (3.34e \text{ rev.})$$

These are used as an example in order to present the matrix as it is implemented in the code. First, the functions of F are written in their discrete version as

$$(F_V)_i = \frac{V_{i+1} - 2V_i + V_{i-1}}{\Delta x^2} + \frac{1}{\lambda^2} (p_i - n_i + C_i), \quad (\text{B.1})$$

$$(F_n)_i = -\frac{\bar{n}_R u_n^R - \bar{n}_L u_n^L}{\Delta x} + (G_i - R_i), \quad (\text{B.2})$$

$$(F_p)_i = -\frac{\bar{p}_R u_p^R - \bar{p}_L u_p^L}{\Delta x} + (G_i - R_i), \quad (\text{B.3})$$

$$(F_c)_i = \frac{\overline{(nT_n)}_R \cdot \partial_x^R T_n - \overline{(nT_n)}_L \cdot \partial_x^L T_n}{\Delta x} - \frac{5}{3} \frac{\overline{(nT_n)}_R \cdot u_n^R - \overline{(nT_n)}_L \cdot u_n^L}{\Delta x} \\ - n_i \frac{\overline{T_n}_R u_n^R - \overline{T_n}_L u_n^L}{\Delta x} + \frac{1}{3} n_i T_{ni} \frac{u_n^R - u_n^L}{\Delta x} - \frac{\nu_n}{\varepsilon_n} n_i (T_{ni} - T_{Li}) + \frac{2}{3} n_i u_n^R u_n^L \quad (\text{B.4})$$

$$(F_L)_i = \psi \frac{T_{Li+1} - 2T_{Li} + T_{Li-1}}{\Delta x^2} + \frac{3}{2} \nu_n n_i (T_{ni} - T_{Li}) \quad (\text{B.5})$$

Here, some terms are abbreviated in order to present the equations more clearly. For instance, the downstream average value of electron density is expressed as

$$\bar{n}_R = \frac{n_{i+1} + n_i}{2},$$

while the downstream expression for velocity is defined as

$$u_n^R = \partial_x^R V - \frac{1}{\bar{n}_R} \partial_x^R (nT_n) \\ = \left(\frac{V_{i+1} - V_i}{\Delta x} \right) - \left(\frac{2}{n_{i+1} + n_i} \right) \left(\frac{n_{i+1} T_{ni+1} - n_i T_{ni}}{\Delta x} \right).$$

Similar expressions are used for the rest of the variables, using the subscript L for the corresponding upstream expression. Once discretized, the partial derivative of each function in F is calculated. For instance, F_V derived in V , is expressed as

$$\frac{\partial F_V}{\partial V} \cdot \delta V = \frac{\delta V_{i+1} - 2\delta V_i + \delta V_{i-1}}{\Delta x^2}. \quad (\text{B.6})$$

Therefore, each matrix is expressed using the tridiagonal vectors as

$$\frac{\partial F_V}{\partial V} \cdot \delta V = a_i^{V,V} \delta V_{i-1} + b_i^{V,V} \delta V_i + c_i^{V,V} \delta V_{i+1} \quad (\text{B.7})$$

In this case in particular, each element is given by,

$$a_i^{V,V} = c_i^{V,V} = \frac{1}{\Delta x^2}, \quad (\text{B.8})$$

$$b_i^{V,V} = -\frac{2}{\Delta x^2}. \quad (\text{B.9})$$

The boundary conditions are established by $a_1^{VV}\delta V_0$ and $c_{N_u}^{VV}\delta V_{N_u+1}$. The same algorithm and analogue notation is used for every partial derivative. Each vector of the corresponding component of the matrix is presented ahead. For $\partial F_V/\partial n$ and $\partial F_V/\partial p$, the vectors are constant and given by

$$b_i^{V,p} = -b_i^{V,n} = \frac{1}{\lambda^2}. \quad (\text{B.10})$$

For electrons mass balance, the submatrices given by the partial derivatives $\partial F_n/\partial V$, $\partial F_n/\partial n$ and $\partial F_n/\partial T_c$ are given by,

$$a_i^{n,V} = -\frac{(\bar{n}_L)_i}{\Delta x^2} \quad (\text{B.11})$$

$$b_i^{n,V} = \frac{(\bar{n}_L)_i + (\bar{n}_R)_i}{\Delta x^2} \quad (\text{B.12})$$

$$c_i^{n,V} = -\frac{(\bar{n}_R)_i}{\Delta x^2} \quad (\text{B.13})$$

$$a_i^{n,n} = \frac{(T_n)_{i-1}}{\Delta x^2} + \frac{(\partial_x^L V)_i}{2\Delta x} \quad (\text{B.14})$$

$$b_i^{n,n} = -2\frac{(T_n)_i}{\Delta x^2} + \frac{(\partial_x^L V)_i - (\partial_x^R V)_i}{2\Delta x} \quad (\text{B.15})$$

$$c_i^{n,n} = \frac{(T_n)_{i+1}}{\Delta x^2} - \frac{(\partial_x^R V)_i}{2\Delta x} \quad (\text{B.16})$$

$$a_i^{n,c} = \frac{n_{i-1}}{\Delta x^2} \quad (\text{B.17})$$

$$b_i^{n,c} = -\frac{2n_i}{\Delta x^2} \quad (\text{B.18})$$

$$c_i^{n,c} = \frac{n_{i+1}}{\Delta x^2} \quad (\text{B.19})$$

For holes mass balance, the submatrices given by the partial derivatives $\partial F_p/\partial V$, $\partial F_p/\partial p$ and $\partial F_p/\partial T_L$ are given by,

$$a_i^{p,V} = \frac{(\bar{p}_L)_i}{\Delta x^2} \quad (\text{B.20})$$

$$b_i^{p,V} = -\frac{(\bar{p}_L)_i + (\bar{p}_R)_i}{\Delta x^2} \quad (\text{B.21})$$

$$c_i^{p,V} = \frac{(\bar{p}_R)_i}{\Delta x^2} \quad (\text{B.22})$$

$$a_i^{p,p} = \frac{(T_L)_{i-1}}{\Delta x^2} - \frac{(\partial_x^L V)_i}{2\Delta x} \quad (\text{B.23})$$

$$b_i^{p,p} = -2 \frac{(T_L)_i}{\Delta x^2} + \frac{(\partial_x^R V)_i - (\partial_x^L V)_i}{2\Delta x} \quad (\text{B.24})$$

$$c_i^{p,p} = \frac{(T_L)_{i+1}}{\Delta x^2} + \frac{(\partial_x^R V)_i}{2\Delta x} \quad (\text{B.25})$$

$$a_i^{n,L} = \frac{p_{i-1}}{\Delta x^2} \quad (\text{B.26})$$

$$b_i^{n,L} = -\frac{2p_i}{\Delta x^2} \quad (\text{B.27})$$

$$c_i^{n,L} = \frac{p_{i+1}}{\Delta x^2} \quad (\text{B.28})$$

For carriers energy balance, the submatrices given by the partial derivatives $\partial F_c / \partial V$, $\partial F_c / \partial n$, $\partial F_c / \partial T_c$ and $\partial F_c / \partial T_L$ are given by,

$$a_i^{c,V} = -\frac{2n_i}{3} \frac{(u_n^R)_i}{\Delta x} + \frac{n_i}{\Delta x^2} \left(\frac{(T_n)_i}{3} - (\overline{T_{nR}})_i \right) \quad (\text{B.29})$$

$$b_i^{c,V} = \frac{2n_i}{3} \frac{((u_n^R)_i - (u_n^L)_i)}{\Delta x} - \frac{n_i}{\Delta x^2} \left(\frac{2(T_n)_i}{3} - (\overline{T_{nR}})_i - (\overline{T_{nL}})_i \right) \quad (\text{B.30})$$

$$c_i^{c,V} = \frac{2n_i}{3} \frac{(u_n^L)_i}{\Delta x} + \frac{n_i}{\Delta x^2} \left(\frac{(T_n)_i}{3} - (\overline{T_{nL}})_i \right) \quad (\text{B.31})$$

$$\begin{aligned} a_i^{c,n} = & -\frac{(\partial_x^L T_n)_i (T_n)_{i-1}}{2\Delta x} + \left(\frac{2n_i}{3} \frac{(u_n^R)_i}{(\overline{n_L})_i} \right) \left(\frac{(\partial_x^L (nT_n))_i}{(\overline{n_L})_i} + \frac{(T_n)_{i-1}}{\Delta x} \right) \\ & - \left(\frac{(T_n)_i}{3\Delta x} - \frac{(\overline{T_{nL}})_i}{\Delta x} \right) \left(\frac{n_i}{(\overline{n_L})_i} \right) \left(\frac{(T_n)_{i-1}}{\Delta x} + \frac{(\partial_x^L (nT_n))_i}{2(\overline{n_L})_i} \right) \end{aligned} \quad (\text{B.32})$$

$$\begin{aligned} b_i^{c,n} = & \frac{((\partial_x^R T_n)_i - (\partial_x^L T_n)_i) (T_n)_i}{2\Delta x} + \frac{\nu_n}{\varepsilon_n} ((T_n)_i - (T_L)_i) + \frac{2}{3} (u_n^R)_i (u_n^L)_i \\ & + \frac{2n_i}{3} \left(\frac{(u_n^R)_i}{(\overline{n_L})_i} \left(\frac{(\partial_x^L (nT_n))_i}{2(\overline{n_L})_i} - \frac{(T_n)_i}{\Delta x} \right) + \frac{(u_n^L)_i}{(\overline{n_R})_i} \left(\frac{(\partial_x^R (nT_n))_i}{2(\overline{n_R})_i} + \frac{(T_n)_i}{\Delta x} \right) \right) \\ & + \left(\frac{(T_n)_i}{3\Delta x} - \frac{(\overline{T_{nR}})_i}{\Delta x} \right) \left(\frac{n_i}{(\overline{n_R})_i} \left(\frac{(T_n)_i}{\Delta x} + \frac{(\partial_x^R (nT_n))_i}{2(\overline{n_R})_i} \right) + (u_n^R)_i \right) \\ & + \left(\frac{(T_n)_i}{3\Delta x} - \frac{(\overline{T_{nL}})_i}{\Delta x} \right) \left(\frac{n_i}{(\overline{n_L})_i} \left(\frac{(T_n)_i}{\Delta x} - \frac{(\partial_x^L (nT_n))_i}{2(\overline{n_L})_i} \right) - (u_n^L)_i \right) \end{aligned} \quad (\text{B.33})$$

$$\begin{aligned}
 c_i^{c,n} = & \frac{(\partial_x^R T_n)_i (T_n)_{i+1}}{2\Delta x} + \left(\frac{2n_i (u_n^L)_i}{3(\bar{n}_R)_i} \right) \left(\frac{(\partial_x^R (nT_n))_i}{2(\bar{n}_R)_i} - \frac{(T_n)_{i+1}}{\Delta x} \right) \\
 & - \left(\frac{(T_n)_i}{3\Delta x} - \frac{(\bar{T}_{nR})_i}{\Delta x} \right) \left(\frac{n_i}{(\bar{n}_R)_i} \right) \left(\frac{(T_n)_{i+1}}{\Delta x} + \frac{(\partial_x^R (nT_n))_i}{2(\bar{n}_R)_i} \right)
 \end{aligned} \tag{B.34}$$

$$\begin{aligned}
 a_i^{c,c} = & \frac{1}{\Delta x} \left(\frac{(\bar{n}T_{nL})_i}{\Delta x} - \frac{n_{i-1} (\partial_x^L T_n)_i}{2} \right) + \frac{2n_i n_{i-1} (u_n^R)_i}{3(\bar{n}_L)_i \Delta x} \\
 & - \frac{n_i n_{i-1}}{(\bar{n}_L)_i \Delta x^2} \left(\frac{(T_n)_i}{3} - (\bar{T}_{nL})_i \right) + \frac{n_i (u_n^L)_i}{2\Delta x}
 \end{aligned} \tag{B.35}$$

$$\begin{aligned}
 b_i^{c,c} = & \frac{1}{\Delta x} \left(-\frac{(\bar{n}T_{nR})_i}{\Delta x} + \frac{n_i (\partial_x^R T_n)_i}{2} - \frac{(\bar{n}T_{nL})_i}{\Delta x} - \frac{n_{i-1} (\partial_x^L T_n)_i}{2} \right) - \frac{\nu_n n_i}{\varepsilon_n} \\
 & + \frac{n_i^2}{(\bar{n}_R)_i \Delta x^2} \left(\frac{(T_n)_i}{3} - (\bar{T}_{nR})_i \right) + \frac{n_i^2}{(\bar{n}_L)_i \Delta x^2} \left(\frac{(T_n)_i}{3} - (\bar{T}_{nL})_i \right) \\
 & + \frac{2n_i^2}{3\Delta x} \left(\frac{(u_n^L)_i}{(\bar{n}_R)_i} - \frac{(u_n^R)_i}{(\bar{n}_L)_i} \right) + \frac{n_i}{6\Delta x} \left((u_n^L)_i - (u_n^R)_i \right)
 \end{aligned} \tag{B.36}$$

$$\begin{aligned}
 c_i^{c,c} = & \frac{1}{\Delta x} \left(\frac{(\bar{n}T_{nR})_i}{\Delta x} + \frac{n_{i+1} (\partial_x^R T_n)_i}{2} \right) - \frac{2n_i n_{i+1} (u_n^L)_i}{3(\bar{n}_R)_i \Delta x} \\
 & - \frac{n_i n_{i+1}}{(\bar{n}_R)_i \Delta x^2} \left(\frac{(T_n)_i}{3} - (\bar{T}_{nR})_i \right) - \frac{n_i (u_n^R)_i}{2\Delta x}
 \end{aligned} \tag{B.37}$$

$$b_i^{c,L} = \frac{\nu_n}{\varepsilon_n} n_i \tag{B.38}$$

Finally, for lattice energy balance, the submatrices given by the partial derivatives $\partial F_L/\partial n$, $\partial F_L/\partial T_c$ and $\partial F_L/\partial T_L$ are given by,

$$b_i^{L,n} = \frac{3\nu_n}{2} ((T_n)_i - (T_L)_i) \tag{B.39}$$

$$b_i^{L,c} = \frac{3\nu_n}{2} n_i \tag{B.40}$$

$$a_i^{L,L} = \frac{\psi}{\Delta x^2} \tag{B.41}$$

$$b_i^{L,L} = -\frac{2\psi}{\Delta x^2} - \frac{3\nu_n}{2} n_i \tag{B.42}$$

$$c_i^{L,L} = \frac{\psi}{\Delta x^2} \tag{B.43}$$

The rest of the coefficients whose value is not specified are equal to zero.